UNIVERSITY OF SOUTHAMPTON

Faculty of Physical Sciences and Engineering

Optoelectronics Research Centre

Controlling Light with Plasmonic Metasurfaces

João P. Valente

Thesis for the degree of Doctor of Philosophy

June 3, 2016

Dedicated to my family, especially to Avô Henrique and Avô Fernando.

"Para viajar, basta existir"
Fernando Pessoa

"Lá vem a Nau Catrineta
Que tem muito que contar!
Ouvide agora, senhores,
Uma história de pasmar."
Almeida Garrett

UNIVERSITY OF SOUTHAMPTON

ABSTRACT

Faculty of Physical Sciences and Engineering

OPTOELECTRONICS RESEARCH CENTRE

Doctor of Philosophy

Controlling Light with Plasmonic Metasurfaces

by João P. Valente

Nanostructured membrane plasmonic metasurfaces have exciting mechanical properties and enable new approaches to dynamic control of optical radiation. In this thesis I report:

- The first realization of a photonic metasurface that can be reconfigured by application of electric current and magnetic field. In an artificial chevron nanowire structure, fabricated on an elastic nanomembrane, the Lorentz force drives reversible transmission changes on application of a fraction of a volt when the structure is placed in a fraction-of-Tesla magnetic field. The change of optical characteristics of the structure is underpinned by nanoscale movements of the nanowires and associated changes of their plasmonic spectra. I show that magneto-electro-optical modulation can be driven to hundreds of thousands of cycles per second promising applications in magneto-electro-optical modulators and field sensors at nano-Tesla levels. Stimulation-induced transmission changes reaching 45% have been observed in this structure at the telecommunications wavelength of 1550 nm.

- The photonic metasurface activated by the Lorentz force as a material structure exhibiting a giant reciprocal magneto-electro-optical effect that manifests itself as strong changes of optical properties of the metamaterial in response to simultaneous application of external electric and magnetic fields and does not depend on reversal of the propagation direction of the wave. This new effect is fundamentally different from the Faraday, Cotton-Mouton and the polar, longitudinal and transversal magneto-optical Kerr effects. From our experimental data we can estimate the order of magnitude of the effect as $\chi^{(3)}/n \approx 10^{-4}$, where n is the refractive index and $\chi^{(3)}$ is a component of the dielectric tensor of the medium.

- The first auxetic materials with a negative Poisson's ratio that have micro- and nanoscale periodicity. These planar auxetic structures possess the distinct mechanical property of expanding laterally upon being stretched. Fabricated by structuring nanoscale plasmonic films supported by dielectric nanomembranes, these materials exhibit negative Poisson's ratios between -0.3 and -0.5 under uniaxial tension or compression. In contrast to conventional materials, stretching or compression of auxetics provides an opportunity where both the aspect ratio of the unit cell and its corresponding optical anisotropy (or isotropy) can in principle remain unchanged. Infrared and optical spectra of these structures show plasmonic resonances, indicating that such materials could act as novel nanomechanical light modulators.

- The first nanofabrication method for ultrathin free-standing gold metasurfaces with identical optical properties for opposite directions of illumination. These metasurfaces enable coherent control of light with light. Due to deeply subwavelength thickness of the free-standing plasmonic metasurface and its symmetry with respect to the light propagation direction, the light-matter interaction of such a metasurface can be controlled by placing it in a standing wave and changing the position of the metasurface relative to the nodes of the standing wave. Coherent control of absorption of light with up to THz bandwidth and down to single photon intensities for applications from all-optical logical operations to image processing has been demonstrated.

In summary, this thesis introduces novel solutions for controlling light with plasmonic metasurfaces by exploiting mechanical reconfiguration of nanomembrane metamaterials and coherent control of light with light on metasurfaces. These complementary approaches can be applied to various metamaterials, enabling the development of electrically, magnetically and optically controlled active metadevices for optoelectronics, nanophotonics and plasmonics.

Contents

List of Figures

List of Tables

DECLARATION OF AUTHORSHIP

I, João Pedro Mire Dores Pulido Valente, declare that the thesis entitled "Controlling Light with Plasmonic Metasurfaces" and the work presented in this thesis are both my own, and have been generated by me as the result of my own original research. I confirm that:

- this work was done wholly or mainly while in candidature for a research degree at this University;
- where any part of this thesis has previously been submitted for a degree or any other qualification at this University or any other institution, this has been clearly stated;
- where I have consulted the published work of others, this is always clearly attributed;
- where I have quoted from the work of others, the source is always given. With the exception of such quotations, this thesis is entirely my own work;
- I have acknowledged all main sources of help;
- where the thesis is based on work done by myself jointly with others, I have made clear exactly what was done by others and what I have contributed myself;
- parts of this work have been published as the journal papers and conference contributions listed in Appendix B.

Signed: _____

Date: _____

Acknowledgements

The scientific achievements that make up a PhD thesis are only possible in collaboration with other people. I would like to acknowledge their contribution, namely:

- Prof. Nikolay I. Zheludev and Dr. Eric Plum, my supervisors, for their guidance, the freedom to explore my own ideas and useful scientific discussions.
- Dr. Jun-Yu Ou for focused ion beam milling and electrical measurements training and Envangelos Atmatzakis for helping me with COMSOL modelling. I also enjoyed and benefited from experimental collaborations regarding coherent control of light with light. Dr. Venkatram Nalla, Maria Papaioannou and Charles Altuzarra, amongst other co-authors, performed experiments on samples I fabricated.
- Dr. Carlos Nunes de Carvalho, Dr. Guilherme Lavareda and Dr. Killian Lobato for planting the seed of knowledge in me at an early stage of my career.
- My family, especially my grandparents, parents and sister, who unconditionally supported and encouraged me to become a scientist. Since my first steps the support was immense, the belief staggering and the love unconditional.
- Dr. Botsinis, Dr. Cilibrizzi, Dr. Katis, Dr. Parreira, Dr. Zisis, Aabid, Afonso, Filipe, Gonçalo, Joni, Mara, Niko(s), Nuno, Rui, Stan, Tasos, Vagelis, Zé, BDC thank you, above all, for your friendship.
- Francesca, my light and love, for her support, affection and shared emotions.
- All other friends, not mentioned by name, who surely know they were part of this road.

Support from the UK's Defence Science and Technology Laboratory (DSTL) through the national PhD scheme (grant DSTLX1000064081) is gratefully acknowledged.

Chapter 1

Introduction

Engineering of optical materials has generated dramatic scientific progress with enormous impact in our economy and society. Examples include the fibre optic communication network powering the internet, optical data storage, lasers, light emitting diodes (LEDs) and modern display technologies. Extreme purification of natural materials (e.g. silica), investigation of a large range of available optical materials (e.g. gain media) and theoretical advances in material science have contributed to the globalization of such products across our entire society. However, now natural media are reaching limits (such as the diffraction limit and the positive refractive index of natural materials) affecting our ability to progress further. Metamaterials offer solutions for overcoming some, if not all, of these physical limitations. Their research and understanding can fuel further technological and scientific development in optics, photonics and optoelectronics.

Metamaterials are a young class of structurally engineered materials or composites, which has enabled striking developments in electromagnetic wave control and manipulation [1]. Main advantages of metamaterials are the possibility of attaining electromagnetic responses not found in natural media [2,3], enhancing natural electromagnetic effects [4] and achieving control over light-matter interactions [5]. These advantages enable the manipulation of electromagnetic waves at will by engineering the effective electromagnetic parameters of the metamaterial, i.e. the permittivity (ϵ_{eff}) and permeability (μ_{eff}). In order to control such parameters, metamaterials must be made out of structures (metamolecules) of sub-wavelength size so that the electromagnetic

wave perceives them as effective media. While for the lower frequency part of the electromagnetic spectrum (i.e. microwaves or terahertz waves) the required fabrication processes are well developed and fully controlled, several challenges still exist in case of metamaterials for the optical part of the spectrum. In order to interact as an effective medium with visible and near infrared wavelengths, the metamolecules that make up the metamaterial must be fabricated at nanometre scale. Therefore, new techniques and metamaterial architectures must be developed and realized in order to attain high quality and more complex structures. Moreover, reconfiguring and tuning optical properties of such optical metamaterials will require practical and simple ways of either changing size/structure of the metamolecules using nanoscale forces, or directly controlling the metamaterial's interaction with light. These are the main challenges tackled in this work.

Here, we explore the novel concepts, known as structurally reconfigurable metamaterials and coherent control of metasurfaces, and take metamaterials fabrication forward to allow better control of the interaction of metamaterials with infrared and visible light. From careful metamolecule design to optimization of fabrication processes and new experimental setups, this work places itself at the cutting edge of nanotechnology. Finally, reconfiguring photonic metamaterials to achieve continuous and reversible changes of their optical properties promises practical solutions for active optical components while controlling absorption of metasurfaces with two light beams could enable optical computing.

1.1 Motivation

Metamaterials have been around for about 15 years and many novel properties and functionalities, such as negative refractive index or asymmetric transmission, have already been demonstrated [2, 3, 5–9]. However, most are based on resonant characteristics, making metamaterials narrow band and limiting their applications. Therefore, new solutions to tune their optical properties (band broadening) and nanoscale fabrication improvements that enable us to do so are important challenges that remain to be addressed. In this way, metamaterials can become powerful competitors for optical components, optical circuitry and introduce themselves to novel applications. Moreover,

as most commercial and military applications lie in the optical part of the spectrum (optical communications, camouflage, cloaking, optical data processing, data storage) a flexible platform providing tuneable metamaterial properties at optical frequencies is needed. The ability to control the optical properties of metamaterials at will, could bring metamaterials from a conceptual stage to useful metadevices. For such ideas to become a reality, finding ways to dynamically control light with metamaterials and metasurfaces in a simple and practical manner achieving high levels of contrast and modulation frequency is compulsory. We will exploit two physical principles in order to target these goals. Structurally reconfigurable metamaterials based on silicon nitride membranes provide a simple platform for achieving both, high contrast and high modulation frequencies, while coherent all-optical control of light-matter interactions at a metasurface, in theory, can achieve 100% contrast at ultrafast speeds. Moreover, such platforms may also allow the implementation of silicon based technologies easing the fabrication of more and more complex structures, while integration in silicon photonics and plasmonics would be facilitated. With total control over photonic metamaterial properties, holographic "displays", telecommunications demultiplexers and cloaking devices could be developed and metamaterial technology could become widely applied.

In this work we target reconfiguration of metamaterials, in a way that is practical for implementation into metadevices. Taking advantage of well established silicon based technologies and by using simple physical concepts, i.e. Lorentz force actuation, dynamic control over the optical properties of metamaterials and metasurfaces can be achieved. Demonstration of the practicality of structurally reconfigurable metasurfaces, their huge potential for enhancement of magneto-electro-optical effects and realization of metasurfaces for light with light control are the main objectives of this work. Moreover, in order to bring metamaterials and metasurfaces to metadevices, high resolution and high precision nanostructures are mandatory, requiring optimization of nanoscale fabrication processes. By exploring new physical concepts and using new or optimized fabrication processes, one can envision different applications, study new phenomena and implement novel experiments. The motivation for this work is both technological through the development of fabrication techniques and solutions for tuning of metasurface's optical properties, as well as scientific, through unveiling more of the already so rich electromagnetism of metamaterials.

1.2 Metamaterials and Metasurfaces

The prefix "meta" (from Greek - $\mu\epsilon\tau\alpha$) means "beyond" and, therefore, metamaterials can be considered as materials with properties that go beyond what we can find in nature. In other words, by combining and structuring different materials, enhanced and novel properties can be obtained. For metamaterials, rather than the chemical composition of molecules or atoms, it is the physical structure of the metamolecules which is the origin of their remarkable properties.

The first person to link structural composition and electromagnetic properties in composite media was J. C. Bose in 1896 [10, 11]. In his reports, using a book with interleaved thin metal foils, Bose observed linear polarizing properties for this composite medium. Bose placed the composite material (book with metal foils) between the radiating box and the receiver, setting up the apparatus presented in Figure 1.1. Bose analysed how the polarization was changed when electromagnetic waves travel through the medium. This was the first observation on how optical properties change due to

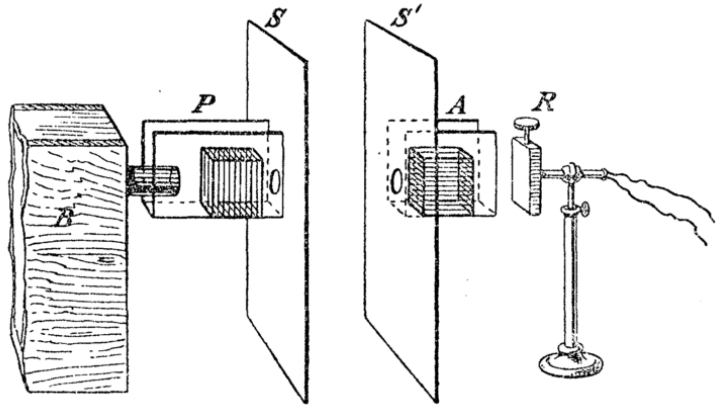

Figure 1.1: ***Bose's polarization experimental apparatus.*** *Experimental apparatus consisting of a radiating box B (horizontal platinium spark-gap radiator), polariser P (square pieces of thick copper), analyser A (square pieces of thick copper), screens S and S'and receiver R (sensitive spirals circuit) [11].*

structural composition. However, his pioneering work only gained practical importance with the development of wireless communication and radar technology. During the Cold War scientists looked deeply into frequency selective surfaces for radar applications [12–14]. Nowadays, frequency selective surfaces are used in dichroic reflectors, antennas [15], broadband communications, stealth applications and terahertz technology [16–18].

The term "metamaterial" first appeared in the literature in 2000 when Smith *et al.* published a seminal paper on a structured material with simultaneously negative permeability and permittivity at microwave frequencies [2]. This very important paper showed us how by structuring materials or composites, the effective electromagnetic parameters of the metamaterial, permittivity (ϵ_{eff}) and permeability (μ_{eff}), could be engineered. Considering these reports, one can easily envisage how metamaterials can present us the possibility to engineer and design a multitude of electromagnetic responses. A definition of a metamaterial was reported in the book "Optical Metamaterials: Fundamentals and Applications":

"A metamaterial is an artificially structured material which attains its properties from the unit structure rather than the constituent materials. A metamaterial has an inhomogeneity scale that is much smaller than the wavelength of interest, and its electromagnetic response is expressed in terms of homogenized material parameters." [19]

However, many metamaterials are assembled from just slightly sub-wavelength elements and the nanostructures considered here are very thin compared to the wavelength, which make the use of homogenized material parameters problematic. Therefore we will use the following more general definition:

"Metamaterials are sub-wavelength structured materials or composites perceived by electromagnetic waves as an effective medium, therefore attaining unusual electromagnetic properties."

Considering these definitions, a metamaterial reveals it uniqueness by its man-made structure, consisting of sub-wavelength unit cells with their own electromagnetic properties. Placed in arrays, the characteristics of these tiny metamolecules will combine in such a way that a homogeneous (non-diffracting) electromagnetic response can be attributed to the resultant metamaterial. Ultimately, such metamaterials can be made with a deeply sub-wavelength thickness, which introduces the concept of metasurfaces. When metamolecules are structured in a deeply sub-wavelength thickness substrate they become the two-dimensional counterpart of metamaterials. For such structures, we cannot assign the usual effective parameters to the surface since, for example, an effective refractive index only has physical meaning when there is a medium to travel through. In such designed surfaces, dimensions of the constituent metamolecules might be deeply sub-wavelength only in one direction and the electromagnetic wave inter-

action can be described theoretically based on boundary conditions rather than constitutive parameters [20]. This ideal is best approximated by a single periodically patterned metal layer with a thickness that is comparable to the skin depth, which is the characteristic thickness of the current carrying layer at a conductor's surface. Such nanostructures, due to their sub-wavelength periodicity, do not diffract electromagnetic waves at normal incidence. The transmission and reflection properties of a metasurface can be written in terms of the transmission (t) and reflection (r) matrices, which relate the transmitted and reflected electric fields, $\mathbf{E^t}$ and $\mathbf{E^r}$, to the incident field $\mathbf{E^0}$. Considering a forward propagating incident wave (indicated by the arrow over the matrix), these relations can be written as,

$$\overrightarrow{\mathbf{E}}^{\mathbf{t}} = \overrightarrow{t}\,\overrightarrow{\mathbf{E}}^{\mathbf{0}}, \tag{1.1}$$

$$\overrightarrow{\mathbf{E}}^{\mathbf{r}} = \overrightarrow{r}\,\overrightarrow{\mathbf{E}}^{\mathbf{0}}. \tag{1.2}$$

Due to their deeply sub-wavelength thickness, metasurfaces can be also regarded as a 0 thickness discontinuity which will scatter electromagnetic waves. Therefore, it is convenient to express transmission and reflection in terms of the scattering matrix, s. As a metasurface is just a non-diffracting array of scatterers, the transmitted field is simply the superposition of the scattered field and the incident wave, as represented by,

$$\overrightarrow{t} = \overrightarrow{s} + 1, \tag{1.3}$$

where 1 is the unit matrix. Also, metasurfaces can only couple to tangential electric fields and normal magnetic fields. Coupling to normal electric fields and tangential magnetic fields is not possible, as the electric charges cannot leave the plane of the structure. Consequently, two electromagnetic waves that do not differ in these field components must excite the metasurface in the same way. Particularly, the electric field radiated by a metasurface (or planar current configuration) must be symmetric with respect to the nanostructure. This is why the scattering matrix in the reflection direction differs from the scattering matrix in the transmitted one by a coordinate

transformation. The reflection matrix for forward propagating incident waves is,

$$\overrightarrow{r} = \overrightarrow{s}, \tag{1.4}$$

if the matrices describe normally incident linearly polarized basis states relative to a coordinate system that is fixed to the lab (coordinates do not depend on the wave propagation direction). For a metasurface, transmission and reflection matrices are linked by equation 1.3 and equation 1.4. Therefore, metasurfaces can be described in terms of their scattering properties, represented by the scattering matrix of the array of metamolecules, s. The scattering properties for opposite directions of incidence onto a metasurface are linked by Lorentz reciprocity [21] and therefore the scattering, reflection and transmission matrices for opposite directions of illuminations (arrows) take the following form:

$$\overrightarrow{r} = \overrightarrow{s} = \begin{pmatrix} a & b \\ c & d \end{pmatrix} \quad \text{and} \quad \overleftarrow{r} = \overleftarrow{s} = \begin{pmatrix} a & c \\ b & d \end{pmatrix}, \tag{1.5}$$

$$\overrightarrow{t} = \begin{pmatrix} a+1 & b \\ c & d+1 \end{pmatrix} \quad \text{and} \quad \overleftarrow{t} = \begin{pmatrix} a+1 & c \\ b & d+1 \end{pmatrix}. \tag{1.6}$$

Upon interference of the incident electromagnetic wave with the scattered field of the metasurface, a new electromagnetic wave shape in terms of intensity, phase and polarization is produced. The electromagnetic response of metamaterials and metasurfaces is controlled by plasmonic excitations within the metamolecules and coupling of electromagnetic responses (plasmons) within the array. In Figure 1.2, these steps are schematically explained. Each individual metamolecule is excited by the incoming electromagnetic wave (Figure 1.2 a)) and characteristic plasmonic resonances of the structure (metamolecule) will be present. Metamolecules can support a quasi-static electrical resonance,

$$\omega_r = \frac{1}{LC}. \tag{1.7}$$

In this case, the resonant frequency (ω_r) can be controlled through the inductance (L) and capacitance (C) of each individual metamolecule. However, when characteristic

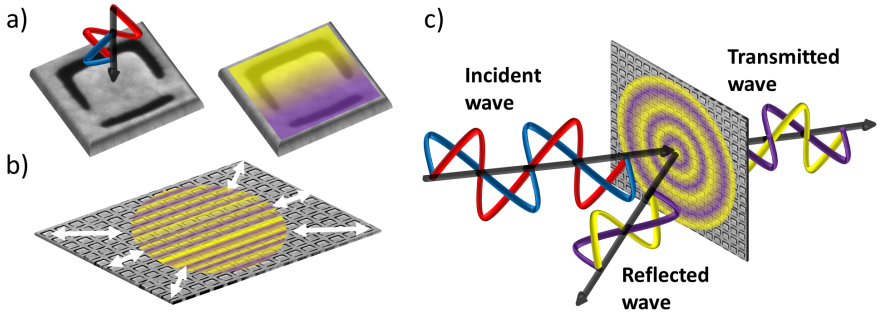

Figure 1.2: ***Metamaterial optical properties.*** *a) Plasmonic excitation within the metamolecule by the incident wave - electric field (blue wave), magnetic field (red wave) and plasmonic oscillation (purple and yellow stripes). b) Electromagnetic coupling of metamolecules within the array - expansion of the plasmonic oscillation (purple and yellow stripes). c) Incident wave interaction [electric field (blue wave), magnetic field (red wave)] with a metamaterial and resultant electromagnetic waves: coupling (purple and yellow stripes), reflection and transmission [electric (purple wave), magnetic field (yellow wave)].*

sizes of the structure correspond to a half-integer multiple of the effective wavelength, a geometrical resonance can also be excited,

$$\lambda_{r,N} = \frac{\sqrt{\epsilon^*} l}{(N+1)}, \tag{1.8}$$

where ϵ^* is the resonator's effective permittivity and N a positive integer. In such structures, the characteristic length of an individual metamolecule (l), controls the free space wavelength of the resonance ($\lambda_{r,N}$). These resonances control the way electromagnetic energy is distributed within and scattered by the metasurface. When electromagnetic radiation interacts with plasmonic sub-wavelength structured metamolecules, electrons in the conduction band of the constituent material will start oscillating creating plasmons. A plasmon is a quasi-particle resulting from the quantization of plasma oscillations. These oscillations will occur inside the solid by transfer of linear momentum and energy from the electromagnetic wave to the solids' free electrons. Due to the electromagnetic interaction between metamolecules, a coupled electromagnetic response is produced (Figure 1.2 b)) resulting in the characteristic electromagnetic response of the metamaterial or metasurface array. The interaction energy from coupling two dipoles together, either electric or magnetic ones, can be derived considering a simple quasi-static picture [22]. For instance, let us consider a first approximation where only the dipole-dipole interaction is considered, although higher-order multipoles can play

a substantial role in metasurfaces [23, 24]. If two dipoles with dipole moments p_1 and p_2 (either electric or magnetic) interact at centre-to-centre distance r, the quasi-static interaction energy Q_{int} is given by [25],

$$Q_{int} = \iota \frac{p_1 \cdot p_2}{4\pi\epsilon_0 r^3}, \tag{1.9}$$

where r is the distance between p_1 and p_2 and ι is the interaction index, which is +1 when considering purely transverse coupling or -2 for longitudinal coupling of the two dipoles with magnitudes p_1 and p_2. From equation 1.9 the interaction energy of the coupled metamolecules (dipoles) strongly depends on the distance (r) between them. This indicates that by displacing metamolecules relative to each other, the coupling energy can be tuned and the overall optical properties of the metasurface changed. Now, if the plasmon oscillations are coherent and at an interface between two materials (at which the dielectric function changes sign), surface plasmons can be created and will propagate along the interface. The coherent oscillation of plasmons travels through the medium and can either be radiated into the free space by coupling to a photon or be absorbed, depending on the the symmetry of the plasmonic mode. Coupling of metasurface plasmons to propagating photons results in the scattered field (intensity, polarization or phase). The coherent plasmonic scattering response will interfere with the incident electromagnetic wave of the metamaterial or metasurface. This new output electromagnetic response results from the overall electric and magnetic field interaction between the input electromagnetic wave and the electromagnetic characteristic response of the array, see Figure 1.2 c). In this way, waves transmitted and reflected by a metamaterial or metasurface are formed. In summary, after travelling through a metasurface, the initial electromagnetic wave will be changed by the scattered electromagnetic field produced by the metasurface. This scattered field results from the coupled plasmonic response of each individual metamolecule, see Figure 1.3.

Moreover, metamaterials and metasurfaces are scalable, meaning that any property demonstrated for microwave or terahertz spectral range can, in principle, be brought to the optical range just by shrinking the metamolecule dimensions and making the miniaturized structure interact with radiation of appropriately scaled wavelengths (provided that the properties of the constituent materials are similar in these spectral ranges).

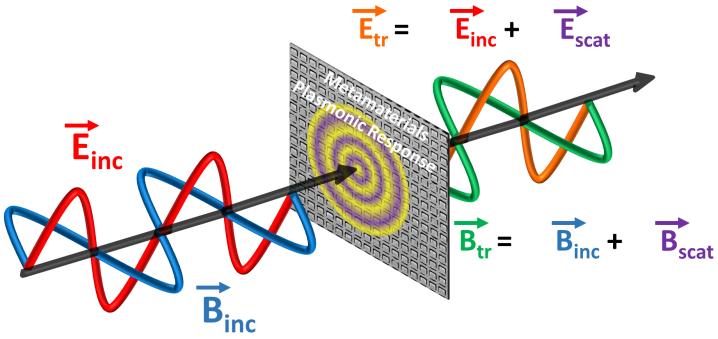

Figure 1.3: ***Transmission of light by a metasurface.*** *Incident electromagnetic waves interact with a metasurface and excite its plasmonic response which will radiate a scattered field. The resultant transmitted electromagnetic wave after metamaterial interaction is composed of the sum of the incident electric (magnetic) field and this electric (magnetic) scattered field.*

In order to bring metasurfaces to the optical part of the electromagnetic spectrum, not only the distance between metamolecules must be smaller than the incident wavelength, but also deeply sub-wavelength thicknesses are imperative. Nanoscale structures must be designed and fabricated with details usually only a few nanometres in dimension. Therefore, structuring of nanoscale metamolecules to form metamaterial and metasurface arrays must be accurately done to achieve a homogeneous electromagnetic response of the structure with unique electromagnetic properties. Latest technological developments in nanofabrication and nanoprocessing, for example focused ion beam technology and electron beam lithography, are suitable. In addition, these technologies already shown to provide high resolution nanostructures and some silicon processing technologies are being used increasingly to enable more complex structures. However, optical metamaterials and metasurfaces still face an enormous challenge in order to become useful for a wider range of practical applications: their properties are usually fixed and limited to a single wavelength (narrow band). Dynamic control over metamaterial or metasurface functionalities via external signals would unlock major opportunities for science and applications. Such applications might include tuneable spectral filters (any wavelength) for communications, ultra-small optical modulators for miniaturized optical signal processing, colour-changing camouflage surfaces, adaptable cloaks and programmable transformation optics devices. In the next section, tuneable metamaterials and metasurfaces for active control of visible and infrared light are discussed and the state of the art is reviewed.

1.3 Control of Light with Metasurfaces

Metasurfaces and metamaterials can exhibit remarkable properties, however, their usefulness for practical applications would greatly benefit from dynamic control over their optical properties. If narrow band metasurface functionalities could be dynamically tuned and/or broadened, metasurfaces could become a major technology in optics, photonics and plasmonics. Moreover, dynamic control over metasurface optical properties could enable control over light at will. Several ways of realizing tuneable metamaterials have been suggested and explored in the microwave, terahertz and optical parts of the spectrum. Different physical principles can be behind dynamic control of metamaterial properties which promises a radical expansion of photonic functionalities.

Tuneable microwave metamaterials have been realized by including non-linear electronic components like varactors [26] or exciting a metamaterial with different profiles of visible light illumination [27]. For example, Ilya V. Shadrivov [27] introduced and experimentally demonstrated the concept of functional metamaterials whose properties are externally controlled using visible light. In such metamaterials effective material parameters for microwaves are locally controlled by a handcrafted illumination profile. Such metamaterials will, therefore, attain arbitrary gradients of the effective material parameters by tuning the magnetic resonance of light-tuneable magnetic metamolecules. The adjustment in metamaterial properties is achieved by controlling the permittivity (ε_{eff}) or the permeability (μ_{eff}) of the effective material and thus the refractive index n, following the relation: $n = \pm\sqrt{\varepsilon_{\text{eff}}\mu_{\text{eff}}}$, where n becomes negative if both ε_{eff} and μ_{eff} are simultaneously negative.

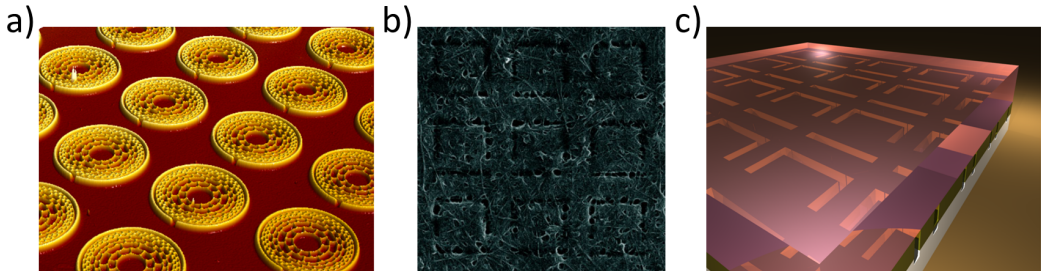

Figure 1.4: ***Tuneable metamaterials.*** *Different concepts for achieving tuneability in metamaterials: a) superconducting metamaterial [28], b) metamaterial containing nonlinear carbon nanotubes [29], c) phase change metamaterial containing a layer of chalcogenide glass [30].*

Superconducting metamaterials were used in the microwave and sub-THz regimes allowing tuning of optical properties upon temperature changes [31, 32], Figure 1.4 a). Savinov *et al.* [32] fabricated a niobium metamaterial consisting of an interlinked two-dimensional network of subwavelength resonators connected by a continuous superconducting wire loop, to dynamically modulate sub-terahertz radiation. The main mechanisms of modulation correspond to the suppression of the superconductivity in the network by magnetic field, heat and electrical current. A superconductor material is characterized by having an Ohmic-lossless regime below a critical temperature, magnetic field and current. Resistive heating due to applied currents above the critical current increases the metamaterial temperature above and then the metamaterial's optical properties become highly dependent on the electric current applied. Therefore, by changing the temperature of the superconductor around the transition temperature, the authors were able to tune optical properties of superconducting metamaterials.

At terahertz and optical frequencies, the use of nonlinear media [29, 33–35] (Figure 1.4 b)), phase change materials [30, 36, 37] (Figure 1.4 c)), or liquid crystals [38–42] has been reported as means for achieving tuneable electromagnetic properties. Phase change materials [30, 36, 37] can offer a solution when considering tuning of optical properties for near-infrared to visible light. Utilizing vanadium oxide (VO_2), which has a metal-insulator phase transition as substrate for metamaterial structures, Dicken *et al.* [37] demonstrate frequency-tunable metamaterials in the near-IR range, from 1.5 to 5 μm wavelength. Arrays of Ag split ring resonators were patterned with e-beam lithography onto planar VO_2 and etched via reactive ion etching to yield an Ag/VO_2 hybrid system. FTIR reflection data show that the resonant peak position red-shifts upon heating above the phase transition temperature. Tuning of the system's optical properties around the phase change temperature was demonstrated. Another work using phase change materials was reported by Samson *et al.* [30]. Authors exploited the frequency shift of a narrow-band Fano resonance mode in a plasmonic planar metamaterial induced by a change in the dielectric properties of a superstrate chalcogenide glass layer. An electrically stimulated transition between amorphous and crystalline forms of the glass brings about a 150 nm wavelength shift in the near-infrared resonance providing transmission modulation with a contrast ratio of 4:1 in a device of subwavelength thickness.

Liquid crystals have been employed along with metamaterials for infra-red wavelengths [38, 40, 42]. I. C. Khoo *et al.* [38] analysed aligned nematic liquid crystal cells containing core-shell nanospheres and have shown that it is possible to devise a new type of metamaterial whose index of refraction is tuneable from negative, through zero, to positive values. Practical realization of such structures was not presented but the authors claim that the design parameters can be scaled for application in the optical spectral region. Werner *et al.* [40] claim that tuneability can be achieved by cladding thin layers of liquid crystal both as a superstrate and a substrate on an established negative-index metamaterial. By adjusting the permittivity of the liquid crystal, the index of refraction for the proposed structure can be changed over the range from -1 to +1.8. Another work developed with liquid crystals was reported by Buchnev *et al.* [42]. The authors fabricated a liquid crystal cell containing a metamaterial structure as an electrode. In response to voltage application to the cell, the liquid crystal will change its orientation and allow electromagnetic waves to interact with the metamaterial electrode resulting in a characteristic electromagnetic resonance.

Tuneable metamaterials and metasurfaces based on established micro electromechanical systems (MEMS) have been demonstrated for terahertz frequencies [43–46], see Figure 1.5. Such tunable metamaterials can be denoted as structurally reconfigurable metamaterials since the change in optical properties arises from structural displacements and geometry changes within the design. In this work we use the shortened terms reconfigurable metasurfaces and reconfigurable metamaterials to refer to structurally reconfigurable metasurfaces and metamaterials. Reconfigurable anisotropic metama-

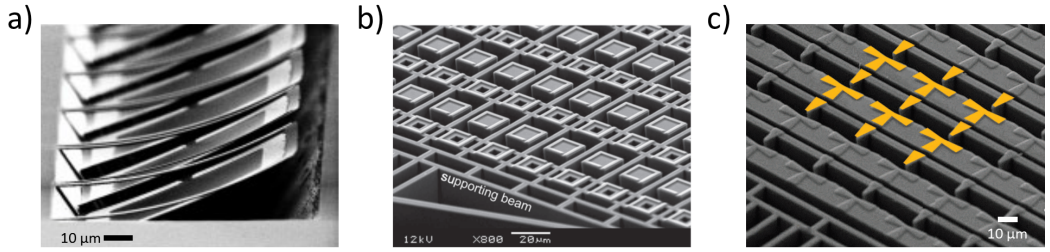

Figure 1.5: ***Tuneable MEMS metamaterials for THz waves.*** *a) Reconfigurable anisotropic metamaterial design that bends out of plane in response to a thermal stimulus [43], b) Wide tuning of resonant frequency via reconfiguration of asymmetric split-ring resonators [44], c) Maltese-cross metamaterial with tuneable anisotropy [46]. The latter two structures are electrically driven by comb drive actuators.*

terials at terahertz frequencies by reorientation of metamolecules within unit cells in response to an external stimulus were demonstrated by Tao *et al.* [43] (Figure 1.5 a)). Bimaterial cantilevers designed to bend out of plane in response to a thermal stimulus, present marked tuneability of the electric and magnetic responses. More recently, Fu *et al.* [44] (Figure 1.5 b)), reported a micromachined reconfigurable metamaterial where tuneability is achieved by adjusting the distance between asymmetric split-ring resonators. M-comb drive actuators (electrostatic actuation) are used to move a part of each split ring that is supported by a movable frame, while the position of the other part of the split rings remains fixed. Therefore, the strength of dipole-dipole coupling between metamolecules can be continuously tuned tailoring the electromagnetic response of the metamaterial. Finally, Zhu *et al.* [46] (Figure 1.5 c)), demonstrated a terahertz metamaterial with tuneable anisotropy. Based on the Maltese-cross pattern and by breaking its four-fold symmetry, anisotropy is induced and can be tuned from positive to negative values. Similarly to previous works, bidirectional in plane displacement of carrying metamolecule beams (or parts of it) is achieved using electrostatic MEMS actuators. The main idea behind the utilization of the MEMS platform to achieve tuneability relies on the control of coupled interactions between metamolecules, as discussed before in this chapter. This platform, not only suits tuneability since it is able to induce movement of micro- and nanoscale parts of a structure but it also benefits from fabrication processes and technologies developed for electronics which, nowadays, are fully controlled and understood.

Another widely explored concept to achieve tuneability in metamaterials was stretch-based systems [47–49] where mechanical actuation of metamaterials results in tuning of their optical properties, see Figure 1.6.

Firstly, reconfigurable metamaterials using high-strain mechanical deformation of an elastomeric substrate to controllably modify the distance between their resonant elements were reported [47]. In this work, the authors achieved 180 fold enhanced reflection and manipulation of resonator components is also used to tune and modulate the Fano resonance of a coupled system at terahertz frequencies. This result is obtained by stretching the substrate which changes the dimensions of the metamaterial structure and therefore also the coupling between resonators. At optical frequencies and using gold nanoparticle dimers, active tuning of surface plasmons on stretchable

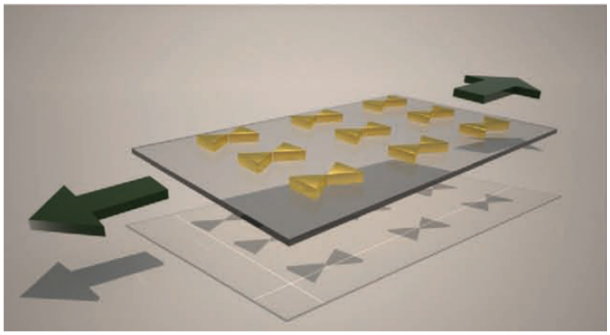

Figure 1.6: ***Stretchable tuneable metamaterial.*** *Application of a load to an elastic substrate supporting metal resonators results in electromagnetic tuning of the metamaterial [49].*

elastomeric films could be realized by Fumin Huang [48]. Reversible stretch-tuning of the metal dimer spacing on the nanometre scale reveals radically different spectral tuning than previously reported for sub-10-nm nanoparticles, since the resonant peak position remains unchanged when perpendicular polarized light is shone upon the dimers. For light polarized along the dimers, the resonant peak position red shifts exponentially with decreasing dimmers gap. Finally, interesting work has been carried out by Aksu *et. al* [49] on the realization of electronic and photonic components on flexible, stretchable, nonplanar, and biocompatible substrates. In their work, authors review fabrication technologies and results on such platforms and develop a new method that can enable single-step, high-throughput, high-resolution and large-area fabrication of nanostructures on flexible and elastomeric substrates at dimensions relevant for nanophotonics, plasmonics, and metamaterials. For a complete overview on tuneable metamaterials, Jingping Zhong [50] and A. Q. Liu *et al.* [51] published detailed reviews.

In all previous mechanisms there are drawbacks regarding scaling/application to visible/infra-red radiation. Superconductors do not operate at optical frequencies, large nonlinear effects require high intensities and the existing MEMS metasurfaces and metamaterials are far too complex for the 100-fold size reduction needed. Liquid crystals, in turn, tune the electromagnetic incident wave on the metasurface, however, this mechanism is slow (microseconds to milliseconds) and highly dependent on the liquid crystal used. Similarly, phase change materials are highly dependent on the material properties (i.e. transition temperature) and tuneability is achieved through

manipulation of the incident light. Finally, in stretchable metamaterial systems high frequency actuation is not possible due to the need of macroscopic displacement of a high mass (entire metamaterial) of low-stiffness material.

Another way of enabling dynamic control of light resides in the light-matter interaction of a metasurface that is thin compared to the wavelength of interaction. Wave plates [52,53] as well as polarization rotator and circular polariser [54,55] functionalities have been demonstrated in metamaterials of essentially zero thickness and also gratings and Fresnel zone plates can be realized as a layer that is thin compared to the wavelength. Recently, Capasso [20] and others [56–64] demonstrated that the propagation direction of light can also be controlled by phase gradient metasurfaces, where spatially varying resonators on an interface scatter with different phases. The effects underlying the functionalities of metasurfaces can be divided into two categories: dispersion phenomena including narrow resonances, stop bands and EIT-like behaviour on one hand, and polarization phenomena such as optical activity, linear birefringence and circular conversion dichroism on the other hand. For a full review on metasurfaces and control of light with them, see Nanfang Yu and Federico Capasso [65].

While these are powerful solutions for static wavefront control, they cannot offer dynamic control over light propagation. However, instead of modifying the metasurface, active control of light can be achieved by controlling the light-matter interaction with an optical control signal [66]. When placed in a coherent light network environment, metasurfaces can manipulate light with light at high speeds and arbitrarily low intensities.

Despite all efforts developed to achieve and improve tuneability of metamaterials and metasurfaces, when approaching visible wavelengths, current solutions become impractical or simply non suitable due to complexity and miniaturization requirements. Here, we will explore possible solutions including reconfigurable metasurfaces driven by electric and magnetic fields and metasurfaces which placed in a coherent control network can actively control light intensity or polarization, to tackle tuneability in a simple and practical manner.

1.4 Thesis Overview

Compared to natural materials, metamaterials provide an opportunity to access a far greater range of optical properties, such as negative, zero or extremely large refractive indices, giant nonlinearities and novel polarization effects. However, these properties are usually static and narrowband. Therefore dynamic control of metamaterial functionalities has become the next big challenge on the route to many applications.

This thesis starts with the present chapter (Chapter 1) consisting on a brief introduction to the work developed and the motivation behind it. Also, a description of the underlying physics and properties of metamaterials and metasurfaces can be found in section 1.2. In the previous section, light control using metamaterials and metasurfaces is generally reviewed. This overview of the document ends the present chapter.

Chapter 2 consists on a more detailed review on solutions for the dynamic control of light with two-dimensional metamaterials which could be mass-produced based on existing technology, metasurfaces and metamaterials. Also, relevant theory concerning the results reported in this work will be reviewed. Therefore, structurally reconfigurable photonic metamaterials (section 2.1), magneto-electro optical effects (section 2.2), auxetic materials (section 2.3) and coherent control of metasurfaces (section 2.4) are discussed. Last but not least, in this chapter, nanofabrication and characterization of metasurfaces are explained in sections 2.5 and section 2.6.

Results supporting the main achievements of this PhD are organized considering the mechanism used to dynamically control light with metasurfaces. Therefore, subsequent chapters in this thesis report on the results achieved by modifying metasurfaces on the nanoscale using electrical, magnetic and mechanical control signals. Moreover, using coherent optical control signals, dynamic control of light was also demonstrated by controlling the light-matter interaction on a metasurface.

In Chapter 3 results on driving optical changes in metasurfaces by actuation of arrays of thousands of meta-molecules with electrical currents and magnetic fields are reported. Exploiting that electrical resistive heating bends nanostructures consisting of materials with different thermal expansion coefficients, active modulation of metasurface optical properties with high contrast was demonstrated.

Also using the magnetic Lorentz force that acts on a current-carrying nanowire

placed in a magnetic field, reconfiguration of a metasurface provides a novel reciprocal magneto-electro-optical effect and magneto-electro-optical modulation of light at high modulation rates of up to hundreds of kHz, see Chapter 4.

In Chapter 5 mechanical and electromagnetic metasurfaces on the nanoscale were merged to demonstrate the first nanoauxetic metasurfaces, paving the way towards mechanically tuneable metadevices that conserve isotropy.

Development of free-standing metasurfaces used in several experiments in a coherent control environment is reported in Chapter 6. Colleagues demonstrate that metasurface properties are crucial in such experiments and I developed suitable fabrication processes to achieve high quality samples for coherent control of metasurface functionalities.

Finally, conclusions drawn from this work are presented in Chapter 7. An Appendix B lists articles and conference contributions published during the work reported in this document.

Chapter 2

Fundamental Concepts

Dynamic control of light can be achieved by several, very distinct methods, as discussed in section 1.3. Here, the state of the art and underlying physics in the fields most relevant to this thesis are introduced in a more focused way in order to place the experimental chapters of this thesis into context. As the same fabrication methods and experimental techniques are relevant to several parts of this work, two final sections of this chapter describe metasurface nanofabrication and characterization. Concretely, section 2.1 presents the state of the art in terms of (structurally) reconfigurable photonic metamaterials and discusses existing challenges related with such systems. Section 2.2 introduces the known fundamental electrooptical, magnetooptical and magneto-electro-optical effects before discussing the novelty of the effect reported in this work. Subsequently, introduction and review of mechanical metamaterials concept is given in section 2.3. Section 2.4 introduces coherent control of light with light on metasurfaces and highlights the crucial importance of sample fabrication. Finally, metasurface nanofabrication is described in section 2.5 where different technologies, such as, thin film evaporation systems and focused ion beam milling are explained. Characterization techniques used in order to obtain the results reported later are discussed in section 2.6. By the end of this chapter, the reader will have the necessary background to better understand the results presented in the experimental chapters that follow and to acknowledge the important steps made in order to push forward the state of the art in dynamic control of light.

2.1 Reconfigurable Photonic Metasurfaces

Tuning of metasurface electromagnetic properties has been widely studied and demonstrated through various mechanisms, as shown in section 1.3. A relatively new field of research targeting the tunability of metasurface optical properties is through structural reconfiguration of the metasurface. Reconfigurable photonic metasurfaces based on MEMS have been realized for THz and sub-THz frequencies [43, 44, 46, 67–69] and recently shrunk to the optical spectral range [70, 71]. In this section we will review the state of the art in reconfigurable photonic metasurfaces inspired in MEMS/NEMS technologies for the visible to near infrared part of the spectrum. Such systems can also be considered structurally reconfigurable metasurfaces since tuning of their optical properties results from structural reconfiguration of the metasurface. Sub-wavelength scale structuring of a noble metal film supported by a dielectric membrane of nanoscale thickness can be used to make mechanically reconfigurable metasurfaces suitable for the optical spectral range. Ou *et al.* demonstrated tunability using 3 different mechanisms of actuation based on this nanomembrane approach [70–72]. Interaction of an electromagnetic wave with a densely populated metasurface, where metamolecules are strongly coupled, will alter the wave by plasmonic phenomena (section 1.2, equation 1.9). In order to achieve tunability in the visible part of the electromagnetic spectrum, authors proposed to manipulate optical metasurfaces by changing the relative arrangement of their plasmonic building blocks, i.e. thousands of metamolecules. Moreover, by constructing their metasurfaces from bi-material layers, i.e. metal on top of dielectric, planar metamaterials which are reconfigurable by ambient temperature or electrostatic actuation were realized. Bi-material layered structures can be actuated by temperature changes based on different thermal expansion coefficients to engage displacement and different layers can provide both a mechanical support (dielectric) and a plasmonic material (metal). Elements of reconfigurable metasurfaces can often be represented as nanowires. At the nanoscale, electromagnetic forces and thermally actuated displacements act on such nanowires and are comparable with elastic forces of the supporting structure. In general, the elastic restoring force of such nanowires

with circular cross-section that are supported on both ends can be described as [73],

$$F_{Elastic} = 6\pi E \frac{D^4}{L^3} x, \tag{2.1}$$

where, E is the Young's modulus, L is the length, D the diameter and x the displacement of the nanowire. Such parameters can be visualized in the Figure 2.1, considering

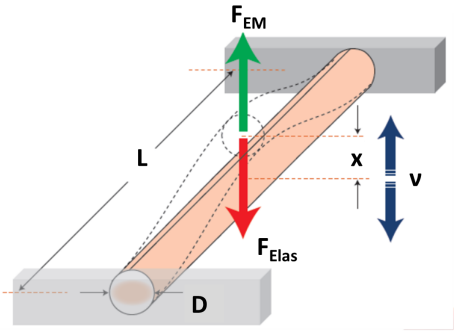

Figure 2.1: ***Elastic force at nanoscale.*** *A nanowire anchored at both ends of length L, diameter D and Young's modulus E. Using an external electromagnetic force F_{EM} it is possible to drive a nanowire against its elastic restoring force at a certain frequency, ν. [73]*

a general design. Using equation 2.1, we can estimate the force needed to achieve displacement.

Ou et *al.* [70] were able to demonstrate the concept of a thermally reconfigurable photonic metasurface, where continuous change of the physical configuration of the nanostructure was achieved. Such structures take advantage of nanomembrane technology, which provides very thin, flexible dielectric substrates. Moreover, evaporation of a plasmonic metal on one or both sides of such substrates allows the fabrication of innovative nanomembrane-based planar metamaterials. As shown in Figure 2.2, this thermally reconfigurable metasurface consisted of an array of plasmonic metamolecules supported by pairs of strings (nanowires) cut from the membrane and designed in a way that one string of the pair exhibited temperature-activated deformation while the other did not. These bridges can be spatially repositioned by changing the ambient temperature. In order to achieve different thermal displacement of neighbouring bridges, half of them are gold-covered on both sides, while the others are only covered by gold on one side. When the temperature of the metasurface changes, only the asymmetrically layered bridges that are gold-covered on only one side will bend due to different thermal expansion coefficients of gold and silicon nitride. The bridges covered from both

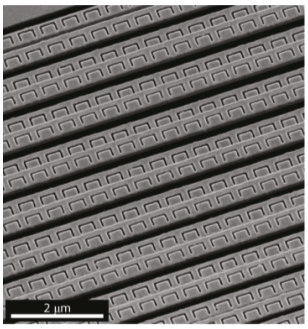

Figure 2.2: ***Thermal reconfigurable photonic metasurface.*** *[70] Reconfigurable photonic metasurface where tunability of optical properties is driven by thermal expansion and achieves up to 50% contrast. Grey colour shows gold-coated silicon nitride bridges while black colour shows bridge gaps and ring resonators milled on the gold-coated silicon nitride bridges.*

sides will remain static since structural symmetry does not allow any displacement. The changing distance between metamolecules or between arrays of metamolecules (bridges) modifies the plasmonic coupling and the electromagnetic response. Despite achieving a fully reversible mechanism to tune metasurface optical properties, this work has the drawback of being slow: the reaction time (time taken to achieve thermal equilibrium), τ, depends on the thermal conductivity of materials involved and the geometry of the string. Reaction time as function of thermal conductivity, κ and string length,L, is given by:

$$\tau \approx \frac{L^2 C_L}{12 A \kappa}, \tag{2.2}$$

where, C_L is the heat capacity per unit length and A the cross-section of the string. Therefore, depending on the capacity of the material to receive heat to achieve certain temperature, its thermal conductivity, the length and the shape of the wires, thermal equilibrium will be achieved at different rates. For metasurfaces with an overall size of tens of micrometers, the response time is typically on the microsecond to millisecond scale. Moreover, such mechanism requires an environment that can provide large temperature changes which increases the complexity of the setup, for example, by requiring a cryogenic sample holder.

Another work by Ou et *al.* [71], exploits electrostatic forces to reposition similar bridges. In this work, the authors developed a new type of metasurface operating in the optical part of the spectrum, for which the operation speed is not limited by the thermal time-scale of the nanostructure. The metasurface is actuated by electrostatic

forces arising from the application of only a few volts to its nanoscale building blocks. The electrostatic force acting on such nanostructures can be approximated by,

$$F_{Coulomb} = \vartheta(D,d)\frac{\pi\epsilon_0 V^2 D}{2d(d-D)}L, \tag{2.3}$$

where, $\vartheta(D,d)$ is a dimensionless parameter that takes value 1 for realistic geometries, D the diameter of the nanowires, d the distance between them, ϵ_0 the permittivity of vacuum and V the applied voltage. The charged plasmonic meta-molecules which

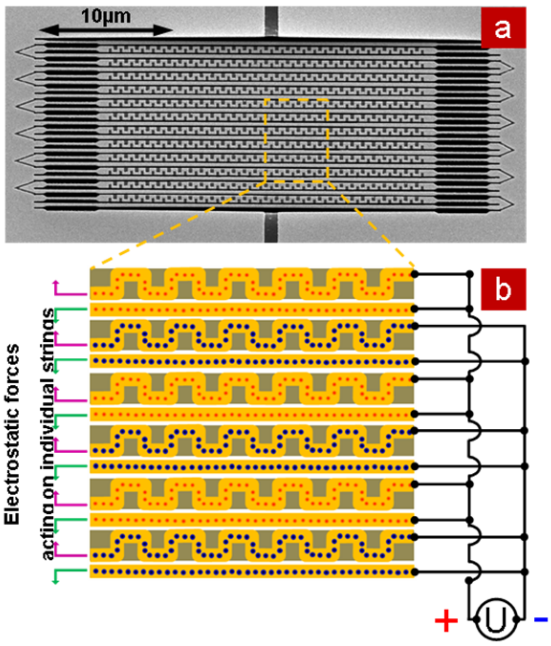

Figure 2.3: ***Electrostatically reconfigurable metasurface.*** *[71] a) Scanning electron microscope image of the device, black colour is the gap and grey the nanoscale bridges; b) Schematic of a section of the metasurface pattern and its driving circuit, where U is the applied voltage, blue dots represent negative charged bridges and red dots positive charged ones. Alternating coloured arrows show the in plane movement of the bridges.*

are supported by pairs of parallel strings cut from a nanoscale thickness flexible silicon nitride membrane move due to electrostatic attraction and repulsion, and thus repositioning of metamolecules is achieved, see Figure 2.3. These strings of picogram mass and only 100 nm thickness can be synchronously driven to megahertz frequencies to electromechanically reconfigure the metamolecules and dramatically change the metasurface's transmission and reflection spectra, thus giving rise to a colossal electrooptical effect. In this work, the elastic properties of the support structure gives access to two different modes of operation: (i) analog tuning, where over a range of voltages the

structure's optical properties can be changed continuously (up to 8% optical signal modulation); (ii) a step-like "digital" change of the optical properties (switching with 250% contrast), where the electrostatic force overcomes the elastic restoring force. Most

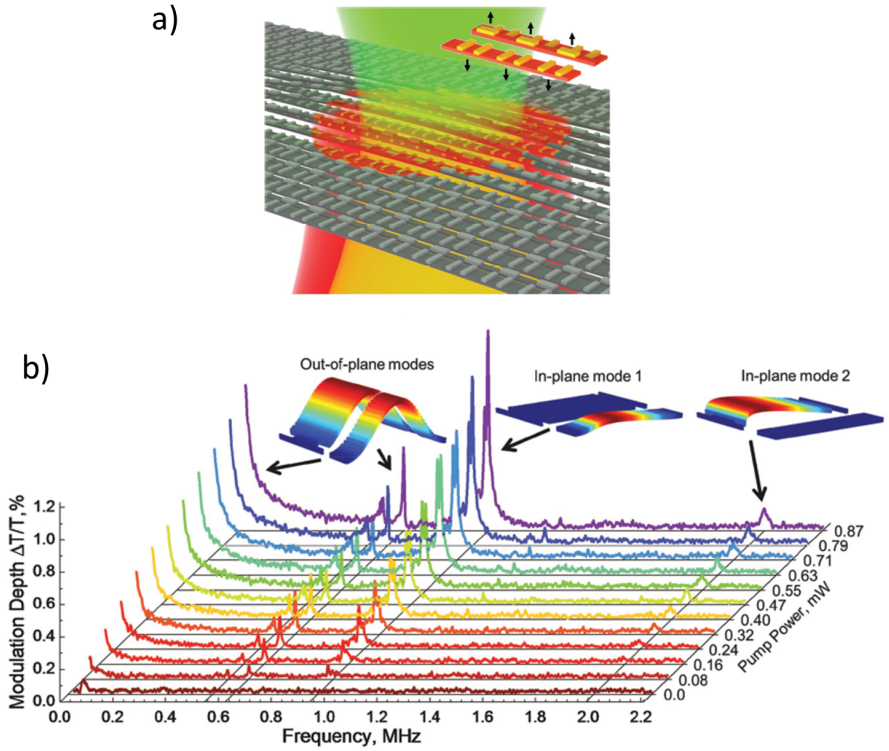

Figure 2.4: ***Optically reconfigurable photonic metasurface.*** *[72] Reconfigurable photonic metasurface where tunability of optical properties is driven by optical forces, a) red beam modulating the green beam at a different wavelength and achieving b). The inset shows how the different constituent bridges move upon optically induced displacement. b) Transmission modulation at the probe wavelength as a function of pump modulation frequency and pump power. Each modulation depth peak has a characteristic mechanical mode identified by mechanical displacement simulations and shown by the insets.*

recently, Ou et *al.* [72], see Figure 2.4, explored optically induced forces that act on a plasmonic metasurface array causing nanoscale reversible displacements of its small and light building blocks. In this work, light induced oscillating dipoles are engaged in order to produce a time-averaged optical force that is proportional to the incident light intensity, I_{light} and the illuminated bridge length L,

$$F_{Optical} \propto I_{light} L. \tag{2.4}$$

Using nanomembrane technology and plasmonic structures, optically-induced forces

drive the nanostructure at up to MHz modulation rates. By using a pump beam (shown red), the authors modulated another, weaker probe beam of light (shown green) at a different wavelength.

However, reported methods have drawbacks. Thermal tuning requires large ambient temperature changes with a complex apparatus, electrostatic actuation engages irreversible structural transitions to achieve significant optical contrast and optical tuning despite MHz modulation rates only reaches few percent of light modulation. Certainly, there are practical actuation signals that can be employed in order to achieve high frequency and high contrast tuning, for example, electrothermal actuation or magnetic fields (Lorentz force). In this work, we will demonstrate that reconfigurable photonic metasurfaces controlled by electrical currents and magnetic fields provide a practical solution for reversible large-range tuning and modulation of optical metasurface functionalities. Taking advantage of the versatility of nanomembrane technology, we will study how magnetic fields and electrothermal mechanisms can be used to actuate such structures. Once more, tunability will be tackled by controlling the metamolecules electromagnetic modes and therefore the coupling between resonators. Changes in the relative position of metasurface components or geometry at the nanoscale will induce strong optical properties changes. As before, our approach takes advantage of the changing balance of forces at the nanoscale, where bilayers of nanoscale thickness bend strongly in response to electrothermal stimulus and weak elastic forces allow the magnetic Lorentz force to cause substantial deformation and, due to large mechanical resonance frequencies of picogram-scale moving parts, allow fast modulation.

2.2 Magneto and Electrooptical Effects

Electro- and magneto-optical phenomena are widely used in several optoelectronic applications, such as electro-optical modulators or magneto-optical isolators. Such phenomena that allow the modulation of optical material properties with external electric or magnetic fields are known as magneto- and electrooptical effects. However, we found a gap in such effects where optical properties of a metamaterial vary linearly and simultaneously with electric and magnetic fields. The aim of this section is to review magnetooptical and electrooptical effects already studied and demonstrated and to

place this new magneto-electro-optical effect into context.

Starting from purely electrooptical effects, we recall the well-known linear electro-optical or Pockels effect [74] of changing or inducing birefringence of crystals in the presence of static electric field **E**. This effect is used in numerous light modulation applications and, in terms of the field-induced correction to the dielectric tensor ε_{ij}, it may be introduced as:

$$\delta\varepsilon_{ij} = \chi^{(2)}_{ijk} E_k. \tag{2.5}$$

By varying the electric field one can change the dielectric tensor and change or induce birefringence in the electrooptical medium. Such variation is linear but it does not depend on the magnetic field. Another example is the electro-optical Kerr effect [75] that is normally observed in isotropic liquids and manifests itself as birefringence proportional to the square of applied electric field and is represented as,

$$\delta\varepsilon_{ij} = \chi^{(3)}_{ijkl} E_k E_l. \tag{2.6}$$

Magnetooptical effects can also be linear or quadratic with the magnetic field. Let us start with the linear magneto-optical effects, i.e. the optical Faraday effect [75] that induces circular birefringence and dichroism for transmission along a longitudinal magnetic field **H** and the polar, longitudinal and transversal magneto-optical Kerr effects [75] that are usually observed for reflected waves, are well known and applications include optical isolators and reading magnetically stored information with reflected light [76]. For all the mentioned effects, the field-induced correction to the dielectric tensor has a linear dependence on the magnetic field expressed by,

$$\delta\varepsilon_{ij} = \chi^{(2)}_{ijk} H_k. \tag{2.7}$$

The quadratic magneto-optical effect of inducing optical birefringence by transverse magnetic field is also well documented and known as the Voigt effect in gases and the Cotton-Mouton effect in solids and liquids [77, 78]. These effects can be described as:

$$\delta\varepsilon_{ij} = \chi^{(3)}_{ijkl} H_k H_l. \tag{2.8}$$

Also known in the literature are phenomena of electro- and magneto-gyration that

describe changes of optical activity in chiral media in the presence of electric and magnetic fields [79, 80] and a non-reciprocal optical magneto-electric effect leading to directional birefringence and dichroism [4, 81–84]. The effect we will demonstrate in Chapter 4 shows its novelty by the way it changes $\delta\varepsilon_{ij}$ when electric E_k and magnetic fields H_l are simultaneously applied. The novel effect is reciprocal with respect to reversal of the light propagation direction. Finally, our reciprocal linear magneto-electro-optical effect may be described as follows,

$$\delta\varepsilon_{ij} = \chi^{(3)}_{ijkl} E_k H_l. \tag{2.9}$$

As all effects mentioned above, when using a metasurface to replicate them, the field-induced correction to the dielectric tensor can be described by a change of the metasurface's scattering matrix.

2.3 Auxetics

The term auxetic is derived from the Greek word *αύξητικός* (auxetikos) which means "that which tends to increase". This terminology has its origin in the first unusual property reported for this class of materials, namely its negative Poisson's ratio. Auxetics are often called mechanical metamaterials and can be found in nature, i.e. certain crystals and rocks, tendons, paper, but are usually man-made in the form of foams, folded sheet materials or composites. Their unusual mechanical properties result from their natural structure or man-made structuring, which makes them the mechanical counterparts of electromagnetic metamaterials. In analogy with the latter, one can design structures to achieve specific mechanical properties not found in nature. Due to their particular internal design, for example, angles, re-entrant shapes, low density and hinge-like areas, auxetic microstructures will flex in particular ways resulting in unusual mechanical properties.

Negative Poisson's ratio [85–88], synclastic behaviour [89] and wave energy harvesting [90] are examples of unique properties that mechanical metamaterials can exhibit. As for electromagnetic metamaterials and metasurfaces different designs and therefore different electromagnetic (mechanical) properties will favour different applications.

Two typical auxetic materials are shown in Figure 2.5 possessing different prop-

erties, negative Poisson's ratio foam (Figure 2.5 a) and b)) and synclastic curvature polymeric material (Figure 2.5 c) and d)). In the first case, the auxetic foam expands (shrinks) in the direction perpendicular to the direction in which it is pulled (compressed). In the second case, auxetic material corners tend to bend inwards and towards each other when a sheet of structured material is indented.

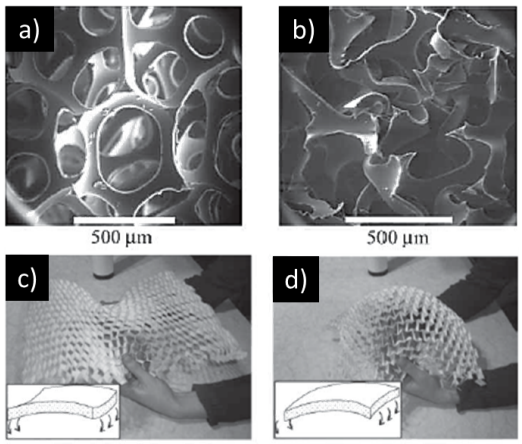

Figure 2.5: ***Auxetic materials with unusual mechanical properties.*** *[91] a) Normal material with positive Poisson's ratio. b) Auxetic material with negative Poisson's ratio. c) Normal material with anticlastic curvature. d) Auxetic showing synclastic curvature.*

In this work we will explore the unusual property of a negative Poisson's ratio, where the Poisson's ratio is defined by Equation 2.10 [92],

$$\nu = -\frac{lateral\,strain}{axial\,strain}, \tag{2.10}$$

where strain relates the dimension changes ΔL of the material to its original dimensions L as follows [93],

$$strain = \frac{extension}{length} = \frac{\Delta L}{L}. \tag{2.11}$$

Numerous auxetic structures were demonstrated theoretically [87, 94] and experimentally studied at millimetre [95], micrometer [96,97] and molecular scales [98]. Such materials and structures are expected to have extraordinary mechanical properties such as high energy absorption and fracture resistance and may be useful in applications such as body armour or knee and elbow pads. Suitable fabrication techniques are determined by the characteristic size of the auxetic structure. For example, macroscopic structures with unit cell dimensions larger than 1 mm were fabricated using open cell polymeric

or metallic foams [85], aramid paper [95], mechanical devices made of hinges, springs, and sliding collars [99], and epoxy resin casting [100]. Soft lithography [97] has allowed fabrication of negative Poisson's ratio structures with characteristic sizes of hundreds of microns, while auxetics with unit cells on the order of 100 μm have been realized by laser micromachining [96]. However, negative Poisson's ratio materials with nanoscale lattice parameters cannot be fabricated using such techniques due to their limited resolution and the complexity of auxetic designs. Nevertheless, nanoscale auxetics would be particularly interesting as optical materials.

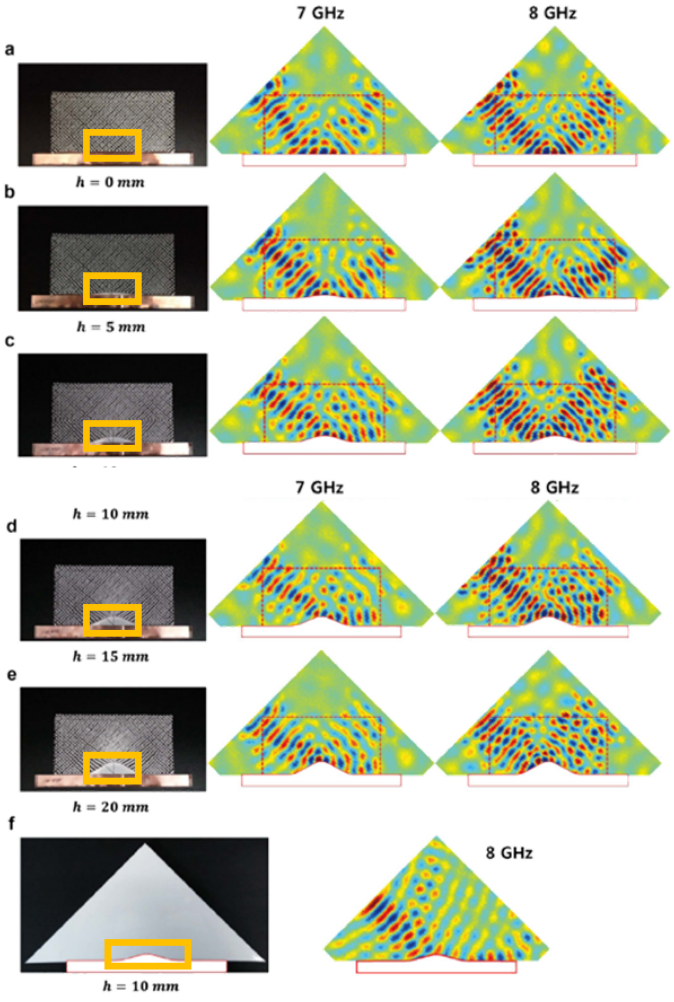

Figure 2.6: ***Experimentally measured E-field maps of a smart cloak [101],*** *where the wave is incident at* 45° *with frequencies of 7 GHz and 8 GHz, while the bump height,* h, *is changed. a)* h = *0 mm, b)* h = *5 mm, c)* h = *10 mm, d)* h = *15 mm, and e)* h = *20 mm, respectively. f) Without an auxetic cloak, a beam incident on the bump of* h = *10 mm in a homogeneous medium of silicone rubber at 8 GHz. A photograph of the sample in each case is given in the first column.*

Interestingly, results on the dielectric properties of auxetic metamaterials [100, 102–106] and their combination with transformation optics concepts, in order to realize better electromagnetic cloaking devices for microwaves [101, 107], have been reported. Shin *et al.* [101] developed smart transformation optics devices where the permittivity distribution of the metamaterial is given by the structure and its deformation. Based on extremely auxetic (Poisson's ratio -1) elasto-electromagnetic metamaterials fabricated devices have shown the ability to deform carpet cloaks, bent waveguides, and potentially other quasi-conformal transformation optics based devices operating at 7-8 GHz. These devices acquire the necessary distribution of effective permittivity entirely from the mechanical deformation of its boundary. In such design, when an object is placed inside the transformation optics device, the cloak will deform elastically giving it the desired effective permittivity distribution, see Figure 2.6.

Instead of 3D macro- and microstructures we can now consider 2D planar auxetics at micro- and nanoscale. Dielectric properties of such auxetic metasurface can be tuned by modifying specific unit cell parameters [100]. Considering the hinging model that relies on stiff structures in both axial and transverse directions, as well as, in elastic deformation only due to angle changes, the Poisson's ratio for both direction ($\nu_{1,2}$ and $\nu_{2,1}$) as function of unit cell parameters (see Figure 2.7) can be described as follows [87]:

$$\nu_{1,2} = {\nu_{2,1}}^{-1} = \frac{sin\theta(\alpha + sin\theta)}{cos^2\theta}. \tag{2.12}$$

Assuming that the planar auxetic is made out of a non-magnetic, homogeneous and isotropic material with permittivity ϵ_{base}, the honeycomb structure shown in Figure 2.7 is fully defined by θ, α, β, ϵ_{base} and w. The unit cell of a conventional honeycomb

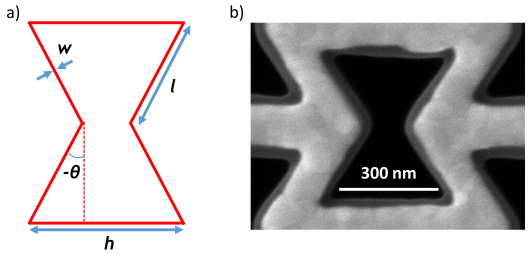

Figure 2.7: ***Honeycomb unit cell.*** *a) The geometry is fully defined by* α=h/l, β=w/l *and* θ. β *describes the relative density of the honeycomb. Adapted from [100] b) SEM image of a fabricated unit cell for comparison.*

is characterized by having equal length facets and equal internal angles, $\alpha = 1$ and $\theta = \pi/6$ radians, respectively. Considering such a planar auxetic honeycomb structure the effective permittivity (ϵ_{eff}) has the form [108],

$$\epsilon_{eff} = \begin{pmatrix} \epsilon_x & 0 & 0 \\ 0 & \epsilon_y & 0 \\ 0 & 0 & \epsilon_z \end{pmatrix}. \tag{2.13}$$

In a conventional non-auxetic honeycomb, α and θ are fixed and the effective permittivity is governed only by β and ϵ_{base}. The effect on a conventional honeycomb of increasing β or ϵ_{base} is to increase simultaneously the diagonal terms of the permittivity tensor. In an auxetic re-entrant honeycomb, α and θ are not fixed which, from a structural design viewpoint, allows tuning to enhance a honeycomb's structural performance and, from the electromagnetic design viewpoint, facilitates a much greater control over the honeycomb's effective permittivity [100].

Tunability of metamaterials and metasurfaces is an important step forward when bringing metadevices to practical application. In re-entrant honeycomb designs such tunability can be envisioned as already discussed in this chapter (section 2.1) and also in Chapter 1 (section 1.3). Changes of the optical properties of a metasurface can be achieved by actuating synchronously thousands of metamolecules. Plasmonic response and thus optical properties of the metasurfaces are highly sensitive to the geometry of their structure. However, stretching or compression of the entire material will normally change its aspect ratio and such directional deformation changes also the degree of optical isotropy. In mechanical metamaterials (auxetics) this problem can be overcome by designing structures with a Poisson's ratio of -1. Upon uniaxial stretching (compression), such structures will expand (shrink) equally in all directions, resulting in conservation of isotropy of the initial design. This means that such auxetic metamaterials which are initially isotropic will keep their isotropy, while anisotropic ones will keep their anisotropy. Moreover, when fabricating such auxetic structures at the nanoscale, optical resonances characteristic of electromagnetic metasurfaces are observable. Micro- and nanoauxetic metamaterials combined with actuation mechanisms of reconfigurable THz and photonic metasurfaces [69, 71, 109, 110] promise a class of tunable optomechanical metadevices with fixed optical anisotropy. In principle, auxetics,

which expand (shrink) in all directions upon stretching (compression), can maintain the aspect ratio of their unit cell, resulting in similar tuning of their optical properties for light polarized parallel or perpendicular to the applied force that causes the unit cell size variation. Careful design of the auxetic scaffold that supports plasmonic or high-index dielectric resonators enables unique combinations of mechanical and optical properties that may be controlled through actuation with sub-microsecond response times [71,72]. Due to strong confinement and coupling of the electromagnetic response of micro- and nanoscale metasurfaces, we argue that small geometry changes in such metasurfaces will lead to significant optical property changes with unchanged optical isotropy. In this work, for the first time at the nanoscale, mechanical and electromagnetic metamaterials are merged in order to unlock such optomechanical properties.

2.4 Coherent Control of Metasurfaces

The ever increasing demand for all-optical data processing has introduced the need for efficient control of light with light. A number of recent studies illustrated that optical phenomena in thin films, from intensity and polarization effects to nonlinear and quantum phenomena, manifest differently in travelling and standing waves [66,111]. Indeed, a deeply subwavelength thin film may be placed at a node or anti-node of a

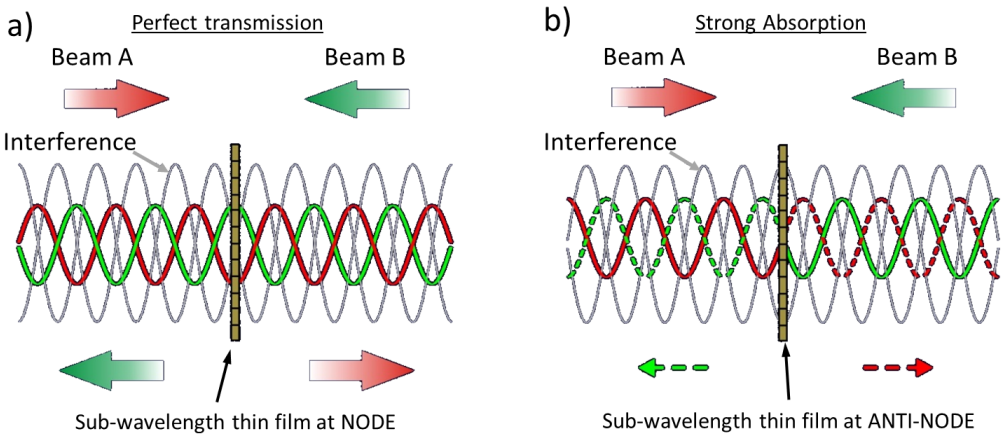

Figure 2.8: ***Coherent control of light with light.*** *a) When a thin film of deeply subwavelength thickness is placed at an electric node of a standing electromagnetic wave, no interaction between film and wave is observed leading to perfect transmission. b) In contrast, when it is placed at an electric anti-node, the interaction between film and wave is enhanced, leading to increased absorption on the film, compared to single beam illumination.*

standing wave formed by counter-propagating coherent beams of light. If the thin film is placed at a node of electric field (Figure 2.8 a)), the optical electric field cannot interact with it and therefore the electric light-matter interaction is switched off; the thin film is effectively transparent. In contrast, the light-matter interaction will be enhanced if the thin film is located at an electric field anti-node of the standing wave, see Figure 2.8 b).

Therefore, absorption can be controlled, from perfect transparency to complete dissipation of electromagnetic energy by the mutual phase and intensity balance of the coherent counter-propagating waves interacting on the absorber. This provides a method to go beyond the theoretical limit of 50% absorption in a thin film [66], but also a new way for controlling optical signals [112]. Usually, the translation of the sample between nodes and anti-nodes of the standing wave is achieved by varying the beam phase difference between the two counter-propagating beams, A and B, while keeping the sample position fixed. Considering two linearly y-polarized counter-propagating plane waves with wave number k and frequency ω, the following electric fields describe both beams,

$$\mathbf{E_A} = E_0 e^{-i(\omega t - kz + \Delta\phi)}\hat{y}, \tag{2.14}$$

$$\mathbf{E_B} = E_0 e^{-i(\omega t + kz)}\hat{y}, \tag{2.15}$$

where, E_0 is the amplitude of the electric field and $\Delta\phi$ is the relative beam phase difference at position $z = 0$. The interference of these two counter-propagating waves produces a standing wave which oscillates in time, but has stationary spatial dependence. The position-dependent energy density stored in this electric field (dU/dV) can be described as,

$$\frac{dU}{dV} = \frac{\epsilon_0}{2}\left|\mathbf{E_A} + \mathbf{E_B}\right|^2, \tag{2.16}$$

from where we can derive the time averaged electric energy density at position $z = 0$ of the standing wave,

$$< \frac{dU}{dV} >_{|z=0} = 2w_e(1 + \cos\Delta\phi), \tag{2.17}$$

where $w_e = \frac{\epsilon_0}{2}E_0^2$ is the electric energy density of the single beam (same for A and B) entering the system. An absorber of deeply subwavelength thickness with incoherent absorption coefficient A_{incoh}, standing at z = 0 will interact with the energy density

given by equation 2.17. Thus, the fraction of overall incident power absorbed by the film in the coherent control scheme is,

$$A_{coh} = A_{incoh}(1 + \cos \Delta\phi). \tag{2.18}$$

Looking into equation 2.18, when the phase shift between counter-propagating beams at the metasurface is $\Delta\phi = (2N + 1)\pi$ where N is an integer, we are at the nodes of the standing wave and the absorption is always zero. When the same phase shift at the metasurface is $\Delta\phi = 2N\pi$ we are at the anti-nodes of the standing wave and absorption will be maximized, $A_{coh} = 2A_{incoh}$. In this way, all-optical control over the light-matter interaction at the metasurface is achieved.

Two coherent beams of light can interact on a layer of absorbing material in such a way that one beam modulates the intensity of the other. The interference of the two beams can eliminate the plasmonic Joule losses of optical energy in the absorber resulting in full transmission of the incident light. Depending on the mutual phase of incident beams it can also lead to total absorption of light. Optimal performance requires 50% absorption of a single illuminating beam with balanced reflection and transmission, in a thin film that is thin compared to the wavelength. Unfortunately, unstructured thin films cannot, simultaneously, be deeply thin compared to the wavelength of light, reach 50% single beam absorption, with balanced 25% reflection and 25% transmission. Metasurfaces, however, can be designed to achieve 50% of absorption while keeping their thickness deeply subwavelength. Moreover transmission and reflection can also be engineered and balanced. Modulation of light with light based on the coherent perfect absorption in metasurfaces of deeply sub-wavelength thickness is possible and it has been demonstrated with a continuous wave (CW) laser [66] and with femtosecond optical pulses exhibiting modulation bandwidths of at least few terahertz [5].

Furthermore, the ability to control the wavefront of light is fundamental to focusing and redistribution of light, enabling many applications from imaging to spectroscopy. Established solutions for dynamic wavefront control are either electro-optical spatial light modulators based on liquid crystals or digital micromirror devices [113–115], or all-optical devices based on holographic operations in nonlinear photorefractive me-

dia [113, 116, 117]. Therefore, wave interaction on highly nonlinear photorefractive materials is essentially the only established technology allowing the dynamic control of the wavefront of a light beam with another beam of light, but it is slow and requires large optical power. However, two-dimensional control of light with light based on the coherent interaction of optical beams on highly absorbing plasmonic metasurfaces can also provide wavefront manipulation and offers advantages including arbitrarily low intensities and high speeds. Finally, far-reaching implications of the coherent control idea can be in all-optical data-processing functions such as all-optical modulation, summation and inversion that can be performed in a 4-port device utilizing a thin absorber [118]. All of these concepts and application ideas need, however, deeply subwavelength thin films which can provide high levels of absorption. Moreover, unstructured thin films cannot provide these properties while structured ones (metasurfaces) can. In order to demonstrate high-contrast modulation of absorption of light with light, metasurfaces need not only the characteristic mentioned before but also identical optical properties for opposite directions of illumination. Using cutting edge nanofabrication processes, adequate metasurfaces for such experiments have been fabricated by me and several examples of coherent control of light with light have been demonstrated by colleagues, see Chapter 6. Combination of symmetric metasurfaces of deeply subwavelength thickness with the coherent control concept allows control over absorption of light with light from almost 0% to almost 100% with 90 THz bandwidth, arbitrarily low intensities down to the single photon quantum limit and diffraction-limited spatial resolution. The next sections describe the nanofabrication and characterization techniques used to obtain and study, not only ultrathin metasurfaces, but also nanomembrane-based reconfigurable metasurfaces.

2.5 Metasurface Nanofabrication

A lot of the progress in optical metasurface research only became possible due to developments in nanofabrication technology achieved over the last two decades. However, in order to keep pushing the boundary further, more improvements and merging of technologies for fabrication of structures with nanometre resolution is imperative. If one can fully control nanometre scale fabrication and even achieve sub-nanometre res-

olution, high quality photonic metasurfaces can be realized and further lower their wavelength of operation. Moreover, sample fabrication and processing becomes increasingly important when concepts must be put forward into devices. If fabrication does not reach a minimum level of quality performance will be degraded or could even vanish completely. The requirements of metasurface samples, depending on the final applications, are becoming increasingly more complex with high levels of accuracy and precision needed. The definition of metasurfaces involves that the size of metamolecules must be substantially smaller than their operating wavelength, which is few hundreds of nanometres for visible light and their thickness is considerably sub-wavelength.

Nanofabrication of optical metamaterials and metasurfaces is extremely challenging and requires the creation of features at deep subwavelength scale. The required feature sizes are smaller than the resolution of conventional photolithography but and therefore advanced technologies are being employed. Nanoimprint, interference optical lithography, direct laser writing, electron beam lithography (EBL) and focused ion beam (FIB) milling are just some examples [119, 120]. Some of these technologies achieve cost efficient, high-volume fabrication of micro- and nanoelectronic devices, but require masks/stamps, chemical solutions or highly energetic (thermal) processes which can be a disadvantage for prototyping. Considering low-volume fabrication of nanodevices like optical metamaterials and metasurfaces for prototype device development, focused ion beam milling, despite being time consuming, stands out as the best choice. This flexible technology allows the fabrication of a large range of structures in a single step process with spot size of 5 nm and line resolution of 30 nm without involving chemical precursors. Not only structuring of materials in order to achieve high resolution metasurfaces is important, but also the way initial materials are obtained before focused ion beam milling and their post-treatment can be crucial.

Also, free-standing plasmonic metasurfaces with deeply subwavelength thickness must be used to achieve metasurfaces for application in coherent control experiments, as mentioned in section 2.4. In order to achieve such ultrathin membranes of plasmonic metal, processes and methods that are not usually used in metamaterials and metasurfaces fabrication shall be brought into play. Free-standing gold membranes will be fabricated for this purpose using etching processes alongside metal evaporation techniques. Here we will introduce the processes used for thin film deposition and etching

as well as focused ion beam milling.

A lot of work has been done recently concerning fabrication at the nanoscale, exploring new techniques, increasing resolution levels and reproducibility. Hopefully this piece of work adds to such advances and brings metadevices closer to reality by introducing new fabrication methods and taking advantage of their versatility. With improved control over nanoscale fabrication and characterization techniques plus the theoretical knowledge already obtained, one can finally think of realizing metadevices for applications.

2.5.1 Resistive Thermal Evaporation

Several techniques can be used in order to obtain metallic plasmonic thin films. Physical or chemical deposition methods can be used depending on the final requirements and thin film composition, morphology or application. For example, chemical processes are usually complex (CVD), require high temperature (Sol-Gel) and precursors contamination is inevitable (Spin Coating). However, such process can deliver a very smooth surfaces and stoichiometry control is an advantage. For metamaterials and metasurfaces, the goal is to achieve metallic thin films with plasmonic properties, usually made out of gold, with no strict requirements in terms of electrical properties or morphology. The crucial parameter to take into account is the film thickness, as explained below.

Resistive thermal evaporation involves two processes: hot source material sublimation and condensation on a substrate. In our case, deposition occurs in high vacuum which allows evaporated particles to travel to the substrate with few collisions with other particles on the way (long mean free path), increasing purity of the final films. A high current is applied to a tungsten crucible containing gold pellets in order to electrothermally heat it up to the melting point of gold. Metal particles start to evaporate and will easily reach the substrate where they will firstly form small islands of material and later coalesce into a continuous film. However, by slightly changing the deposition parameters (i.e. pressure, evaporation rate, temperature) we can manipulate the final properties of the gold films. For example, heating up the substrate can promote the development of the microstructure by grain growth and polycrystalline thin films can be manufactured. While thin film quality is important for metasurfaces, the metal film thickness is crucial as plasmonic properties depend on the photon penetration skin

depth of the metal. The skin depth can be calculated as [121],

$$\delta_s = \frac{1}{\frac{\alpha}{2}}, \tag{2.19}$$

where $\frac{\alpha}{2}$ is the attenuation constant and is identical to the (negative) real part of the propagation constant, the ratio of the amplitude at the source of the wave to the amplitude at some distance x. For a typical plasmonic metal such as gold, the skin depth ranges between 6.2 nm for 2 μm wavelength and 2.8 nm for 400 nm wavelength.

The final gold thin films used here have thicknesses between 30 nm, the lower thickness limit in order to obtain high resolution and high precision focused ion beam milling, and 60 nm, which is still deeply subwavelength compared to the near-infrared wavelengths used in the experiments discussed in Chapters 3 to 6. Moreover, low roughness, high uniformity and nanoscale grain structure are characteristics of the final deposited thin films. Unless otherwise stated, all the plasmonic metallic thin films deposited for this work were obtained using resistive thermal evaporation, at high vacuum (2×10^{-6} mbar) of gold pellets (99.99%) at evaporation rates of 0.10 nm/s. Generally, all of the gold thin films used in this work have a morphology similar to the one shown in Figure 2.9.

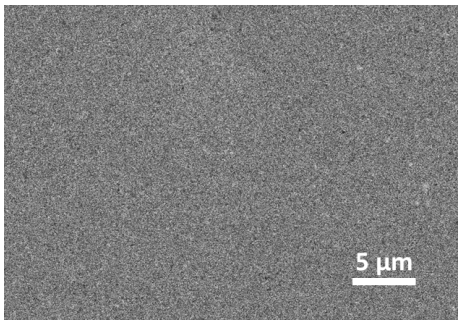

Figure 2.9: ***Typical gold thin film deposited by resistive thermal evaporation.*** *Image obtained by SEM of a typical gold film on a silicon nitride membrane. The gold film thickness is 50 nm and the grain size is a few 10s of nanometres.*

Due to the low melting point of gold is it possible to choose from a wide range of deposition techniques, however, by using resistive thermal evaporation, a cost effective, high output and simple method, thin films of gold with desirable plasmonic properties can be produced. Also, this deposition method allows substrates to be patterned with low resolution by masking some areas to selectively prevent metal deposition. This is

very useful when electrical connections must be fabricated on devices to avoid focused ion beam milling of large areas which is hugely time consuming. Taking advantage of the fact that our plasmonic material is also a good electrical conductor, we simply use a clover mask in order to pattern our substrate, see Figure 2.10. Our mask consists

Figure 2.10: ***Patterned gold film on silicon nitride nanomembrane.*** *Gold film deposited by resistive thermal evaporation through a mask onto a commercially available silicon frame containing a silicon nitride membrane of nanoscale thickness at its centre (wobbly area). Overall size:* 5×5 mm^2

of *Kapton* tape placed from the centre of the substrate to the edges, at the middle of each face. Since resistive thermal evaporation is a highly directional evaporation method, our substrates must be in constant rotation to avoid shadow effects. Using such masking of our substrate, we can later individualize 4 different electrical contacts by only removing the gold layer from the nanostructure to reach the gold-free area, a few hundreds of microns (Figure 2.11).

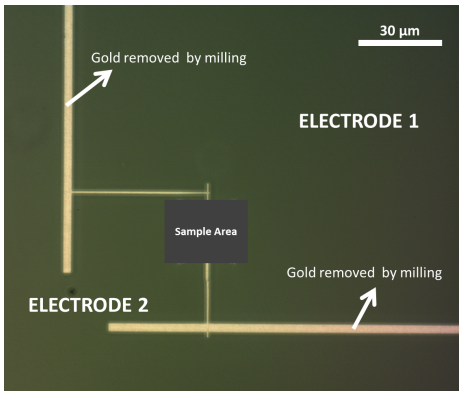

Figure 2.11: ***Fabrication of electric contacts.*** *Optical image showing the sample area in the middle of a gold-coated silicon nitride membrane. In order to individualize each electrode for electrical signal application, milling of the gold layer is performed to reach the gold-free areas obtained by masking our substrate.*

Resistive thermal evaporation combined with coarse masking of the electrodes, is a simple and fast way of preparing substrates for metamaterials and metasurfaces high

accurate and precise fabrication. For reconfigurable metasurfaces, electrical connections are individualize right after the fabrication of the nanostructure. Further details on how to achieve free-standing plasmonic substrates are given in Chapter 6, section 6.2.

2.5.2 Focused Ion Beam Milling

Demand for miniaturization in electronics and optoelectronics increased the number and accuracy of fabrication techniques able to deliver sub-micron features. Several lithographic methods [122, 123], including electron beam lithography [124], were developed in recent years to achieve resolutions below 100 nm. Another technique that recently emerged is nanoimprint [125] which uses a stamp in order to reproducibly pattern a surface. However, both technologies have disadvantages. Considering, for example, any type of photolithography, the need for a photomask is inefficient and restrictive while high-resolution masks have prices well above £10k, making this technique too expensive for prototype fabrication and development. Lithography with multi-step techniques involving chemical procedures that require optimization can damage nanoscale structures, for example due to surface tension in liquids. Nanoimprint promises large area patterning and cheap mass-production of identical copies of the same photonic metasurface, however, the cost of stamp fabrication makes it unsuitable for obtaining research samples, where almost every sample needs to be different.

Focused ion beam (FIB) milling has been successfully used in the field of metasurfaces and photonic metamaterials allowing single nanodevice fabrication for prototype development. Historically, FIB technology was mainly used for sample preparation for transmission electron microscopy (TEM), failure analysis for semiconductors and MEMS, photolithography mask repair and circuit edit procedures [126]. FIB is now a powerful technique for fabrication and preparation of nanoscale samples. Despite being very time consuming, its few nanometre resolution and versatility made it a success. Recently, FIB milling has been widely used for prototype nanofabrication, especially for reconfigurable metamaterials and optical metasurfaces.

The basic functions of the FIB require a highly focused beam. The smaller the effective source size, the more tightly can the ion current be focused to a point. Unlike the broad ion beams generated from plasma sources, high-resolution ion beams are defined by the use of a field ionization source with a small effective source size on

the order of 5 nm, therefore enabling the beam to be tightly focused. Of the existing ion source types, the liquid metal ion source (LMIS) provides the brightest and most highly focused beam. There are a number of different types of LMIS sources, the most widely used being a Gallium-based (Ga) blunt needle source. Ga has clear advantages over other LMIS metals such as In, Bi, Sn, and Au because of its combination of low melting temperature (30°C), low volatility, and low vapour pressure. The low melting temperature makes the source easy to design and operate. Because Ga does not react with the material defining the needle - typically tungsten (W) - and evaporation is negligible, Ga-based LMISs are typically used in commercial FIB systems [126, 127]. The most important components of such commercial system are: the ion column, the work chamber, the vacuum system, the gas injection system and the computer controlled user interface [128]. A typical diagram of a FIB column is shown in Figure 2.12.

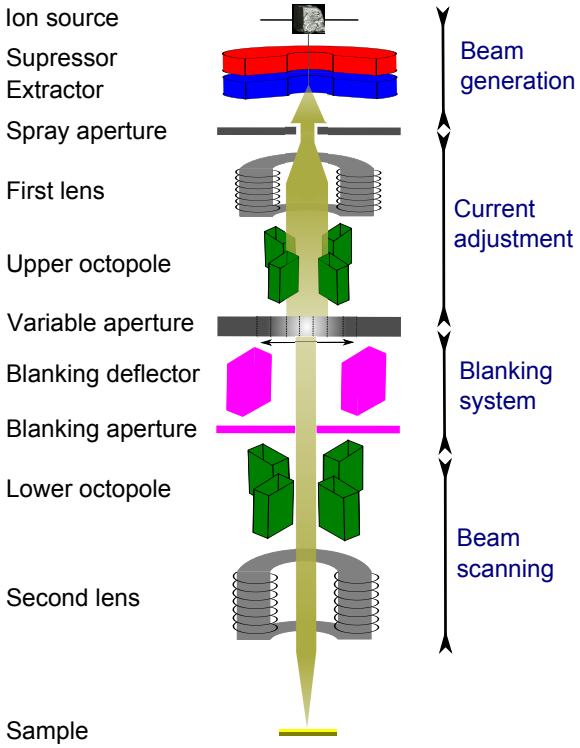

Figure 2.12: ***Schematic of the focused ion beam system*** *composed of 4 subsections: beam generation, current focusing adjustment, beam blanking system and beam scanning. Adapted from [128]*

The structure of the column is similar to that of a scanning electron microscope (SEM) but instead of an electron beam it uses a gallium ion (Ga^+) beam. Typically, a vacuum of about 1×10^{-7} mbar is maintained inside the column to enable emission,

focusing and manipulation of the ions. At the source, liquid Ga is extracted from a liquid source by electric field induction upon high voltage application. Ions of Ga will then be accelerated down the column and pass through a first aperture for first profile shaping. The ion beam energy is typically between 2 and 30 keV. Then, the ion beam is condensed by the first electrostatic lens while the upper octopole adjusts the beam stigmatism. Using the variable aperture mechanism, the beam current can be varied, usually between 1 pA and 22 nA. Depending on the beam current one can obtain either a fine beam for high-resolution imaging or a strong beam for fast and rough milling. Blanking of the beam is realized by the blanking deflector and aperture in order to promptly blank the beam during fabrication. The lower octopole is used for raster scanning the beam over the sample in a user-defined pattern, facilitating the most intricate and twisted designs with high resolution. Finally, the beam is focused to a fine spot with the second electrostatic lens, enabling a best resolution in the sub 5 nm range.

In order to actually observe what is happening inside the vacuum chamber, detectors surrounding the sample record interactions between the sample and incoming ions, detecting scattered ions and electrons to reconstruct an image. The Everhart-Thornley detector (ETD) [129] and continuous dynode electron multiplier (CDEM) [130] are used to collect secondary electrons and ions for imaging. In FIB technology, imaging and milling with Ga^+ ions will always result in Ga^+ ion implantation in the sample. In order to avoid ion implantation during sample imaging, most modern FIB instruments supplement the FIB column with an additional SEM column so that the instrument becomes a versatile "dual-beam" platform. The ion beam and electron beam are placed in fixed positions and share their focal points at the"coincidence point", an optimized position for the majority of operations, including FIB sample direct writing [127]. The SEM part can be used not only to search and image the sample area for FIB processing but also to monitor the process of FIB milling in real time.

The physical solid-ion interactions occurring in the FIB milling process are well known. When an ion hits a solid, it loses kinetic energy through interactions with the sample atoms. The ion typically comes to rest in the solid, leading to its implantation. The transfer of energy from the ion to the solid results in a number of different processes (see Figure 2.13): ion reflection and back-scattering, electron emission, elec-

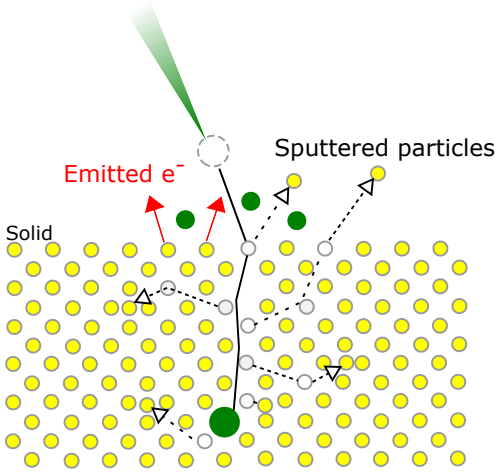

Figure 2.13: ***Focused ion beam interactions*** *showing ion reflection and backscattering (small solid green circles), electron emission (red arrows), atomic sputtering (ejected solid yellow circles) and sample damage (displaced solid yellow circles). Atomic vacancies are represented by the solid white circles. After interaction with the solid, the incoming ions will come to a rest inside the solid (big solid green circle). Adapted from [127]*

tromagnetic radiation, atomic sputtering and ion emission, sample damage, and sample heating [126]. With the exception of electromagnetic radiation generation, all of these processes are important to FIB applications. Ion kinetic energy and momentum are transferred to the solid (sample) through both inelastic and elastic collisions. In inelastic interactions, ion energy is lost to the electrons in the sample resulting in ionization of material atoms and emission of electrons and electromagnetic radiation from the sample. In elastic interactions, ion energy is transferred as translational energy to target atoms and can result in damage and sputtering from the sample surface. The most accepted model to explain interactions occurring between a solid and a FIB is the collision cascade model [127, 131, 132]. The collision cascade involves a series of independent multiple collisions when 5-30 keV Ga^+ ions impinge on most solids. If the translational energy transferred to a target atom during a collision exceeds a critical value called the displacement energy, the atom will be knocked out of its original site. This primary recoil atom may have sufficient energy to displace further sample atoms (secondary recoils), thus generating a volume where large numbers of atoms have excess kinetic energy. If a displacement collision occurs near the surface, the recoil atom may be emitted from the solid and lead to sputtering. The displacement energy (typically on the order of 20 eV) is much larger than the binding energy for the atoms (of the order of 1 eV), reflecting the fact that the collisions are nonadiabatic, because of the

very short time scale. After approximately 10 ps, the 5-30 keV Ga^+ ion comes to rest in the solid, and the energies of all particles participating in the cascade have decreased below the displacement energy. At this point, the collision cascade has ended. However, other interactions can continue and evolve, such as emitted particles and radiation, ion beam damage (lattice defects), integrated Ga and heat [126]. Based on the ion-solid

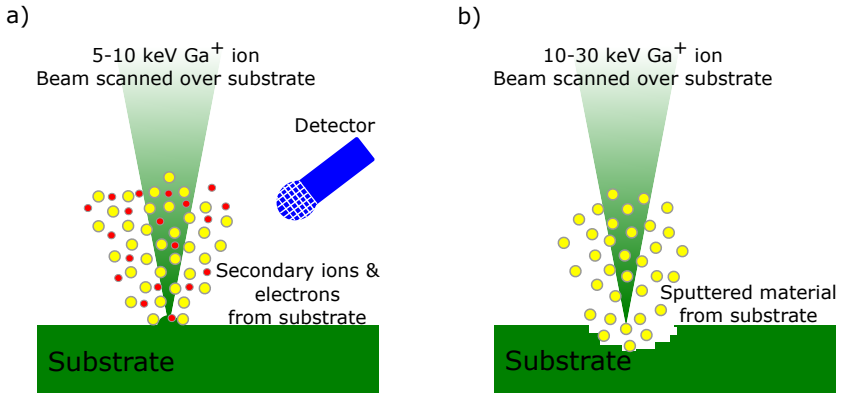

Figure 2.14: ***Focused ion beam operation modes.*** *FIB systems can be operated in distinct modes including a) imaging and b) milling. Adapted from [128]*

interactions, there are three main working principles of an FIB system, namely imaging, milling, and ion beam induced deposition [128]. Figure 2.14 shows the first two modes mentioned, since they are the relevant ones for this work. Controlling, for example, emission energies (5-10 keV), FIB system can be used for high resolution imaging of samples (Figure 2.14 a)). Such process is destructive and should be carefully controlled to minimize alteration of sample properties. In a scanning electron microscope (SEM), the imaging signals can be generated from a number of electron induced processes including low energy secondary electrons, back-scattered high energy electrons, cathode luminescence, x-rays, and Auger electrons, all of which carry information about target topography or chemical composition. In the case of ion beams, the signals detected are low energy secondary electrons and/or secondary ions. The secondary electron yield per incident ion is an important physical parameter in FIB applications. Generally, the secondary electron emission by ion bombardment is much more sensitive to details of the surface structure of the target than in the SEM because the projection range of ions in the keV energy range is short. Many electrons are produced in collision processes between ions and target atoms, and because of momentum conservation, the electrons excited by the ions have rather low energies. The region of interaction is

quite shallow and so the number of secondary electrons escaping from the surface of the target will grow with increasing angle between the target normal and the incident ion trajectory. Since the low energy electrons produced deep below the surface cannot escape, FIB is especially sensitive to the surface topography. Low energy electrons will also be sensitive to the work function of the surface [133]. The FIB secondary electron signal will thus depend on the chemical nature of the surface as well as its morphology. This chemical effect will vary with target material, in particular there is invariably a secondary electron yield difference between oxides and clean elemental surfaces. The secondary electron yields for oxides are always higher than for metals [134, 135] as more low energy electrons will be able to surmount the surface barrier. Another feature differentiating FIB from SEM is the greater sensitivity of an incoming beam to the crystalline structure of the sample. In a crystalline sample it is possible for the primary ions to channel if the orientation of the crystal is aligned with the beam. In this case, the ions travel between the columns of atoms and their range can be quite large. Since a longer range implies fewer interactions (per unit length) between ion and sample, the number of secondary electrons produced will be lower if the crystalline sample is oriented in certain directions relative to the beam. This effect induces image contrast variations depending on small changes of the angular orientation of the sample, which is called "channelling contrast". It is important to remember that ion beam imaging always results in some ion implantation and sputtering of the sample surface.

Another operation mode that is widely used in this work is the milling process. In such mode, higher energies for the ion beam are used (10-30 keV) to promote sputtering of sample's material and allow milling (Figure 2.14 b)). Ion milling is a method of material removal by means of physical sputtering phenomena. The sputtering process involves the transfer of momentum to surface and near-surface atoms from the incident ions through a series of collisions within the solid target. If the ion beam impinges on the target vertically there must be enough momentum reflected from the solid to eject one or more surface atoms. Therefore, the sputtering rate, which is defined as the ratio of the number of ejected atoms to the number of impinged ions, is a function of the angle of incidence of the ion beam as well as the mass and energy of the ions, the mass of the target atoms and the nature of the target atomic structure. FIB milling is carried out with repetitive scanning over a designated area. Arbitrary surface topologies

can be created by controlling the scanning pattern, scanning location, and ion dosage. Typically, with a focused 30 keV Ga^+ ion beam of less than 5 nm diameter, structures with less than 30 nm features can be realized. The minimal milling linewidth is about 50 nm. The FIB milling process can be further enhanced by introducing a specific gas (such as XeF_2) into the work chamber. It will increase the etching rate and the selectivity towards different materials by chemically facilitating the removal of reaction products. This technique is called gas-assisted etching.

In order to attain high resolution nanostructures, substrates need to possess a minimum mechanical and thermal stability for FIB milling. Being an high energetic process, plasmonic thin films should attain minimal mechanical resistance and provide good enough thermal energy dissipation. A few tens of nanometres thick plasmonic layer on top of a 50 nm silicon nitride membrane has proven to be enough for the fabrication of nanomembrane-based high quality metamaterials and metasurfaces. However, when fabricating free-standing plasmonic metasurfaces, composed only from a very thin metal layer, a minimal thickness of about 50 nm is needed to achieve same quality nanostructures. Thinner plasmonic layers will deform (lack of mechanical stability combined with low thermal energy dissipation) upon FIB interaction and structuring becomes problematic.

Since having been introduced to the field of metamaterials and metasurfaces, FIB milling of nanomembranes for reconfigurable metasurfaces is proliferating. A huge range of designs and architectures can be envisioned through the usage of such versatile and powerful technology achieving the resolution needed to target optical wavelengths. The advantages of high resolution, diversity of shapes and dimensions that can be obtained and the wide range of materials that can be milled outweigh the disadvantages of slow nanofabrication and high cost. FIB milling has already contributed hugely to advances in metamaterials and it is turning into a crucial technology for targeting smaller and smaller wavelengths.

2.5.3 Reactive Ion Etching

In solid state physics it is not only important to control how materials are obtained and structured but also how to remove or partially modify them. Therefore several etching processes are used in order to selectively interact with different materials, depending

on crystallographic orientations, chemical reactivity or affinity. There are two main groups when referring to etching technologies, dry and wet etching.

Wet etching involves chemical reactions in a liquid based form in order to process the materials and devices. Such etching mechanism can provide high etching rates and directionality, but they can also lead to contamination of the materials and damage to nanostructures due to surface tension in solid-liquid interaction.

Dry etching mechanisms usually consist of sputtering materials with non-reactive gasses using high mass and energy in order to selectively remove material from a substrate. Selectivity is usually obtained through sacrificial layer deposition, masking or photoresist patterning. All etching systems have their preferred application material or architecture, however, in same cases crucial requirements have to be met.

In our case, since our substrates are silicon nitride nanomembranes, chemical and solution based etching is likely to rip off the fragile membrane. Reactive Ion Etching (RIE) is a resourceful technique for easily removing one material without affecting the subsequent or neighbouring one. RIE is a dry etching technique that consists on a mixture of physical and chemical processes occurring in an ion plasma environment. Using chemically reactive plasma, high-energy ions from the plasma interact with the material to be etched, chemically reacting with it and finally removing the targeted material. The ion plasma is generated in vacuum by an electromagnetic field, see Figure 2.15.

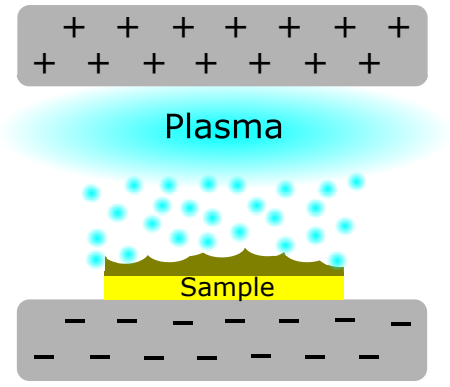

Figure 2.15: ***Reactive ion etching.*** *Gases introduced inside the vacuum chamber will be ionized upon voltage discharge. Ions will then physically and more prominently chemically react with the sample, etching the target material away.*

A typical (parallel plate) RIE system consists of a cylindrical vacuum chamber, with a substrate holder situated in the bottom portion of the chamber. Gas enters

through small inlets in the top of the chamber and exits to the vacuum pump system through the bottom. Depending on the material to be etched and its thickness, ion type, quantity and energy shall be carefully controlled. Gas pressure is typically maintained in a range between 10^{-3} mbar and 10^{-1} mbar by adjusting gas flow rates and/or adjusting an exhaust valve. Plasma is initiated in the system by applying a strong RF (radio frequency) electromagnetic field to the substrate holder. The field is typically set to a frequency of 13.56 MHz and applied at a few hundred watts. Because of the large voltage difference, the positive ions tend to drift toward the substrate, where they collide with the samples to be etched. The ions react chemically with the materials on the surface of the samples, but can also knock off (sputter) some material by transferring some of their kinetic energy. In our process, for example, we use CHF_3 and Ar as precursor gases, with fluxes of 2 sccm and 10 sccm respectively (sccm = standard cubic centimetres per minute) and RF power of about 80 W. This parameter choice was based on the fact that these gases will not affect gold while the etching rates achieved enable a process that removes a 50-nm-thick silicon nitride layer in approximately 10 minutes. Moreover, by avoiding high RF powers, physical bombardment and consequent sputtering is reduced, increasing the selectivity of our process and avoiding damage of the gold layer in our structures. Due to the mostly vertical delivery of reactive ions, reactive-ion etching can produce very anisotropic etch profiles, which contrast with the typically isotropic profiles of wet chemical etching. In this work, RIE process will be applied to remove silicon nitride membranes used as substrate to deposit thin gold films. This allows the realisation of free-standing gold membranes for fabrication of metasurfaces of deeply sub-wavelength thickness (typically 50 nm), enabling coherent control experiments.

2.6 Metasurface Characterization

Fabrication techniques are very important for the success of this work, however, also prototype sample characterization requires high accuracy as effects in nanostructures are often small in magnitude and difficult to detect. The main objective of this work is to provide dynamic control of light with reconfigurable metasurfaces as well as coherent control of light-matter interactions on metasurfaces. Reconfigurable metasurfaces

actuated using electric currents and magnetic fields, as well as, free-standing plasmonic metasurfaces need a reliable and repeatable way of probing their optical properties with and without external stimulus application. All metamaterials and metasurfaces fabricated during this work rely on very thin silicon nitride nanomembranes (later etched away for the free-standing plasmonic membrane case) supported by a silicon frame. Typically the entire device has dimensions of 5×5 mm^2, with sample thicknesses between 50 and 100 nm, making the manipulation, actuation and electromagnetic characterization very delicate. In order to provide robustness to our reconfigurable devices, we place them on an electrical stage and we 3D printed a magnet holder in order to study their optical response to both electric and magnetic control signals in a reproducible manner, see Figure 2.16.

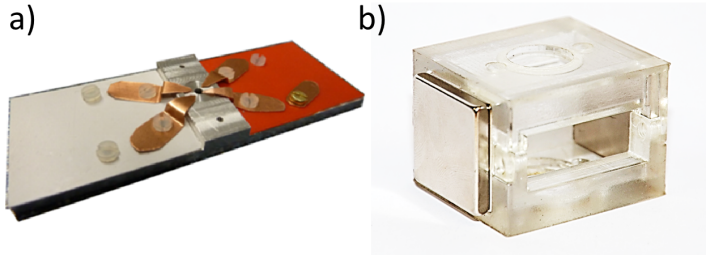

Figure 2.16: ***Holders used for addressing and reconfiguring metasurfaces*** *with a) electric currents and b) magnetic fields. In order to use Lorentz force actuation, sample holder a) can be inserted in the 3D printed magnet holder b) and both external stimuli can be used simultaneously, resulting in a Lorentz force perpendicular to the sample plane.*

After FIB milling of our reconfigurable metasurfaces and correct individualization of electric contacts (section 2.5.1, Figure 2.11), the silicon frame containing our device is placed on the electric holder shown in Figure 2.16 a). Through the copper pads, electric signals can be applied to the nanostructure and since an optical path perpendicular to the sample is available, optical characterization can be preformed. This allows the influence of electric current on reconfigurable metasurfaces to be probed without moving the sample. Moreover, by placing the combined structure (device + electric holder) inside the magnetic holder (Figure 2.16 b)), milli-Tesla magnetic fields can simultaneously be applied to the metasurface. For the free-standing plasmonic metasurfaces fabricated, a simple 3D printed holder was fabricated to facilitate transport and manipulation of samples. Since one of the most important features of such metasurfaces is the symmetry of optical properties with respect to reversal of the light propagation

direction, the latter holder was designed to allow the sample to be flipped over, Figure 2.17.

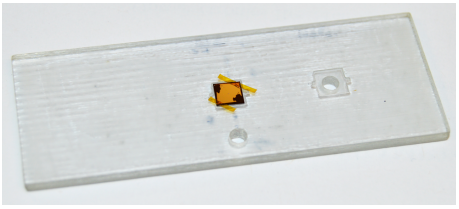

Figure 2.17: ***Holder used for free-standing plasmonic metasurface characterization.*** *In order easily measure optical properties for both sides of light incidence, the holder was designed in a way that the sample does not need to be moved. By simply flipping the entire holder over the backside of the sample can be accessed.*

The optical properties of both reconfigurable metasurfaces and free-standing plasmonic metasurfaces can be measured by placing these assemblies (holders+sample) inside a microspectrophotometer. Moreover, the dependence of a metasurface's optical properties on electric and magnetic signals can also be measured for the reconfigurable metasurfaces. Firstly, reference spectra are taken without any external stimulus applied. Thereafter, optical properties are measured under electric current sweeps and different magnetic field strengths. Through the application of either one or both of these external stimuli, not only reconfiguration of metasurfaces can be demonstrated but also the physical origin of this reconfiguration can be studied.

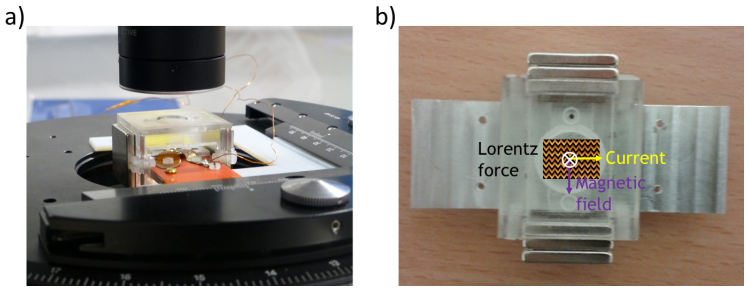

Figure 2.18: ***Metasurface sample placed in the sample and magnet holders*** *shown in Figure 2.16 a) for electrothermal and magnetic modulation measurements using a CRAIC microspectrophotometer. b) Schematic showing the directions of the applied current, magnetic field and resultant Lorentz Force.*

Figure 2.18, shows a metasurface sample being measured with a microspectrophotometer while electric and magnetic stimuli are applied. A microspectrophotometer consists of a spectrometer integrated in a microscope and our model uses mirror-based

reflective optics to allow broadband operation from the ultraviolet to the near-infrared parts of the spectrum (200-2100 nm wavelength). This integration allows for spectroscopy of microscopic sample areas and measurement of optical properties of our metamaterials and metasurfaces. Small sample areas (hundreds of square microns) can be probed non-destructively by collecting light that is transmitted through the sample or reflected from it, see Figure 2.19.

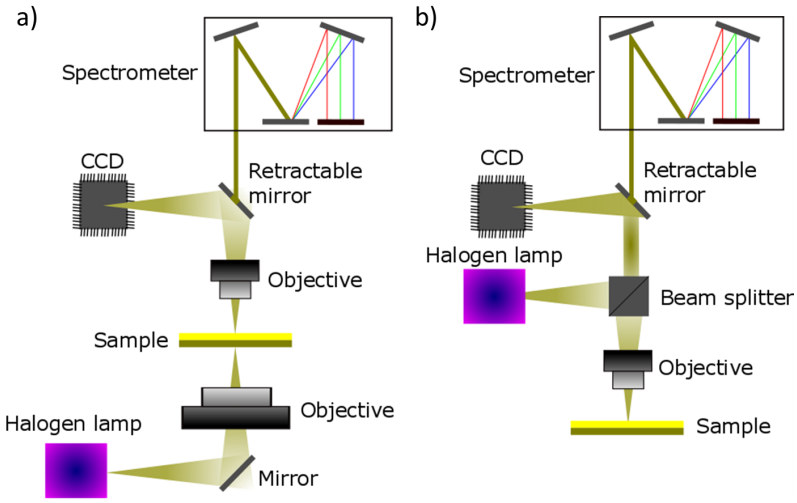

Figure 2.19: ***Microspectrophotometer.*** *The microspectrophotometer system used in our experiments can be operated in two modes: a) Transmission and b) Reflection.*

Light collected from the sample, enters the spectrometer through an aperture (Figure 2.19) and is separated into its component wavelengths. The UV-visible-NIR microspectrophotometer uses difraction gratings to separate white light into its spectral components. The separated light is then focused onto two CCD arrays, one Si (200-950 nm) and one InGaAs (850-2300 nm), where the intensity of each wavelength is measured. The result will be the transmission and reflection spectra of the sample. The portion of light that is not reflected or transmitted might be absorbed or scattered. In subwavelength structures, such as the metamaterials and metasurfaces studied here, scattering is negligible and all light is either transmitted, reflected or absorbed. Using adequate holders and applying the correct stimuli modulation of optical properties can be demonstrated for reconfigurable metasurfaces actuated by electric and magnetic fields. Also, the optical characteristics of free-standing plasmonic metasurfaces for coherent control experiments can be measured using the same microspectrophotometer. For such samples, transmission and reflection spectra are measured for illumination of

both sides of the nanostructure. Moreover, absorption of non-diffracting structures can be calculated from transmission and reflection measurements. In all cases, polarisers are used to measure optical properties for both linear polarizations of incident light.

However, such measurements can only measure spectra in the static (DC) regime. For reconfigurable metasurfaces it would be of interest to study also their frequency dependent light modulation properties. In order to do so, we perform light modulation experiments at a selected wavelength using lock-in amplification, as shown in Figure 2.20.

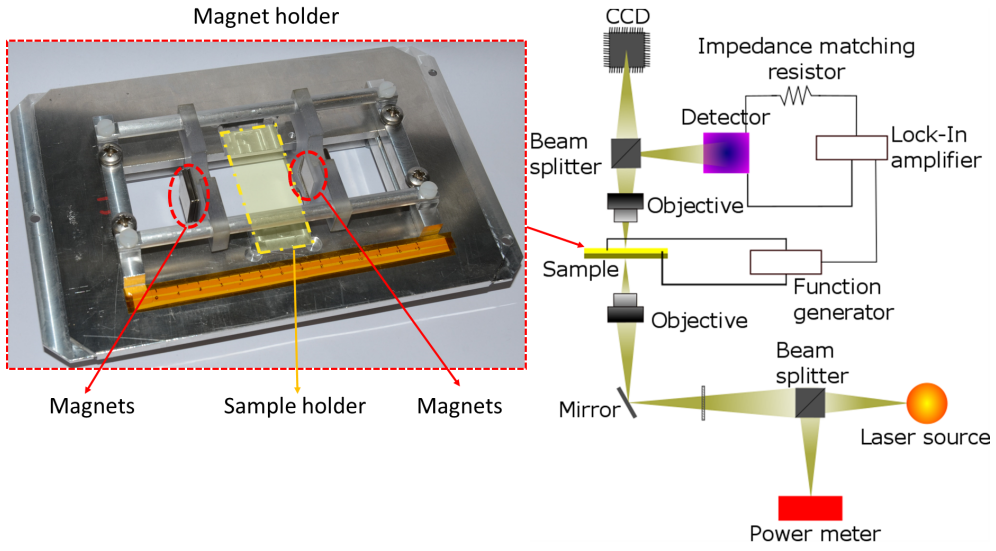

Figure 2.20: ***Setup for magneto-electro-optic modulation experiments.*** *Setup used for frequency dependent modulation of reconfigurable photonic metasurfaces. A 1550 nm laser diode illuminates the metasurface through an optical setup and microscope. Light interacts with the metasurface device which is being modulated with electrical currents applied to the nanostructure using a signal generator at modulation frequencies up to 1 MHz. Lock-in detection at the modulation frequency is used to measure modulation of the laser beam after interaction with the metasurface. The sample holder shown in Figure 2.16 a) is used together with the magnet holder shown by the inset.*

As the measurement system is different, also the holder used for this experiment had to be adapted. Using the same holder of Figure 2.16 a), we place it on the AC modulation setup holder shown in Figure 2.20. In this way, accurate measurements for different magnetic field strengths can be obtained consecutively. Also, the latter holder is designed in such a way that it can be flipped over to facilitate reciprocity measurements preformed while studying the magneto-electro-optical effect that will be demonstrated in Chapter 4. The setup shown consists of a laser source (1550 nm

wavelength) that illuminates the metasurface which is being modulated externally using a signal generator. A sinusoidally modulated current is applied to the metasurface and modulation of the transmitted laser beam is detected using a InGaAs photodetector (New Focus 1811) and two lock-in amplifiers (Stanford Research SR830 up to 100 kHz and SR844 >100 kHz). Using the modulation signal as reference, one can measure the light modulation achieved by our reconfigurable metasurface upon application of electrical currents and magnetic field and study the associated novel electromagnetic effects. The techniques discussed above were utilized for more than one experimental chapter. Other techniques will be discussed in the experimental chapter where they are relevant. The following chapters describe and discuss the main experimental results of this thesis.

Chapter 3

Electrically and Magnetically Reconfigurable Metasurfaces

Reconfigurable metasurfaces based on nano-thickness membranes and plasmonic metals have already shown a huge potential for light manipulation and engineered optical properties, as discussed in Chapter 2, section 2.1. However, despite impressive optical contrasts for reflected and transmitted waves or, for example, several kHz of modulation frequency, none of the previous reports can be considered a practical solution for metasurfaces tuning of optical properties. The thermal reconfigurable photonic metasurface needs cryogenic temperatures [70] while reversible modulation in the electrostatic and optical forces cases can only achieve optical changes of few percent [71, 72]. Therefore, there is still room for improvement by exploring simpler solutions to address such nanostructures which can provide tuning in a practical way and without permanent switching. Achieving reversible and efficient ways of reconfiguring nanomembrane-based photonic metasurfaces at room temperature can bring reconfigurable metasurfaces closer to applications. Advantages of such technology include miniaturization, microWatt power consumption and high achievable frequencies of operation [71, 72].

Considering the physics associated with photonic metasurfaces, small displacements and distance changes between metamolecules can achieve increased tunability due to strong electromagnetic coupling within the structure. Changes of the spacing between metamolecules or their relative position results in a substantial variation on the electromagnetic near-field as well as transmitted and reflected waves. Therefore, actuation of

such structures leads to tuning of their optical properties. Moreover, in contrast to the macroscale where electromagnetic forces are very weak compared to elastic ones, the balance of forces at the nanoscale allows actuation and tuning. In fact, considering the small masses involved at the nanoscale, when approaching distances close to 1 μm the electromagnetic forces, such as electrostatic or Lorentz force become strong enough to displace nanostructures against their elastic force and gravity. Reconfigurable photonic metasurfaces enable tuning of electromagnetic waves at will by moving or actuating unit cells individually or in groups. Here, we will introduce some of the fundamental concepts in such technology and demonstrate a practical and simple solution for reconfiguring photonic metasurfaces to change their optical properties. Such devices can be implemented as filters, switches or magneto-electro-optical modulators.

3.1 Coupled Nearfield Interactions in Metasurfaces

In this work, dynamic control over metasurface optical properties is envisioned by displacing groups of unit cells within a photonic metasurface. In order to better understand and optimize the design to be used, the electromagnetic response of three different designs was simulated using a general purpose software for modelling and simulating physics-based problems (COMSOL). Starting from the concept of planar metamaterials built from bilayer structured nano-thickness membranes, geometric models are designed with the mentioned software. Secondly, 3 different designs were chosen based on literature, considering the existence of sharp edges known to result in strong field concentration and enhancement, and suitability of fabrication and actuation. All structures use the proven gold-on-silicon-nitride bridge actuator design concept used in earlier reconfigurable metasurfaces [70–72]. In fact, all designs are the result of a simple cut through both layers of a gold-coated silicon nitride membrane resulting in 3 different shapes of the gap between elastic bridges: meander cut, inverse triangle cut and chevron cut. In all cases, the considered model consists of a unit cell size of 1.2 μm by 600 nm, composed of 2 bridges in such a way that displacement can also be simulated with minor changes, see Figure 3.1. Overall thickness of our metamolecules is 100 nm (50 nm SiN_x and 50 nm Au), periodic conditions are used and each material is simulated based on its wavelength dependent complex refractive index. The electro-

magnetic input wave is polarized (E_x) perpendicular to the bridge orientation and its electric field amplitude is 1 V/m.

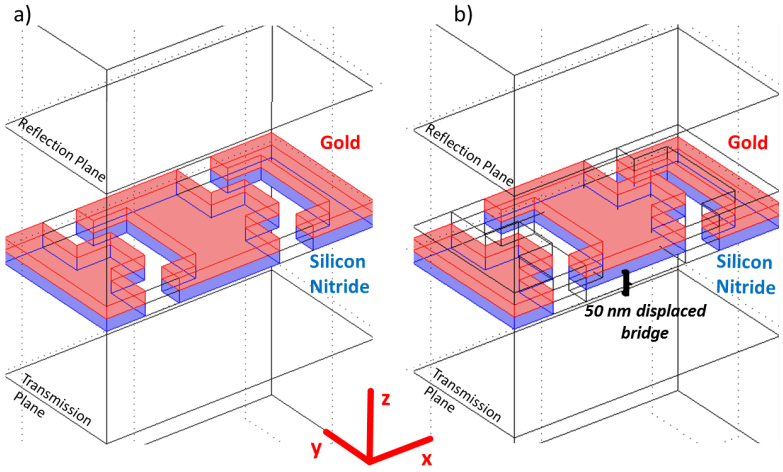

Figure 3.1: ***Metasurface design model.*** *Models used for simulating optical properties of reconfigurable metasurfaces without (a) and with (b) displacement of the central bridge. The unit cell size is 1.2 µm × 600 nm, silicon nitride (blue layer) and gold (red layer) thicknesses are 50 nm for each and the central bridge displacement is 50 nm, for all 3 designs (meander cut shown). Wavelength dependent transmission is simulated using the electromagnetic waves module (COMSOL).*

Moreover, by simply changing the material properties assigned to different domains of the geometry, the optical properties of the displaced structure can be simulated (Figure 3.1 b)) and compared to the stationary case (Figure 3.1 a)). Notice that the simulated displacement is perpendicular to the metasurface plane, avoiding any risk of permanent switching of our structure upon external stimulus application. The change of material properties in our geometry emulates a displacement of the central bridge relative to the outside ones by 50 nm. By integrating the overall power outflow over the transmission plane for each wavelength and normalizing it to the incident wave's power, one can plot the transmission spectra for each studied design, with and without displacement. Bigger differences in transmission of the nanostructure between these two cases will, in principle, lead to increased tunability of our photonic metasurface for the same external stimulus. The wavelength-dependent transmission (600-1800 nm wavelength) for all three designs with and without displacement was calculated considering light polarized perpendicular to the orientation of the bridges, see Figure 3.2.

As can be seen from the spectra, similar properties are obtained for wavelengths

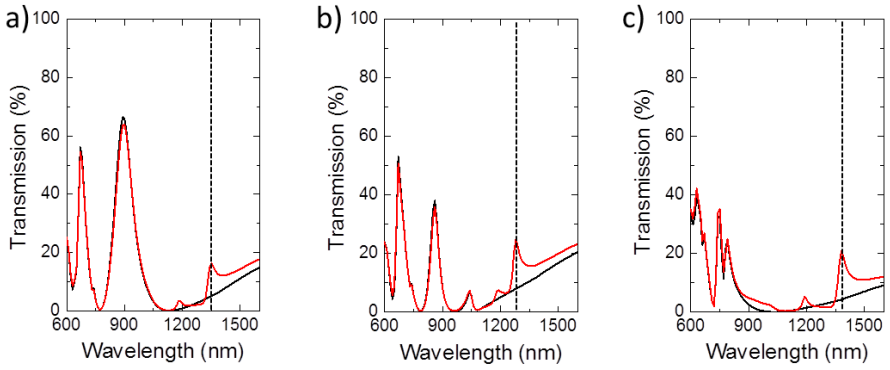

Figure 3.2: ***Transmission spectra for different metasurface designs.*** *Wavelength dependent transmission for all 3 designs: a) Meander cut design, b) inverse triangle cut and c) chevron cut. Simulation results are obtained with (red line) and without (black line) displacement for the 3 different designs. In all cases, incident light is x-polarized (1V/m) and bridges consist of layers of 50 nm SiN_x and 50 nm Au. Dashed lines show the wavelength at which a new resonance appears upon a 50 nm out-of-plane displacement of every second bridge.*

smaller than the unit cell dimension (1.2 μm) in the light polarization direction, comparing the displaced and non-displaced cases for each design. At 1.2 μm all structures show an extra bump for the displaced trace which sits exactly where the wavelength reaches the unit cell size. Moreover, each of the designs present an extra small resonance at longer wavelengths when the structure is only 50 nm displaced. From Figure 3.2 we can obtain the wavelengths where these resonances appear, these being 1.35 μm for the meander cut, 1.28 μm for the inverse triangle cut and 1.38 μm for the chevron cut. At the latter resonances our designs are effectively metamaterials that behave as effective media as these wavelengths are bigger than the unit cell. Differences between displaced and non-displaced spectra for wavelengths smaller than the unit cell may indicate a change in the diffraction pattern of our structures.

It is interesting to study the resonances that appear as a result of displacement in the metamaterial regime. Intensity and phase maps of the electric near-field along propagation direction (E_z) are extracted, 10 nm above the gold surface on every bridge, see Figure 3.3. Such maps indicate the oscillating charge distribution of the plasmonic mode excited by the incident wave. The magnitude of the electric near-field, abs(E_z), is shown in the top row of Figure 3.3. All results are plotted on the same scale and were obtained for the characteristic resonant wavelengths of each structure. Without displacement, all 3 designs are non-resonant and therefore their excitation is weak.

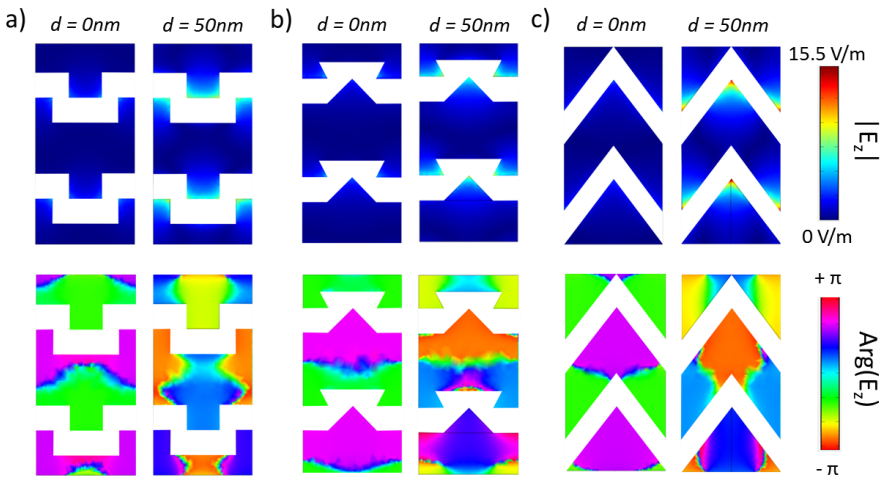

Figure 3.3: ***Near-field maps for different metasurface designs.*** *Electric near-field magnitude and phase maps for the 3 different studied designs. a) Meander cut at 1.35 μm wavelength, b) inverse triangle cut at 1.28 μm and c) chevron cut at 1.38 μm. In all cases the results plotted are abs(E_z) in the top row and arg(E_z) on the bottom one.*

However, when every second bridge is moved 50 nm towards the light source, resonant behaviour at designs' specific wavelength is clear. Considering the 3 studied designs the strongest enhancement of the electric field is observed for the chevron cut with an increase in the magnitude of E_z of about 15 times. Such enhancement is clearly concentrated at the edges of the structure, as expected, and is several times higher when compared to meander and inverse triangle designs. Looking into the phase maps, bottom row of Figure 3.3, without displacement, charges on neighbouring bridges oscillate in phase. Such result is considerably altered upon displacement of every second bridge. For all models, displacement results in resonant and approximately anti-symmetric charge oscillations on neighbouring bridges. This indicates a breaking in the symmetry of the structure and corresponds to the excitation of a resonant "trapped-mode" [136].

While these simulation results provide us with useful insights regarding near-field interactions of neighbouring bridges for the different designs, also mechanical considerations about the design should be taken into account. In principle, the stronger the coupling, the easier it should be to observe displacement-induced transmission changes of our metasurface. However, if the design is too stiff, available forces for tuning might not be strong enough to achieve significant bridge displacement against the structure's elastic forces. Therefore, not only electromagnetic properties of structures but also mechanical ones are important to achieve significant tuning of optical properties. Next

section of this thesis will discuss the mechanical properties of our designs, as well as, estimate the available forces using two main actuation mechanisms. In the end, by changing the physical arrangement of the nanoscale metamolecules we change their coupling and therefore the optical properties of the metasurface array. Large modulation of optical properties will be provided by a design with strongly interacting bridges that have a weak elastic restoring force.

3.2 Classic Beam Theory

After studying the electromagnetic properties of several designs, we estimate the elastic restoring force upon deformation of bridge structures. Gravity can be neglected for the bridge structures of picogram-scale weight and bridge lengths of tens of microns. In order to estimate and understand the mechanical response of our structure, beam theory and forces used for actuation need to be studied.

First of all, we will start with some generic considerations regarding mechanical deformation of the dielectric membrane (Young's modulus, E_{SiN_x} = 297 GPa [137]) used as substrate, ignoring the weaker forces associated with the additional gold layer (E_{Au} = 79 GPa [138]). These considerations will allow us to estimate the restoring force present in such configuration and therefore the magnitude of forces needed to counteract it. Since we will use a design consisting of parallel bridges, let us consider each bridge as a beam fixed at both ends. In this case, the Euler-Bernoulli beam equation [139] can be considered as a good approximation to estimate the restoring force present in response to displacement of the beam,

$$F_{beam}(x) = E_{SiN_x} M_I \frac{d^4u}{dx^4}. \tag{3.1}$$

Here u is the deflection and $F_{beam}(x)$ is a load per unit length. E_{SiN_x} is the silicon nitride elastic modulus and M_I is the area moment of inertia, the product of these giving the stiffness of the beam. The moment of area [140] for a rectangular cross section beam and the spring constant k for a beam fixed at both ends [139], are given by the following equations, where x is displacement at the centre of the beam, w the

width, L the length and t the thickness of a beam:

$$M_I = \frac{wt^3}{12}, \tag{3.2}$$

$$k = \frac{F_{beam}}{x} = \frac{384 E_{SiN_x} M_I}{L^3}. \tag{3.3}$$

From this, the beam's restoring force in response to displacement can be estimated. However, beam theory does neither account for stretching of the beam for large displacements (change in length) nor for the intrinsic stress of the material (extra pulling force at the ends), these two other contributions can be added to achieve a better approximation. Considering that we are pulling a beam that can change its length, this change due to the stretching force is given by the definition of Young Modulus [141],

$$E = \frac{F L_0}{A_0 \Delta L}, \tag{3.4}$$

where F is the force along the beam, A_0 is the original cross-sectional area through which the force is applied, ΔL is the change in length due to the force and L_0 is the original length of the bridge. Now, again considering displacement perpendicular to the bridge, we can estimate the contribution to the restoring force by considering a simplified system where the resistance to stretching dominates the restoring force (a string). Considering equation 3.4, making respective trigonometric approximations and a Taylor expansion, we can write the following equation which relates the string's restoring force to the displacement x produced:

$$F_{stretch} = \frac{8 E_{SiN_x} A_0}{L^3} x^3. \tag{3.5}$$

Similarly, the effect of stress on the restoring force can also be estimated from the definition of Young's modulus by considering the presence of an additional force, which stretches the string even before it is displaced and represents the stress in the silicon nitride membrane. For this case, the restoring force due to the membranes' stress is given by,

$$F_{stress} = \frac{4 S A_0}{L} x, \tag{3.6}$$

where S is the intrinsic stress of the membrane.

Finally, the total restoring force may be estimated by adding the contributions arising from bending of the beam (beam theory), stretching of the beam and the intrinsic stress of the beam. For our situation of a rectangular beam cross-section $A_0 = wt$ the restoring force is,

$$F(x) = \frac{32E_{SiN_x}wt^3}{L^3}x + \frac{8E_{SiN_x}wt}{L^3}x^3 + \frac{4Swt}{L}x, \tag{3.7}$$

where w is the width, L is the length and t the thickness in the displacement direction. We can now estimate the magnitude of the restoring force for the structures discussed in the previous section, i.e. meander cut, triangle cut and chevron cut. Between designs the main difference is that the meander and triangle designs may be approximated by straight silicon nitride beams, while the spring-like design of the chevron structure can be approximated by a straight beam with a lower effective Young's modulus. For a typical beam of 500 nm width, 35 μm length and 50 nm thickness manufactured from a low stress (S $\leq$ 250 MPa) silicon nitride membrane, we can expect a restoring force on the order of 1 nN for a displacement of 100 nm. For the more elastic chevron design the restoring force will be weaker for the same displacement. Nevertheless, the above considerations indicate that forces on the nano-Newton scale will be required to achieve significant deformation of reconfigurable photonic metasurfaces based on silicon nitride bridge beams. Finally, it was shown that not only stronger electromagnetic coupling between bridges but also weaker elastic restoring force is achieved with the chevron cut design. The next section will provide estimates on the magnitude of the available forces for reconfiguring such metasurfaces, i.e. Joule heating causing differential thermal expansion and the magnetic Lorentz force.

3.3 Actuation Mechanisms

Several actuation mechanisms can be considered to reconfigure metasurfaces where an electrically conductive path is present. In our case, all considered designs have an electrically conductive gold layer covering the dielectric bridges. Therefore actuation of such metasurfaces can be achieved by simply applying currents to a subset of bridges. Here we consider thermal and magnetic actuation. The next sections of this chapter

will provide estimates for thermal actuation by resistive heating and magnetic actuation based on the Lorentz force. These two actuation mechanisms were chosen due to simplicity of the apparatus to be used and also because of the big displacements achievable by Joule heating and the fast reconfiguration expected from the Lorentz force, which is not limited by thermal timescales. Considerations about each mechanism, the magnitude of the resultant forces and the magnitude of the observed change in the optical properties will be made for the design that has shown the most promising results, the chevron cut design. We will focus on the chevron cut design as the previous sections indicate that it can deliver both larger displacements and a higher displacement sensitivity of optical properties than the other considered structures.

3.3.1 Thermal Actuation

Since we aim to tune the optical properties of metasurface structures by reconfiguring their nanoscale components in response to different control signals, estimates on the magnitude of available forces should be made. One promising approach is to use thermal actuation, which will lead to out of plane displacement of heated bridges. Despite not being as fast as other mechanisms, it will induce very large physical displacement and therefore large changes of optical properties. Around 1840, James Prescott Joule investigated several physical effects which became known as Joule's Laws. His first law, also known as Joule effect or resistive heating, relates the heat (P) generated in a conductor with its resistance (R) and the current flow (I) [142],

$$P = RI^2. \tag{3.8}$$

This effect is caused by the interaction of current carriers and the atomic ions that constitute the main body of the conductor. Collisions between charged particles, accelerated by an electric field, and the ions, will transfer kinetic energy to the lattice. The increase in the vibrational energy of the ions, manifests itself as heat. Conductive cooling of an electrically heated bridge can be described by the heat equation [143],

$$\mathbf{q} = -\kappa \nabla \vartheta. \tag{3.9}$$

where $\mathbf{q}$ is the heat flux density, κ is the materials thermal conductivity and $\nabla\vartheta$ the temperature gradient. A simple estimate for the maximum temperature on our structure can be obtained by considering the 1 dimensional (x) form of the previous expression,

$$q_x = -\kappa \frac{d\vartheta}{dx}, \tag{3.10}$$

$$\int d\vartheta = \int -\frac{q_x dx}{\kappa}, \tag{3.11}$$

where the heat flux q_x for uniform resistive heating of the bridge is:

$$q_x = \frac{P_{bridge}|x|}{Lwt}. \tag{3.12}$$

P_{bridge} is the power dissipated per bridge, L is the bridge length, w the bridge width, t the bridge thickness and x the position along the bridge, from the centre (x=0) to the ends ($\pm L/2$). By substituting equation 3.12 in equation 3.11 and since the maximum temperature is reached at the centre of the bridge, we can integrate the expression from the bridge centre to the bridge end ($x = 0$ to $L/2$ and maximum temperature to ambient temperature). In this way, the temperature variation will be given by:

$$\Delta\vartheta = \frac{P_{bridge}L}{8wt\kappa}. \tag{3.13}$$

Considering gold as the only thermal conductor (κ=318 $\mathrm{Wm^{-1}K^{-1}}$ [144]), with thermal conductivity about 10 times higher than silicon nitride, we estimate the maximum temperature reached at the centre of our chevron bridge to be 200 K, for 0.05 mW per bridge (see section 3.5). Experiments with currents on the order of 1 mA per bridge are observed to lead to melting of gold at defects in typical samples like those discussed in section 3.1. Given that the melting point of bulk gold is 1064 °C [144], this implies that temperatures of hundreds of degrees are achieved in typical samples at currents of hundreds of μA per bridge. Changing the temperature by tens of degrees will increase the average distance between ions due to their vibrational energy increase and will result in a volumetric expansion of the material. Materials that expand at the same rate in every direction are called isotropic, for these materials the area and linear thermal expansion coefficients may be calculated from the volumetric coefficient. Depending

on the application or dimensions considered important, different coefficients may be considered. In our case, the linear expansion coefficient is considered due to the 1D nature of our structures were the length of the bridges is much bigger than width and thickness. For this situation, the variation (ΔL) of the bridges length (L) for a certain temperature change ($\Delta\vartheta$) is related by the linear expansion coefficient (α_L) [145]:

$$\frac{\triangle L}{L} = \alpha_L \Delta\vartheta. \tag{3.14}$$

Thermal expansion coefficients vary from material to material and if we consider a bi-layer structure of two different materials, one dielectric (e.g. silicon nitride, $\alpha_L = 2.8\times 10^{-6}/K$ [146]) and one metal (e.g. gold, $\alpha_L = 14.4 \times 10^{-6}/K$ [147]), the different change in lengths results in bending of the structure.

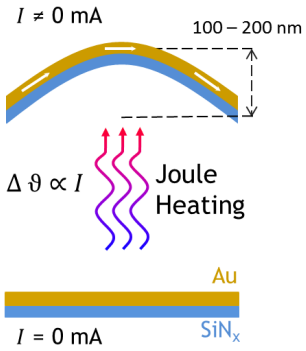

Figure 3.4: ***Thermal actuation concept.*** *Upon electric current (I) application, a bilayer beam fixed at both ends will experience Joule heating which will result in out of plane bending of the beam. Such bending can result in hundreds of nanometres displacement at the centre of a beam that is 10s of microns in length.*

Figure 3.4 illustrates how thermal actuation can be driven by Joule heating where out of plane displacement of a bilayer beam results from differences in thermal expansion coefficients. In this work, currents will be applied to a metasurface and flow along every second bridge in order to change the electromagnetic interaction between neighbouring bridges. Joule Heating of the current-carrying, bilayered bridges will result in out of plane movement of hundreds of metamolecules. Several hundreds of nanometres out of plane displacement might be achieved [148] and the influence on optical properties could be huge. Electrothermal actuation could result in good optical contrast for transmitted and reflected waves with no risk of irreversible switching of the structure. Such actuation is possible at ambient temperature conditions and does not require any

complex apparatus. This new type of reconfigurable metasurfaces promises a simple and practical way for active control of light.

3.3.2 Magnetic Actuation

While thermal actuation promises large tuning, it is inherently slow as it is limited by the cooling timescale on the order of microseconds. In order to overcome this disadvantage, one promising approach is to use the Lorentz force on a current carrying wire placed in a magnetic field to reconfigure metasurface nanostructures. In principle, this allows the metasurface's optical properties to be conveniently modulated by the applied current and thus it has the potential of being a practical method for fast control of metasurface properties. In Figure 3.5 the concept of Lorentz force tuning of a metasurface bridge is illustrated.

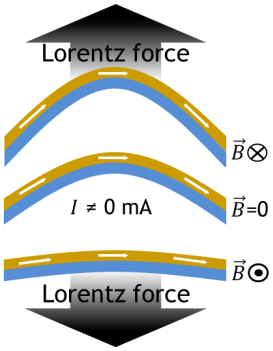

Figure 3.5: ***Magnetic actuation concept.*** *Moving charges (electrical currents) in the presence of a magnetic field oriented perpendicular to the current experience the Lorentz force. Such force can be used for fast reconfiguration of metasurfaces with beam displacement in a chosen direction.*

The practical realization requires currents to be applied to selected reconfigurable parts of the metasurface nanostructure, which needs to be placed in a magnetic field oriented perpendicular to the current flow. The resulting force can be directed upwards or downwards depending on the directions of the magnetic field and current. Assuming realistic values we can estimate the Lorentz force exerted on our bridges. Here, we treat our bridges as current carrying wires. The force acting on a current in a magnetic field is given by [149],

$$\mathbf{F} = L\mathbf{I} \times \mathbf{B}. \tag{3.15}$$

Considering realistic values: I = 1 mA, L = 35 μm, B = 0.1 T, forces of about 3.5 nN

should be achievable. This estimate for the Lorentz force is on the same order of magnitude as the elastic restoring force estimated in section 3.2 for 100 nm displacement of a typical silicon nitride beam of the same length. This suggests that the Lorentz force can significantly deform photonic metasurfaces and thus be used to control their optical properties. Even if for such magnitude of forces the achieved displacement would be only a few tens of nanometres, due to the strong coupling between metamolecules separated by nanoscale gaps, strong changes in the optical response can be expected.

3.4 Fabrication and Characterization

Careful study indicates that the chevron metasurface exhibits the most strongly coupled "trapped mode" resonance (section 3.1) as well as the largest achievable displacements (section 3.2) promising the highest modulation of optical properties amongst several investigated designs. Both electrothermal and magnetic actuation (section 3.3) are expected to produce actuation on the scale of 100 nm in such structures. Here we step forward to the fabrication of such metasurface and, finally, measurement of its optical properties. The reconfigurable nanostructure chosen for practical reconfiguration of metasurfaces by electric currents and magnetic fields was fabricated by focused ion beam milling. Before nanofabrication of our metasurface, a 50-nm-thick gold layer (for the plasmonic metasurface and contact electrodes) was thermally evaporated through a shadow mask (subsection 2.5.1, Figure 2.10) onto a commercially available 50-nm-thick low-stress silicon nitride membrane, which is 500×500 μm^2 in size and supported by a silicon frame.

Firstly, NanoPattern Generation Software (NPGS) is used to create the metasurface array by designing one single unit cell and creating an array by repetition of this unit cell. Using focused ion beam milling (FEI Helios 600 NanoLab), the chevron pattern is then milled through both gold and silicon nitride layers, creating both the plasmonic resonators and the supporting suspended silicon nitride bridges in one step. Then the terminals at the bridge ends were electrically separated by removing the gold film in selected areas. The fabricated metasurface sample is shown in Figure 3.6.

In order to address the metasurface electrically, our substrate (a gold-covered silicon nitride membrane on a silicon frame) is placed in a specifically designed holder, shown

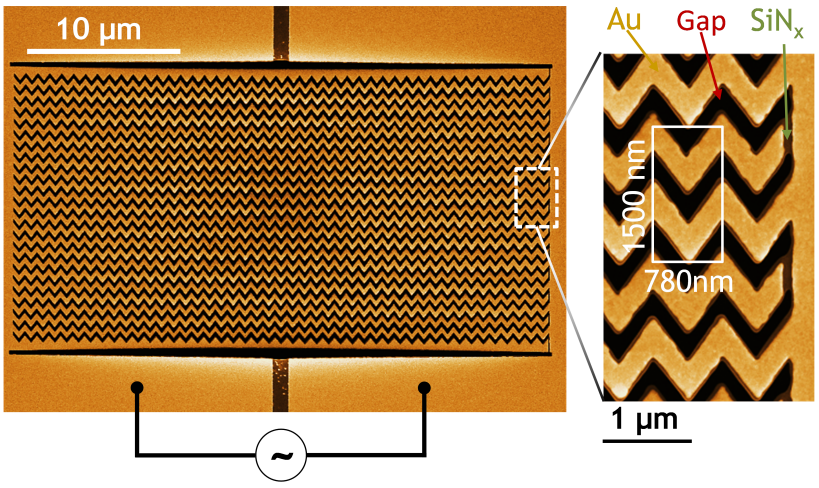

Figure 3.6: ***Reconfigurable photonic metasurface.*** *False coulored scanning electron microscope (SEM) image showing the reconfigurable photonic metasurface. The inset shows an enlarged metasurface section, where a metamolecule has been highlighted and the electrical connections at the bridge ends can be clearly seen.*

in section 2.6, Figure 2.16 a), prior to fabrication. The overall size of the metasurface array is 35 μm×20 μm and its period is 780 nm along the bridges. Removal of the gold layer at one end of only every second bridge limits the electric current flow to alternating bridges. In this way, we displace every second bridge of our array changing the coupling between metamolecules and thus the metasurface's optical properties. However, out-of-plane motion of every second bridge will increase the nanostructure's periodicity perpendicular to the bridges from 750 nm to 1500 nm, leading to a regime of tunable diffraction in the near infra-red. All imaging of the nanostructure was conducted using the scanning electron microscopy mode of the focused ion beam system. *In situ* electrical characterization and observation of the electrothermal displacement are achieved by SEM imaging of the metasurface under current application.

Using a vacuum feed-through connected to a source measurement unit (Keithley 2636) we can electrically actuate the metasurface and simultaneously observe the bridge movement. Two comparative images of the central part of our metasurface are shown in Figure 3.7, currents of 0 mA and 5 mA applied to the whole structure (0 mA and 0.4 mA per electrically connected nanowire). After confirming out of plane movement of the electrically connected bridges relative to the stationary ones, we proceed with the optical characterization of our metasurface with and without applied currents and/or

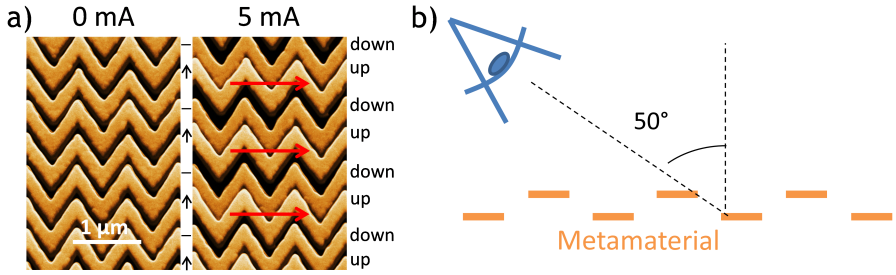

Figure 3.7: ***Electrothermal metasurface actuation under SEM.*** *a) False colour SEM images taken with 0 mA and 5 mA current applied to the metadevice. The images were taken at 50° from the normal to visualize the out-of-plane deformation of the nanostructure and current-carrying bridges are marked by red arrows. b) Schematic of the SEM viewing angle onto our metasurface.*

magnetic fields.

Transmission and reflection spectra were collected from the central portion of the reconfigurable metasurface using a microspectrophotometer (CRAIC Technologies) while applying various currents (via the source measurement unit) and magnetic fields (using neodymium magnets) to tune the mechanical configuration of the nanostructure. Such experiments were made using the magnet holder shown in section 2.6, Figure 2.16 b).

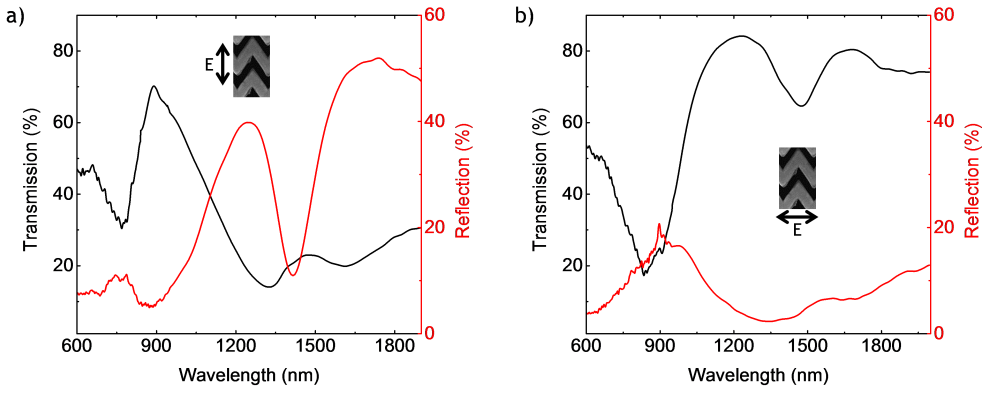

Figure 3.8: ***Optical properties of our chevron metasurface.*** *Transmission and reflection reference spectra of the nanostructure in absence of currents and magnetic fields. a) light polarized perpendicular to the bridges. b) light polarized parallel to the bridges.*

Initially, reflection and transmission spectra are measured for both incident light polarizations without any stimulus applied, see Figure 3.8. These measurements will be used as reference in order to calculate relative transmission changes. Sharp resonant features exist at specific wavelengths for both polarizations. Transmission spectra show a strong resonance at 900 nm for both polarizations, while in reflection only the polar-

ization with the electric field perpendicular to the chevron bridges shows a pronounced resonance at 1.3 μm. The Q-factor of the resonances is limited by FIB resolution and fabrication imperfections as well as absorption losses in the gold layer. Comparing experimental and simulated transmission spectra for light polarized perpendicular to the bridges, we can observe an extra bump around 1.5 μm indicating that a small pre-displacement after fabrication is present and that the effective periodicity of our metasurface in this direction is 1.5 μm (rather than 750 nm).

After complete optical characterization of our metasurface, similar measurements under electric current application and, later, simultaneous application of electric currents and magnetic fields, were conducted. In the optical experiments performed with electric current application the incident electric field was polarized perpendicular to the bridges. Transmission and reflection changes were measured for a range of currents, both positive and negative. Sweeps in current while measuring optical spectra using the CRAIC microspectrophotometer (see section 2.6, Figure 2.18) were conducted in order to evaluate reversible tuning. Finally, magnetic tuning was studied under Lorentz force actuation of our metasurface. As it was not practical to change the magnetic field direction, all data points plotted for negative magnetic field values actually correspond to the equivalent configuration with positive magnetic fields and negative currents, which results in the same Lorentz force and the same electrothermal properties. Both electrothermal and magnetic tuning results are presented and discussed in the following section.

3.5 Results and Discussion

Synchronous rearrangement of about 1000 plasmonic resonators at the nanoscale is achieved exploiting two simple physical principles: (i) bilayers consisting of materials with different thermal expansion coefficients will bend in response to temperature changes and (ii) electric charges moving in a magnetic field will be subject to the magnetic Lorentz force, see Figure 3.4 and Figure 3.5. Selective resistive heating of alternating bridges and thus their deformation by differential thermal expansion, as well as selective magnetic deformation of current-carrying bridges when the nanostructure is placed in a magnetic field, will change the coupling between neighbouring resonators

and therefore the optical properties of the metasurface. The reconfigurable photonic metasurface, which is shown by Figure 3.6, consists of an array of plasmonic V-shaped resonators, which give rise to optical resonances in the near infra-red. In order to allow movement of the nanostructure, the gold resonators are flexibly supported by silicon nitride bridges, which deform easily due to their spring-like chevron shape. Placing sub-micron scale plasmonic resonators on much longer elastic support structures allows us to realize a reconfigurable photonic metasurface without moving parts on the size scale of a metamolecule. Changes of the inter-resonator coupling require relative movement of the bridges, therefore every second bridge has been electrically connected to both electrical terminals at the bridge ends, see the inset to Figure 3.6. Application of a voltage across the device terminals leads to electrical currents and resistive heating in all 12 electrically connected bridges. Due to the large thermal expansion coefficient of gold (14.2×10^{-6} K^{-1}), which exceeds that of silicon nitride (2.8×10^{-6} K^{-1}) by a factor of 5, the electrically connected bridges bow upwards [148]. This is illustrated by Figures 3.7 a) and b), which show the central part of the nanostructure for a viewing angle of 50° from the normal to visualize the out-of-plane deformation when currents are applied. The central portion of the current-carrying bridges is raised continuously by about 200 nm as the magnitude of the applied device current is increased to 5 mA and the bridges return to their original position when the driving current is withdrawn. This continuous and fully reversible change in the physical arrangement of the nanos-

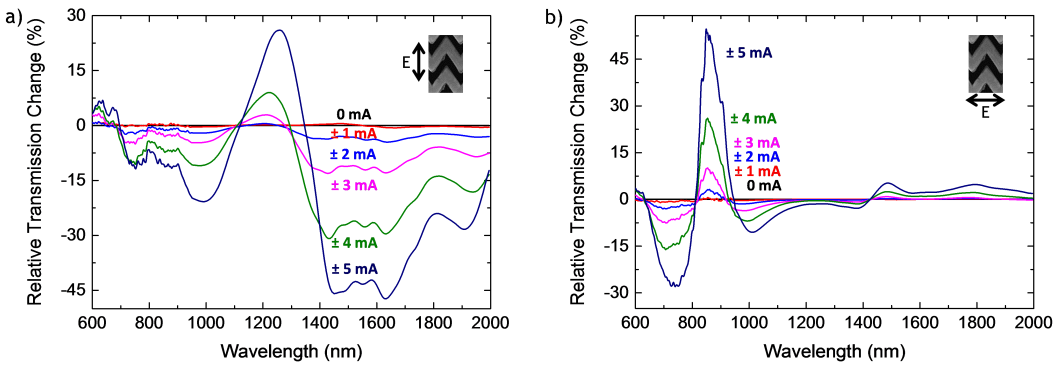

Figure 3.9: ***Electrothermal tuning of transmission.*** *Spectral dependence of the current-induced transmission change relative to a reference case where no current is applied. Positive and negative currents lead to the same transmission change within experimental accuracy, the plotted curves show the average for each current magnitude. a) The incident light is polarized perpendicular to the bridges. b) The incident light is polarized parallel to the bridges.*

tructure is accompanied by dramatic changes in the metasurface's optical properties. For example, transmission for electromagnetic waves polarized perpendicular to the bridges increases by up to 26% in the diffracting regime around 1250 nm and decreases by up to 47% in the non-diffracting regime around 1600 nm, see Figure 3.9 a). Transmission for electromagnetic waves polarized parallel to the bridges increase (decrease) by up to 45% (30%) around 780 nm wavelength, which corresponds to the period of the nanostructure along the bridges, see Figure 3.9 b).

The dependence of the metasurface's reflectivity on electrothermal actuation is shown by Figure 3.10. Similar characteristic behaviour to the one reported for transmission measurements is observed for reflected waves. For light polarized perpendicular to the bridges, main change in reflection occurs in the diffracting regime, but significant reflectivity changes of about 15% are also observed in the non-diffracting regime (Figure 3.10 a)).

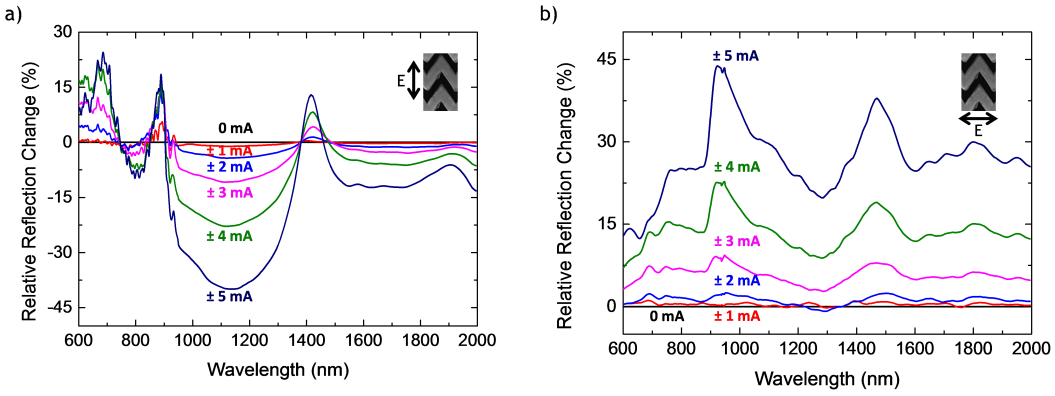

Figure 3.10: ***Electrothermal tuning of reflection.*** *Spectral dependence of the current-induced reflection change relative to a reference case where no current is applied. Positive and negative currents lead to the same transmission change within experimental accuracy, the plotted curves show the average for each current magnitude. a) The incident light is polarized perpendicular to the bridges. b) The incident light is polarized parallel to the bridges.*

Meanwhile, for waves polarized parallel to the bridges, reflection of our metasurface shows spectrally broad tuning with peaks around the periodicity of metasurface' unit cell, both parallel (780 nm) and perpendicular (1500 nm) to the bridges. Reflectivity increases from 600 nm to 2 μm wavelength are measured to be 30% on average, with peaks up to around 40%, with 5 mA applied device current. All electrothermal changes of the metasurface's optical properties do not depend on the current direction. Similar

continuous and reversible changes of at least 40% are observed in transmission and reflection for both eigenpolarizations. In all cases, characteristic electromagnetic resonances of the metasurfaces are tuned by a simultaneous resonance shift and an intensity level modulation. Resistive heating, differential thermal expansion and the resulting bridge displacement are all proportional to the power dissipation in the nanostructure, which is proportional to the square of the applied current. This quadratic current dependence of the nanostructure's physical configuration can be seen in the electrothermal changes of its optical properties, which resemble a parabola when plotted as a function of current, see Figure 3.11.

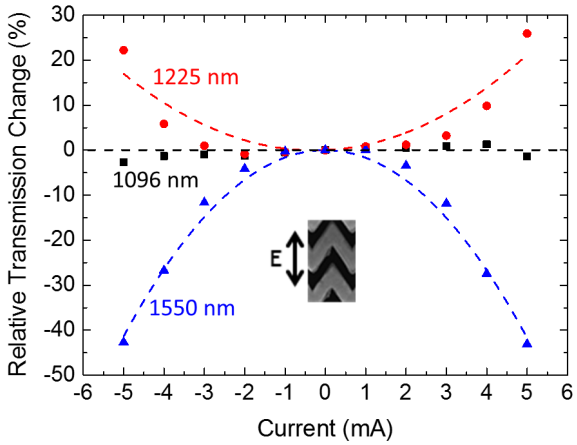

Figure 3.11: ***Electrothermal tuning of transmission: current-dependence.*** *Relative transmission change as function of applied current for characteristic wavelengths, where dashed lines show parabolic fits. Results plotted are extracted from Fig. 3.9 a) for representative purposes.*

Based on the nanostructure's measured resistance of $R = 22\ \Omega$, the device power consumption at a current of $I = 5$ mA is $RI^2 = 550\ \mu$W. Considering conductive cooling, this corresponds to an equilibrium temperature at the centre of the current-carrying bridges that is raised by about 200 K, which is consistent with the observed 200 nm bridge movement as a bridge displacement in the region of 1 nm/K is expected from beam theory [148]. While electrothermal tuning of metasurface properties offers large contrast, its response time is inherently limited by the cooling timescale of the nanostructure, which is about 10 μs. This limitation does not apply to non-thermal driving mechanisms and therefore we propose the use of the magnetic Lorentz force, which responds as quickly as applied currents or magnetic fields can be modulated. A

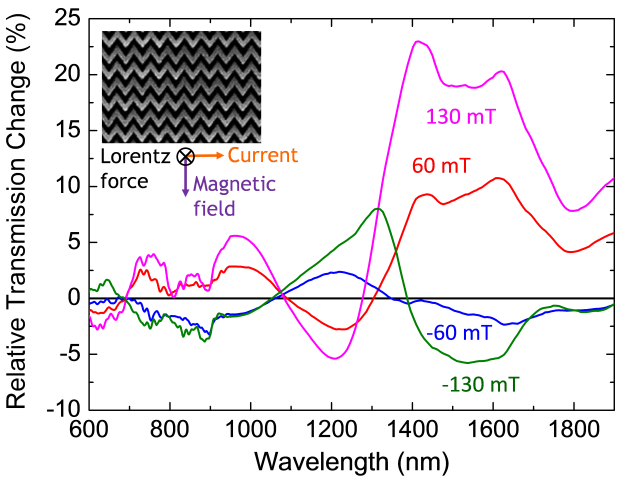

Figure 3.12: ***Magnetic tuning of metasurface transmission.*** *Spectral dependence of the relative transmission change resulting from application of various magnetic fields to the metasurface device while a constant 4 mA current is applied. The applied magnetic field and the electric field of the incident wave are directed perpendicular to the plasmonic metasurface bridges in the metasurface plane. See section 2.6, Figure 2.18, for more details on the experimental setup.*

magnetic field $\mathbf{B}$ in the metasurface plane and perpendicular to a bridge of length L carrying a current $\mathbf{I}$ will lead to a Lorentz force $\mathbf{F} = L\mathbf{I} \times \mathbf{B}$ acting perpendicular to the metasurface plane. Depending on the mutual directions of current and magnetic field, this force can be directed upwards, increasing the electrothermal deformation, or downwards, reducing the electrothermal deformation. The manifestation of this can be clearly seen in the metasurface's optical properties. Figure 3.12 shows how the transmission of the metadevice with 4 mA applied current is changed by the magnetic field.

The metasurface's transmission changes continuously as a function of magnetic field, reaching magnetically induced transmission increases of more than 20% when 130 mT are applied, corresponding to a Lorentz force of about 1.5 nN per bridge and tens of nanometre bridge displacement. Magnetic modulation of the metasurface's optical properties on the background of a constant electrothermal effect can be easily achieved with a constant static magnetic field by modulating the current direction, leading to 25% transmission modulation for ±4 mA currents and 130 mT magnetic field without being limited by thermal timescales. For positive currents and magnetic fields, the Lorentz force is directed downwards, pushing the current-carrying bridges back into the

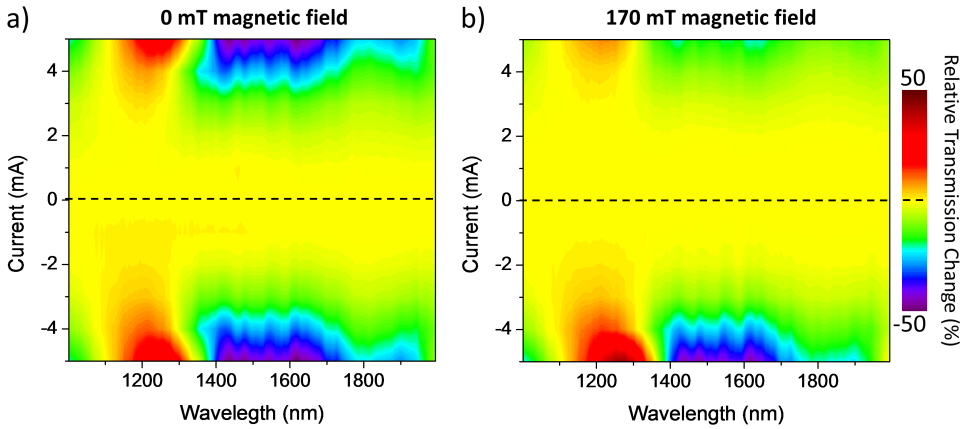

Figure 3.13: ***Electrothermally and magnetically induced transmission changes of chevron metasurface.*** *Relative transmission changes for waves polarized perpendicular to the chevron bridges depending on wavelength and applied current for a) electrothermal tuning and b) magnetic tuning.*

metasurface plane and comparison with Figure 3.9 a) reveals that this largely reverses the electrothermal transmission changes discussed above. On the other hand, reversal of the direction of magnetic field (or current) reverses the Lorentz force direction such that it increases the electrothermal deformation and the associated transmission changes. Colour maps showing relative transmission changes for both electrothermal and magnetic tuning depending on applied current and wavelength are presented in Figure 3.13.

Our measurements show how the introduction of the magnetic field changes the current-dependence of our metasurface's optical properties from fully symmetric, respecting current direction application, for electrothermal tuning to asymmetric for magnetic tuning. The physical deformation of the nanostructure influences its optical properties by affecting inter-metamolecular coupling, strength and spectral position of associated resonances, and diffraction. In general, this leads to a complicated relationship between optical properties and bridge displacement, which may be approximated as linear for small bridge movements. The plasmonic resonators are most strongly coupled when their spacing is small, leading to high sensitivity to mechanical rearrangement. Thus, a reduction of the gap between the bridges resulting from a reduction of the applied current (Figure 3.9 and Figure 3.10) or application of a magnetic field directed to counteract the nanostructure's electrothermal deformation (Figure 3.12) leads to large changes in the metasurface's optical properties throughout the studied spectral range.

Electrothermal and magnetic control of reconfigurable metasurfaces is not limited to gold chevron resonators, but it can in principle be applied to any array of metamolecules that can be supported by a set of bridges. This way, tunability can be added to metasurface arrays with all sorts of useful functionalities. Where the metamolecules themselves do not provide a continuous electrical path, an additional layer of an electrically conductive material such as a transparent conductive oxide can be added and in case of electrothermal control an asymmetric layering of materials with substantially different thermal expansion coefficients needs to be chosen to ensure that resistive heating will lead to structural deformation. In general, the achievable modulation amplitude is controlled by the mechanical, electrical and optical properties of the nanostructure, applied electrical currents and magnetic fields. Both the electrothermal and magnetic displacements and thus modulation amplitudes may be increased by using longer bridges manufactured from a more elastic membrane. Larger modulation can also be achieved by increasing the sensitivity of the metasurface's optical properties to nanoscale displacements through reduced spacing of metamolecules that are optimized to be strongly coupled. Larger magnetic tuning may be achieved by increasing both magnetic fields and electrical currents, resulting in a larger Lorentz force. In particular, higher quality gold films (e.g. single crystal films) would allow both higher currents and lower operating temperatures by reducing resistive heating. It is interesting to compare our electrothermal and magnetic control of reconfigurable photonic metasurfaces with the thermal [70], electrostatic [71] and optical [72] control mechanisms reported in the literature for similar structures. Large scale reversible tuning with optical changes on the order of 50% can be achieved via ambient temperature changes, electrical currents and magnetic fields. However, the required ambient temperature changes on the order of 100 K will be slow and impractical for most applications [70], while electrical currents of a few mA for electrothermal deformation are easily implemented and effective up to tens of kHz modulation and magnetic modulation allows higher modulation frequencies at the expense of slightly higher complexity due to the required external magnetic field. Electrostatically as well as optically driven modulation has been demonstrated up to MHz frequencies, but modulation amplitudes have been limited to a few percent. In case of metasurfaces based on electrostatically reconfigurable bridges, which necessarily move towards each other in the metamaterial plane, large modulation amplitudes are

prevented by an irreversible switching transition that permanently fuses the bridges if they come too close [71]. Deformation perpendicular to the metasurface plane avoids this limitation in case of thermally, optically, electrothermally and magnetically reconfigurable photonic metasurfaces. In the optically reconfigurable metasurface, the optically-induced deformations are small, preventing high contrast modulation of optical properties. Therefore, electrothermal and magnetic reconfiguration of photonic metasurfaces can exhibit large optical contrast, fast modulation, and convenient electrical control, while avoiding the main shortcomings of previous methods.

3.6 Summary

In this chapter, we report the demonstration of innovative and practical solutions for large-range tuning of reconfigurable photonic metasurfaces compared with previous reported works. Electrothermal tuning, exploiting local resistive heating and differential thermal expansion to reconfigure the nanostructure, provides high contrast metasurface's optical properties modulation. Magnetic modulation, exploiting the Lorentz force on current-carrying reconfigurable parts of the metasurface which is placed in an external magnetic field, can provide high frequency modulation of reconfigurable photonic metasurfaces. We use thin gold films deposited on silicon nitride nanomembranes to fabricate metasurfaces which can be tuned in a practical way and achieve high contrast and high frequency modulation of optical properties. Electrothermal tuning delivers optical contrast on the order of 40% and promises 10 μs response times, while magnetic tuning offers 25% optical contrast without being limited by thermal timescales. High frequency modulation of metasurface optical properties based on these actuation mechanisms is discussed in detail in Chapter 4.

Chapter 4

Magneto-Electro-Optical Effect in Metamaterials

Several linear and quadratic electro- and magneto-optical phenomena are known in natural media as discussed in Chapter 2, section 2.2. Such electro- and magneto-optical phenomena play key roles in photonic technology enabling light modulators, optical data storage, sensors and numerous spectroscopic techniques. However, optical phenomena that depend on the simultaneous application of external electric and magnetic fields in conventional media are barely detectable and are technologically insignificant. Here, we demonstrate a novel and large optical effect that depends simultaneously on application of electric and magnetic field in a linear and reciprocal way. In this chapter, we expand on the concepts introduced in Chapter 3, where tuning of reconfigurable

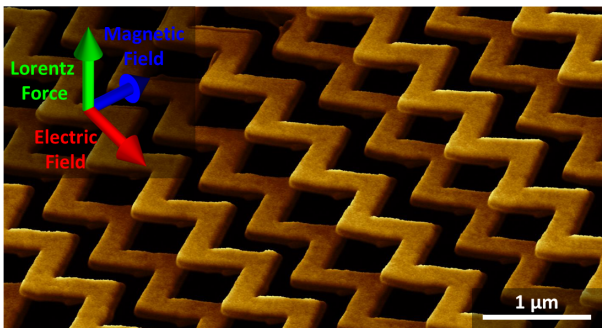

Figure 4.1: ***Lorentz magneto-electro-optical metamaterial.*** *Artistic impression of the nanostructure of current-carrying flexible chevron strips that are driven by the Lorentz force.*

metamaterials with electric and magnetic signals was demonstrated. [1] We explore the relationship of such tuning with other optical phenomena and study high frequency modulation of reconfigurable metamaterials. The metasurface used here is similar in design and operation principle, however, by looking into its frequency dependent optical changes and by separating electrothermal and magnetic effects, a novel magneto-electro-optical effect is reported here. When measurements are preformed applying DC electrical and magnetic signals, the nanostructure will be deformed resulting in tuning of its optical properties. Now, by addressing a similar metasurface using AC signals, a frequency dependent modulation arises and can be further studied. Electrothermal and magnetic effects can be efficiently separated when applying a modulated electrical signal between positive and negative electric signals: electrothermal modulation of the structure's optical properties vanishes at high frequencies and magneto-electro-optical modulation becomes dominant. In order to separate the effects, optical modulation is detected at different frequencies after a laser beam is modulated by the nanostructure. Moreover, making use of the characteristic mechanical resonance of the bridges, both effects can be greatly enhanced.

A large reciprocal magneto-electro-optical effect can be observed in metasurfaces (see Figure 4.1) and is reported in this chapter. In an artificial chevron nanowire structure fabricated on an elastic nanomembrane the Lorentz force drives reversible transmission changes upon application of a fraction of a Volt when the structure is placed in a fraction-of-Tesla magnetic field. We show that magneto-electro-optical modulation can be driven to hundreds of thousands cycles per second promising applications in magneto-electro-optical modulators and magnetic field sensors.

4.1 Magneto-electro-optical Effect

In this work, we report the first observation of a magneto-electro-optical effect that manifests itself as strong changes of optical properties of a metamaterial in response to simultaneous application of external electric and magnetic fields and does not depend on reversal of the propagation direction of the wave. We develop a metamaterial design

[1] In this chapter the term metamaterial is used instead of metasurface since the phenomena are later associated with the physical description of a metamaterial as an effective medium, and not a metasurface of vanishing thickness.

actuated by electric and magnetic fields, similarly to Chapter 3, which provides strong linear optical changes due to coupling change between rows of metamolecules. Our magneto-electro-optical effect may be described by the following term in the constitutive equation,

$$\delta\varepsilon_{ij} = \chi^{(3)}_{ijkl} E_k H_l, \tag{4.1}$$

where $\delta\varepsilon_{ij}$ is the change of the metamaterial's effective dielectric tensor and the associated optical properties due to external electric (E_k) and magnetic (H_l) fields. The strength of the effect is given by $\chi^{(3)}_{ijkl}$. From the equation 4.1, changes in the optical properties depends linearly on the application of both electric and magnetic fields. Similarly to the electrothermal and magnetically reconfigurable metamaterial discussed in the previous chapter, the chosen design is based on a chevron structure with strong coupling and high elasticity, see Figure 4.1. The magneto-electro-optical effect appears concurrently with thermally-induced changes of the optical properties that are driven by resistive heating of the nanostructure.

In general, the Lorentz-force induced change of the optical properties has components that are even and odd functions of the nanowire displacement along the z-direction. Indeed, if initially all strips are located in the plane of the membrane, any change of optical properties is insensitive to the direction of displacement z. However, if alternated nanowires are pre-displaced in the z-direction, the change in the optical properties will be sensitive to the direction of displacement z. As discussed in Chapter 3, in the presence of external magnetic field $\mathbf{H}$, nanowires that bear current are subject to the Lorentz force,

$$\mathbf{F} = L\mathbf{I} \times \mathbf{H}. \tag{4.2}$$

Such force applied to the nanowires will bend them from the plane of the array against the elasticity force to a maximum displacement of few tens of nanometres, see section 4.2. In the reconfigurable metamaterial with anchored ends of the strips, the Lorentz force leads to homogeneous displacement at the centre of the strips, which contributes most to the modulation of optical properties of the metamaterial. While at zero displacement, symmetry dictates identical light-induced charge oscillations in all chevron strips, with displacement of every second strip, charges in neighbouring strips will oscillate with different phase and amplitude giving rise to a change in optical

properties of the metamaterial. This deformation changes the electromagnetic coupling between neighbouring nanowires and thus the plasmonic response of the array at optical frequencies. Such mechanical displacement and the resulting modulation of optical properties will be resonant when the nanowires are driven at their fundamental natural frequency of mechanical oscillation given by [73],

$$\nu_1 = \frac{D}{\pi L^2}\sqrt{\frac{6E}{\rho}}, \tag{4.3}$$

where D, E and ρ are the effective diameter, Young's modulus and density of the nanowire. Driving such metamaterial at its mechanical resonant frequency can lead to an enhancement of such magneto-electro-optical effect, as it will be demonstrated later.

The magneto-electro-optical effect reported here results form the linear response in terms of optical properties when electric and magnetic fields are applied simultaneously. Moreover, reciprocity of the effect with respect to reversal of the light propagation direction is the main distinctive characteristic which makes this work a further illustration of the power of the metamaterial paradigm to create materials with novel properties. In the following section, we will discuss reciprocity in such a system.

4.1.1 Reciprocity

The distinctive characteristic of the magneto-electro-optical effect described in this chapter is not only the linearity observed between changes in optical properties and electrical and magnetic fields simultaneously but also its reciprocity. Therefore, it is important to define this concept and explore ways of measuring it. In optics, the Helmholtz reciprocity principle describes how a light ray and its reverse ray experience same reflection, refraction or absorption. In classical electromagnetism the most common and general formulation of reciprocity is through the Lorentz Reciprocity theorem [21] which states that the relationship between oscillating current and the resulting electric field is unchanged if we interchange the point where both electric current is placed and the electric field is measured. In our experiment, reciprocity measurements can be realized by flipping the sample stage with respect to the incident beam within the setup used to measure the magneto-electro-optical effect, see subsection 2.6, Figure 2.20. In such way, incident light will travel through the sample in both directions without any further

changes to the measurement setup, facilitating reciprocity measurements. Results for both incidence directions will be compared and conclusions about reciprocity of our magneto-electro-optical effect can be drawn.

4.2 Fabrication and Characterization

To create a metamaterial exhibiting strong magneto-electric changes of its optical response we designed a flexible plasmonic nanostructure that can be reconfigured by the Lorentz force upon simultaneous application of external electric **E** and magnetic **H** fields. The metamaterial reported here is an array of separated gold nanowires manufactured from a very thin silicon nitride nanomembrane that was cut into separate elastic chevron strips with 770 nm chevron period along the nanowires (Figure 4.2). In our experiments we targeted the magneto-electro-optical response in the near-infrared part of the spectrum, at telecommunication frequencies.

To engage the Lorentz force we used an array of continuous conductive chevron nanowires of length L along which we applied electric voltage V to introduce an electric field $|\mathbf{E}| = V/L$ and a current **I** that is necessary for the appearance of the Lorenz force, $\mathbf{F} = L\mathbf{I} \times \mathbf{H}$. The nanowire strips form a regular grid with pitch of 775 nm. Alternating nanowires were electrically connected to terminals on both ends (inset Figure 4.2 a)), so that electric field applied across the metamaterial array induces a current **I** in every second strip (Figure 4.2 c)). In the presence of external magnetic field **H**, nanowires that bear current are subject to the Lorentz force $\mathbf{F} = L\mathbf{I} \times \mathbf{H}$ that moves them from the plane of the array against the elastic restoring force to a maximum displacement of few tens of nanometres, see Figure 4.2 d). Optical transmission of the metamaterial has plasmonic resonances in the near infrared, see Figure 4.2 b).

Optical resonances were simulated using the COMSOL software in order to better understand the physics behind the structure's optical properties, field maps are shown by Figure 4.3. Also, transmission spectra were measured using a microspectrophotometer as discussed in section 2.6. The chevron pattern was chosen as it has good longitudinal elasticity due to its spring-like structure, while providing plasmonic optical resonances, continuous electrical paths that can support currents and simplicity in terms of nanofabrication. The reconfigurable nanostructure was fabricated from a

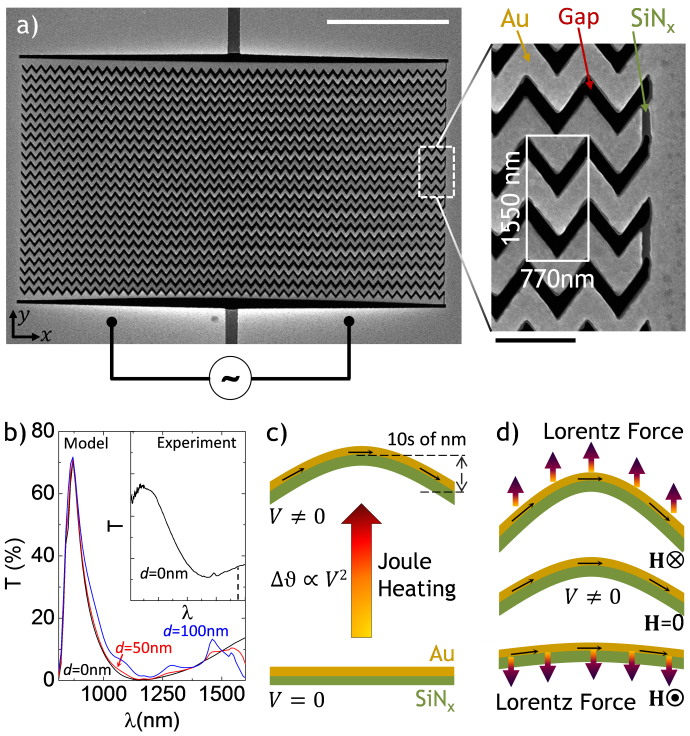

Figure 4.2: ***Lorentz and thermal forces in reconfigurable metamaterial.*** *a) SEM image showing the metamaterial device with chevron nanowires. The white scale bar is 10 μm, the black scale bar in the inset is 1 μm. b) Transmission T of the nanostructure as a function of wavelength λ for several displacements d. Experimental results and numerical simulations are plotted on identical scales and the wavelength used in the modulation experiments is marked by a dashed line. c) Thermal and elastic forces compete in the bilayer nanowire consisting of gold (yellow) and silicon nitride (green) when an applied voltage V leads to a temperature increase Δϑ due to Joule heating. d) Current in a magnetic field* **H** *produces a Lorentz force competing with the thermal effect.*

50 nm thick low stress silicon nitride membrane, which is 500×500 μm^2 in size and supported by a silicon frame. A 50 nm thick gold layer was thermally evaporated onto the membrane and structured with a focused ion beam system (FEI Helios 600 NanoLab), with the contact electrodes connected to a source measurement unit (Keithley 2636) through a vacuum feed-through for *in situ* electrical characterization. Using focused ion beam milling, the chevron pattern was milled through both gold and silicon nitride layers, creating both the plasmonic resonators and the supporting suspended silicon nitride strips in one step. Then the terminals at the strip ends were electrically separated by removing the gold film in selected areas, see Figure 2.11, subsection 2.5.1. The overall size of the metamaterial array is 35 μm$\times$20 μm.

To detect the magneto-electro-optical effect we characterized transmission changes

of the metamaterial induced by simultaneous application of electric and magnetic fields. In order to do so, we used the setup presented in section 2.6, Figure 2.20. Using the holder presented along with the discussed setup, we can apply different driving currents and magnetic fields without changing the sample position or any other experimental parameter. Also, the reciprocity of the effect can be measured by flipping the sample stage to reverse the light propagation direction with respect to the sample.

In all numerical simulations and optical experiments presented in figures of this chapter, the nanostructure was illuminated from the silicon nitride side with the optical electric field polarized perpendicular to the strips. High-frequency modulation was studied with a 1550 nm laser transmitted through the nanostructure, while modulating the electric signal applied to the metamaterial using a signal generator and applying static magnetic fields with neodymium magnets, see section 2.6, Figure 2.20. The modulated signal was detected by an InGaAs photodetector (New Focus 1811) and two lock-in amplifiers (Stanford Research SR830 DSP up to 100 kHz, Stanford Research SR844 RF above 100 kHz). The numerical simulations are full three-dimensional Maxwell calculations based on a finite element method solver (COMSOL). One unit cell consisting of a chevron pair was modelled with periodic boundary conditions. In reciprocity measurements, the sample stage was flipped to switch between illumination of the silicon nitride side and the gold side of the sample. As already mentioned, in bilayer structures the magneto-electro-optical effect will always be accompanied by an electro-thermo-optical effect, however, the magneto-electro-optical effect and the thermal effect can be effectively separated by changing the magnetic field strength. Moreover, with a harmonically modulated external electric control signal the thermal mechanism will respond at the doubled frequency of modulation due to its quadratic nature. However, the Lorentz mechanism will create a modulated optical response at the control frequency.

4.3 Results and Discussion

The out-of-plane motion of every second strip increases the nanostructure's periodicity perpendicular to the strips, so that the metamaterial's unit cell in the dynamic regime is 770 nm $\times$ 1550 nm. Strictly speaking, for the metamaterial to be an effective medium

film, i.e. to transmit and reflect light without diffraction, the optical wavelength shall be longer than the unit cell in all directions. Characterization of the sample was performed at the edge of the effective medium regime of the deformed structure at the telecommunications wavelength of 1550 nm. Therefore, our results shall be interpreted as indication on what changes in ε of a hypothetical homogeneous medium shall be obtained to reach the same modulation depth as the actual nanostructure.

Optical properties of metallic nanostructures, such as the metamaterial investigated here, are determined by the localized plasmonic response of coupled oscillations of conduction electrons and the electromagnetic near-field induced by the incident light. The near-field distribution and thus the plasmonic response are highly sensitive to the geometry of the structure. Therefore, changes on the nanometric scale, that are induced by the action of the Lorentz force, can have a strong effect on the nanostructure's optical properties. The electric near-field component linked to the light-induced oscillating charge separation in the gold layer is the component along the propagation direction, E_z, just above the gold layer. We simulate how this field is affected by displacement of every second nanowire. Displacement-induced changes can be seen in both amplitude and phase patterns for E_z, most dramatically in the latter.

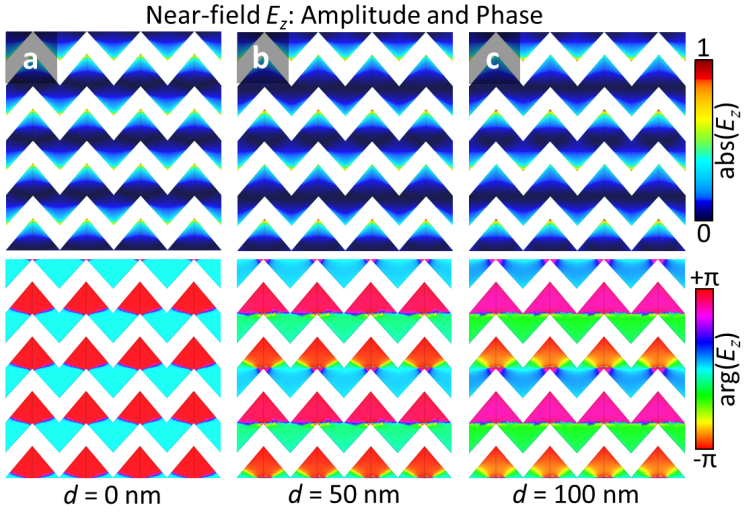

Figure 4.3: ***Electromagnetic response of the magneto-electro-optical metamaterial.*** *To illustrate reconfiguration-induced changes of the plasmonic response of the nanostructure we show the magnitude and phase of the near-field E_z perpendicular to the plane of the metamaterial, 10 nm above the chevron strips. Increasing displacement d from a) zero to b) 50 nm and c) 100 nm leads to a growing phase difference between alternating rows. In these field maps, the nanowires are separated by white areas and the first and third complete chevron strips are being displaced. Incident light is at the wavelength of 1550 nm.*

This is illustrated by Figure 4.3 using somewhat exaggerated levels of displacement (for clarity): the electric field distribution in the near-field of the structure changes dramatically upon out-of-plane movement of every second nanowire of the array. The electro-thermo-optical effect, also reported in Chapter 3, does not depend on the external magnetic field and is not sensitive to the current direction. In the first approximation it is proportional to the power dissipated in the array and thus to $|\mathbf{I}|^2 \sim V^2 \sim |\mathbf{E}|^2$. As the nanowire material used in our experiments was non-magnetic, we observed no optical response upon application of the external magnetic field $\mathbf{H}$ alone. Results for

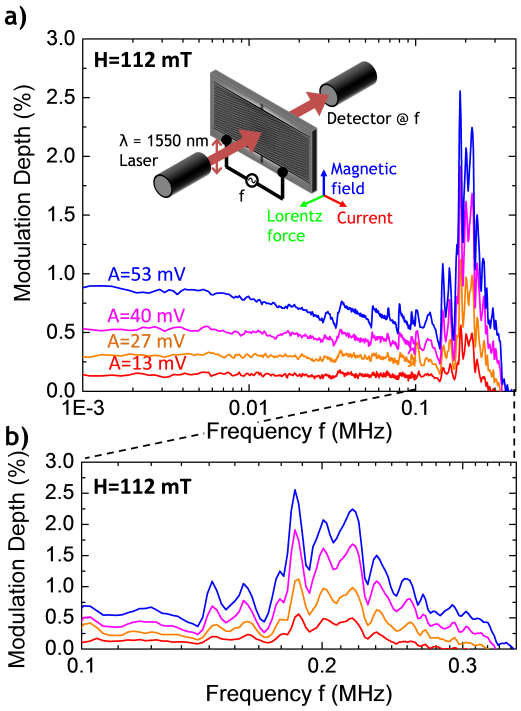

Figure 4.4: ***Magneto-electro-optical modulation of metamaterial transmission.*** *Modulation of transmission ($\frac{\Delta T}{T}$) with an external electrical control signal of amplitude A at different frequencies f in a static magnetic field* $\mathbf{H}$*. Transmission modulation is detected at the frequency of electric modulation.*

non-zero values of the magnetic field strength are presented on Figure 4.4. It shows the optical modulation depth recorded at the frequency f for different amplitudes and frequencies of the control signal $V = A\cos(2\pi f t)$. A high frequency zoom-up displays the resonant feature. The effect has a clear resonant nature (a peak at about 200 kHz, see equtation 4.3) that is related to the mechanical resonance of the chevron nanowires that are supported at both ends. Off-resonance the effect is weakly dependent on the

frequency of modulation. The effect is enabled by the Lorentz force acting against the elasticity of the membrane. Indeed the modulation vanishes at zero magnetic field. Based on the nanostructure's resistance of $R = 27\ \Omega$, a voltage of $V = 53$ mV leads to $I_s = V/(12R) = 160\ \mu$A current in each of the 12 electrically connected strips, corresponding to a maximum Lorentz force of $F_s = LI_sH = 640$ pN per strip in our experiments when $H = 112$ mT magnetic field is applied.

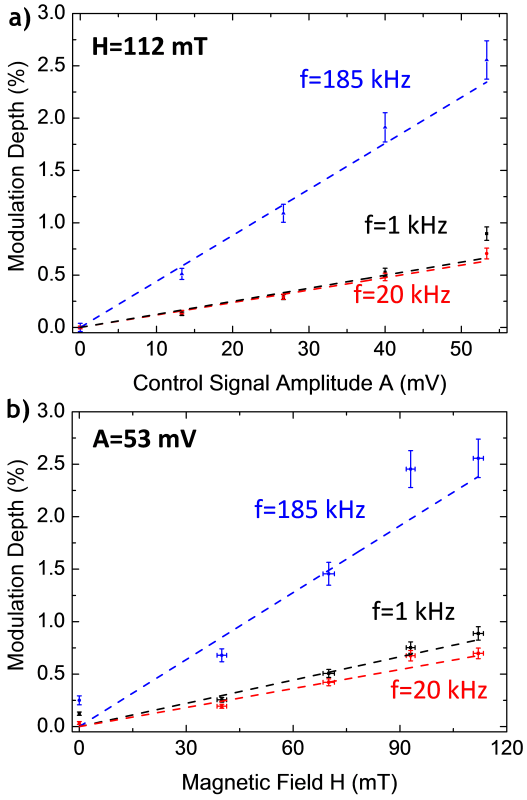

Figure 4.5: ***Magneto-electro-optic effect.*** *Linear relation between transmission change and applied external control signals detected at selected modulation frequencies f. Transmission modulation as a function of a) electric modulation amplitude for a $|\mathbf{H}| = 112\ mT$ static magnetic field and b) magnetic field for a fixed electric modulation amplitude of $A = 53\ mV$ ($|\mathbf{E}| = 1.5\ kV\ m^{-1}$). Error bars show the standard deviation and dashed lines are linear fits through the origin.*

Correspondingly, Figure 4.5 shows the optical modulation depth as a function of control signal amplitude A and magnetic field $\mathbf{H}$ at characteristic frequencies of modulation. The proportionality of the effect to the driving voltage seen in Figure 4.5 a) is only possible if the "hot" nanowires bearing the current are pre-displaced from the plane of the membrane. We argue such displacement results from post-fabrication bow-

type deformation of the sample and/or is induced by the Joule heating of the bilayer nanowires. Indeed, the equilibrium temperature of the heated strips is proportional to power dissipation. The dissipated power at $V = 53$ mV is $V^2/R = 100$ μW, assuming conductive cooling, this corresponds to about 40 K temperature increase at current-carrying nanowire centres compared to their ends. Such temperature increase will cause few tens of nanometres static strip displacement due to differential thermal expansion of gold and silicon nitride [148]. Finally, the results clearly indicate a linear dependence of the sample's transmissivity on the external magnetic and electric fields and this can be described as linear magneto-electro-optical effect, corresponding to a change of the effective dielectric tensor ($\delta\varepsilon_{yy}$):

$$\delta\varepsilon_{yy} = \chi^{(3)}_{yyxy} E_x H_y. \tag{4.4}$$

In contrast, Figure 4.6 a) shows the optical modulation depth recorded at frequency $2f$ at zero magnetic field $\mathbf{H}$ for different amplitudes A and frequencies f of the control signal V. Correspondingly, Figure 4.6 b) shows the optical modulation depth as a function of control signal amplitude A at characteristic frequencies of modulation.

The results show a quadratic dependence of the sample's transmissivity change on the external electric field which shall be expected for the electro-thermo-optical effect. Similar to the magneto-electro-optical contribution, the effect has a peak at the mechanical resonance of the metamaterial. Off-resonance the effect progressively rolls off with the frequency of modulation. Indeed, the electro-thermo-optical effect depends on heating and cooling of the nanostructure, which is controlled by conductive heat transport from the nanowires to the surrounding membrane and then to the supporting silicon frame. Our calculations starting from the law of heat conduction and published values for the thermal properties of 50 nm thick films of gold [150] and silicon nitride [151] predict a characteristic roll-off frequency of few tens of kHz which is consistent with the experimentally observed roll-off (Figure 4.6 a)). Based on the above analysis, electrothermal modulation of the reconfigurable metamaterial becomes ineffective above modulation rates of 50 kHz as the device does not have enough time to cool down in between the heating cycles. In contrast, when modulating our metamaterial in the presence of a magnetic field, a pronounced modulation peak at the nanostructure's

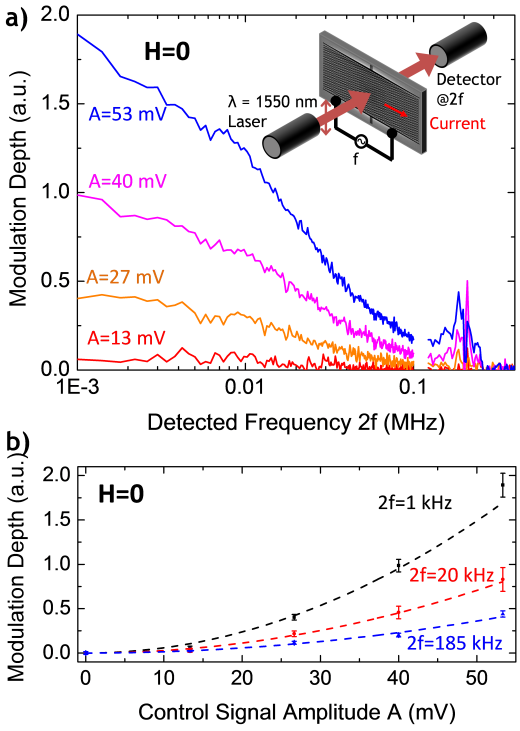

Figure 4.6: ***Electro-thermo-optical modulation of metamaterial transmission.*** *Transmission modulation ($\frac{\Delta T}{T}$) caused by an external electrical control signal at different frequencies without magnetic field. Detection at twice the frequency of modulation $2f$. Modulation depth as a function of a) frequency and b) electrical modulation amplitude. Error bars show the standard deviation and dashed lines are quadratic fits through the origin.*

200 kHz mechanical resonance is observed. The magneto-electro-optical response of our metamaterial can be engaged effectively at frequencies up to the fundamental mechanical resonance of the nanostructure, 200 kHz in our case. In fact, much higher magnetic modulation rates can be expected in stiffer structures with higher mechanical resonance frequencies. Mechanical resonances at MHz frequencies have been reported for a straight bridge design of similar length [71, 72].

We are not aware of any highly flexible natural media structured on the nanoscale with distinctly anisotropic conductivity that could exhibit a similar magneto-electro-optical effect. Therefore our work is a further illustration of the power of the metamaterial paradigm to create materials with novel properties. Here we extend this to the observation of a magneto-electro-optical effect that has never been observed before. We note that Lorentz force based MEMS magnetic field sensors have been

reported [152, 153], but cannot be approximated as effective media. From our experimental data we can estimate the order of magnitude of $\chi^{(3)}$ in,

$$\delta\varepsilon_{yy} = \chi^{(3)}_{yyxy} E_x H_y, \tag{4.5}$$

as $\chi^{(3)}/n \sim 10^{-4}$(m V^{-1} T^{-1}), where n is the effective refractive index of our metasurface. We note that a nonreciprocal optical magneto-electric effect is also known, see Chapter 2, section 2.2. It results from bi-anisotropic constitutive equations that have terms mixing the polarization (magnetization) of the medium with the magnetic field (electric field) of the wave at optical frequencies, resulting in a dependence of the effect on the propagation direction of the wave [4, 81–84]. The phenomenon observed here is different: it results only from the term that describes the change of the dielectric tensor in response to the slowly variable externally applied electric and magnetic fields, which control the deformation of the nanostructure. Such change therefore does not depend on the wave propagation direction, and therefore leads to a reciprocal effect. Control experiments confirm within experimental accuracy that the effect is the same for opposite directions of wave propagation, see Table 4.1.

We argue that although our experiments are performed in transverse magnetic field, a stray component of the field along the direction of light propagating can - in principle - create nonreciprocal circular birefringence (the Faraday effect) in the constituting materials of the nanostructure. However, when probed with linearly polarized light (as in our experiment) it will not give any differential total transmission. Therefore, under our experimental conditions no contribution of the nonreciprocal effect is detectable by the symmetry and choice of polarization of the experiment. The remaining question is if the reciprocal linear or quadratic electro-optical and reciprocal quadratic magneto-optical effects provide a significant contribution to the observed modulation. They do not as the detected modulation is linear in electric and magnetic fields and requires their simultaneous presence.

Both lateral uniformity and magnitude of the observed optical effect can be improved by thinning the chevron nanowires at their ends, which will lead to larger and more uniform displacement of the more rigid central part of the pattern, as has been suggested in [154]. The use of stronger currents and magnetic fields will lead to stronger

Table 4.1: ***Reciprocity of the magneto-electro-optical effect.*** *Difference of the magneto-electro-optical modulation depths $\Delta T/T$ for opposite directions of wave propagation normalized by the magnitude of the effect. Indices SiN and Au mark modulation depths for illumination of the silicon nitride and gold sides of the nanowire metamaterial, which are found to be identical within experimental accuracy. The transmission is modulated with an external electrical control signal of amplitude $A = 53\ mV$ at different frequencies f in a static magnetic field $|\mathbf{H}| = 130\ mT$ and detected at the frequency of electric modulation. The magnetic field is directed perpendicular to the chevron nanowires in the metamaterial plane. Incident light is polarized perpendicular to the chevron nanowires at the wavelength of 1550 nm.*

Modulation Frequency f (kHz)	$\frac{(\Delta T/T)_{SiN} - (\Delta T/T)_{Au}}{(\Delta T/T)_{SiN} + (\Delta T/T)_{Au}}$
1	+0.00 ± 0.07
4	-0.03 ± 0.07
7	-0.04 ± 0.07
10	-0.03 ± 0.07
40	+0.04 ± 0.07
70	-0.01 ± 0.07
100	+0.01 ± 0.07

Lorentz force and larger displacements of the strips, but the Joule heat dissipation and inelastic deformation of the nanostructure will limit the parameter field in which reversible and reproducible changes and consistent signal modulation can be achieved. The main obstacle in achieving higher modulation depth will be thermal damage to the device that we expect to fail at a few hundred millivolts of driving signal. Displacements and optical modulation can also be increased by using longer nanowires to increase the elasticity of the structure and by using more elastic membranes. A considerable increase in the amplitude of high-frequency resonant responses can be attained by reducing the damping associated with the ambient air in which the nanowires move, thus placing the metamaterial in a vacuum cell will help to increase the Q-factor of the response. Furthermore, the design of the plasmonic resonators can be optimized and their spacing reduced in order to couple them more strongly, increasing the sensitivity of optical properties to nanoscale displacements.

4.4 Summary

Electro- and magneto-optical phenomena play key roles in photonic technology enabling light modulators, optical data storage, sensors and numerous spectroscopic techniques. Optical effects, linear and quadratic in external electric and magnetic field are widely known and comprehensively studied. However, optical phenomena that depend on the simultaneous application of external electric and magnetic fields in conventional media are barely detectable and technologically insignificant. In this chapter, we reported that a large reciprocal magneto-electro-optical effect can be observed in metamaterials. In an artificial chevron nanowire structure fabricated on an elastic nanomembrane, the Lorentz force drives reversible transmission changes on application of a fraction of a volt when the structure is placed in a fraction-of-Tesla magnetic field. We demonstrate linear and reciprocal magneto-electro-optical modulation that can be driven to hundreds of thousands of cycles per second promising applications in magneto-electro-optical modulators and field sensors.

Chapter 5

Auxetic Metasurfaces

In analogy to electromagnetic metamaterials, auxetics are often called mechanical metamaterials as their properties result from structuring. One of the unusual mechanical properties presented by auxetic materials is their negative Poisson's ratio. That is the unusual property of expanding both parallel and perpendicular to the direction of an external force that stretches the material. Auxetics with a Poisson's ratio of -1 will expand (shrink) equally in all dimensions upon deformation, resulting in conservation of isotropy of the initial design. This enables the realization of mechanically tunable metamaterials that retain their isotropic or anisotropic optical properties, while tuning for example the intensity or wavelength of transmitted light.

Inspired by the work of Shin *et al.* on auxetic microwave metamaterials [101], we aim to merge mechanical and photonic metamaterials in order to achieve active control of light and to fill the gap between microscale and molecular auxetics. Therefore, we develop micro- and nanoauxetic photonic metasurfaces. We anticipate that the great variety of conceivable auxetic electromagnetic metasurfaces will lead to a broad range of unusual optomechanical properties which is yet to be explored. As such structures enable conservation of optical isotropy in mechanically tunable metasurfaces, we envision applications as isotropic tunable filters and modulators providing polarization-independent control over wavelength, phase and intensity of transmitted light, as well as sensors.

5.1 Optical Auxetic Metasurfaces

For the first time to our knowledge, auxetic metamaterials and photonic metasurfaces are merged at the micro- and nanoscale. In this chapter, we demonstrate nanostructured materials that exhibit simultaneously optical resonances of electromagnetic metasurfaces and the negative Poisson's ratio of auxetic mechanical metamaterials. Figure 5.1 shows one of these auxetic metasurfaces and a mechanical manipulator for load application.

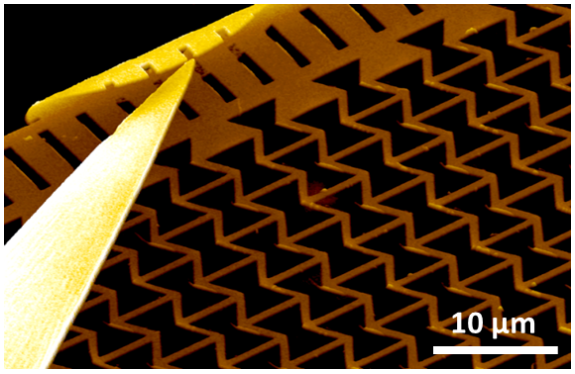

Figure 5.1: ***Microauxetic metasurface*** *of nanoscale thickness. SEM based artistic impression of an auxetic structure actuated by a micromanipulator. The micromanipulator tip applies a force to the metasurface by moving the supporting beam. Such micro- and nanoscale mechanical metamaterials exhibit strong plasmonic resonances in the infrared to optical parts of the spectrum as well as auxetic mechanical properties that are seen upon stretching and compression.*

The nanoscale nature of these structures places this work in the cutting edge of nanotechnology and such structures could in principle enable conservation of optical isotropy of metasurfaces, while frequency selectivity and tunability is also tackled. Tunable optical properties can be achieved in planar metamaterials by synchronous mechanical displacement of thousands of the metamolecules that the metasurface consists of. The optical properties of metallic micro- and nanostructures are determined by the localized plasmonic response of coupled oscillations of conduction electrons and the electromagnetic near-field induced by incident light. Plasmonic response and thus optical properties of metasurfaces are highly sensitive to the geometry of the structure. However, actuation of conventional structures leads to directional geometry changes that will also affect the degree of optical isotropy. By merging electromagnetic metamaterials with mechanical metamaterials (auxetics) this problem can be overcome.

Here we merge mechanical and electromagnetic metamaterials at the nanoscale. We realize micro- and nanoscale metasurface structures and demonstrate negative Poisson's ratios by mechanical actuation (Figure 5.1). Our nanoauxetic structures are not only mechanical metamaterials, but they are also electromagnetic metasurfaces exhibiting strong plasmonic optical resonances in the infrared and optical parts of the spectrum.

Also in this chapter, we were able to improve the quality factor of our electromagnetic resonances by annealing the plasmonic thin film. It is well known how to control thin films deposition in order to control optical, electric and morphological properties [155]. From the deposition technique to the evaporation rates, temperatures or atmospheres involved in the process, very precise control of the microstructure of the final thin film can be achieved. For example, depending on the technique used or on the evaporation rates used during deposition, completely amorphous or fully epitaxial thin films can be obtained. Recently studies have reported on the influence of the gold film structure on the quality factor of metasurface resonances [156]. Such studies highlight the importance of the surface, grain size and general plasmonic thin film quality in order to achieve high quality factor resonances in metasurfaces. Indeed, when considering just the grain size effect, authors reported that increasing it will lead to better quality factors of the plasmonic resonances, when metasurfaces are fabricated. In this work we report a simple and efficient way of improving the quality factor of plasmonic resonances in optical auxetic metasurfaces by application of a potential difference in polycrystalline gold thin films.

5.2 Auxetic Actuation

In principle, auxetic structures can be actuated using the same mechanisms as other reconfigurable metasurfaces, see section 2.1 and Chapter 3. However, in order to be able to obtain clear evidence of the auxetic behaviour of our nanostructures in-plane actuation in one direction is needed, so that expansion or compression in the perpendicular direction can be observed. Instead of providing such a uniaxial load, thermal actuation would produce a difficult-to-interpret overall bending of the structure out of its plane. Mechanical loading resulting in displacement is probably the most reliable way of introducing in-plane actuation. Precise strain measurements in the directions

parallel (axial) and perpendicular (transverse) to the applied force allow the nanostructure's Poisson's ratio to be calculated. Mechanical actuation at the nanoscale can be preformed using a commercially available micromanipulator system (Kleindiek Nanotechnik), see Figure 5.2.

Figure 5.2: ***Micromanipulator*** *used for mechanical actuation of auxetic metasurfaces of nanoscale thickness. The micromanipulator tip applies a force to the metasurface through piezoelectric actuators [157].*

Such apparatus consists of a piezoelectrically actuated mechanical arm with a nanoscale tip that can deliver ultra-precise movement control. Typically, tips are made out of Tungsten and can be obtained with a tip radius, ranging from 30 nm to a few microns (Figure 5.3). The tip's movement is controlled electronically. Such control has various speeds of actuation enabling coarse and fine movement and load application. In order to actuate our structures, we use the micromanipulator tip to push/pull the beam that supports our auxetic structures.

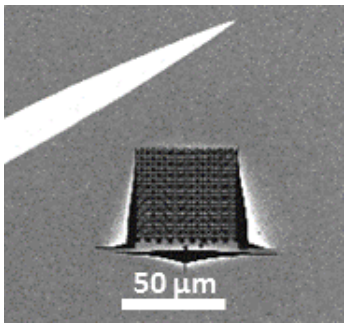

Figure 5.3: ***Micromanipulator tip*** *imaged by SEM inside the focused ion beam system. In the background we can see a typical silicon nitride membrane covered with gold and a metasurface sample.*

By using micromanipulator actuation inside the focused ion beam system, which also has an SEM mode, we can guarantee a uniaxial load application and, at the same time, image the unit cells using the SEM. Thorough analysis of images obtained

with and without loads stretching or compressing an auxetic metasurface nanostructure allows its Poisson's ratio to be determined by measuring the axial and transverse strains.

In-plane actuation of auxetic structures could also be achieved using electrostatic forces to reposition the supporting beam. In this case, an applied voltage leads to attractive or repulsive forces between the supporting beam and surrounding structures, as explained in Chapter 3. A schematic of this concept is presented in Figure 5.4.

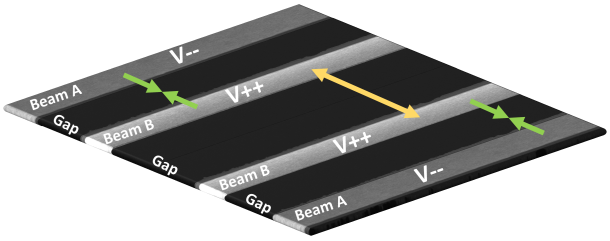

Figure 5.4: ***Concept: Electrostatic actuation.*** *In-plane nanoscale displacement controlled by electrostatic forces between negatively (-, beams A) and positively (+, beam B) charged beams.*

However, such electrostatic actuation would require sufficiently elastic structures to allow significant movement. Attempts to actuate our auxetic metasurfaces using this concept showed that they are too stiff due to the complex design consisting of short interconnected beams. However, the application of electrical voltage to our structures did yield other interesting results which will be discussed later.

5.3 Fabrication of Auxetic Structures

Our micro- and nanoauxetic metasurfaces are based on the re-entrant honeycomb design, which is known for auxetic properties for a wide range of beam thicknesses, sizes and angles [95]. Inspired by recent works in the field of nano-opto-mechanical devices [71,72,109], nanomembrane technology was used to fabricate auxetics with lattice parameters of few microns to hundreds of nanometres. Nanomembrane technology has already provided simple and efficient solutions for reconfiguration of nanoscale structures, enabling nano-opto-mechanical devices and sensors. Moreover, by placing a plasmonic thin film on such membranes, optical excitation can be achieved. The auxetic materials were fabricated by thermally evaporating a 60 nm thick gold layer on a commercially available silicon nitride membrane of 50 nm thickness and then milling the re-entrant honeycomb structure through both layers using a gallium focused ion beam

system (FEI Helios 600 NanoLab). Infrared auxetic materials and nanoauxetic structures were fabricated. The infrared auxetic metasurface microstructures have 7×5 μm^2 rectangular unit cells, an overall size of 60×60 μm^2 and narrow and wide line widths of the honeycomb pattern, respectively, see Figure 5.5 a) and b).

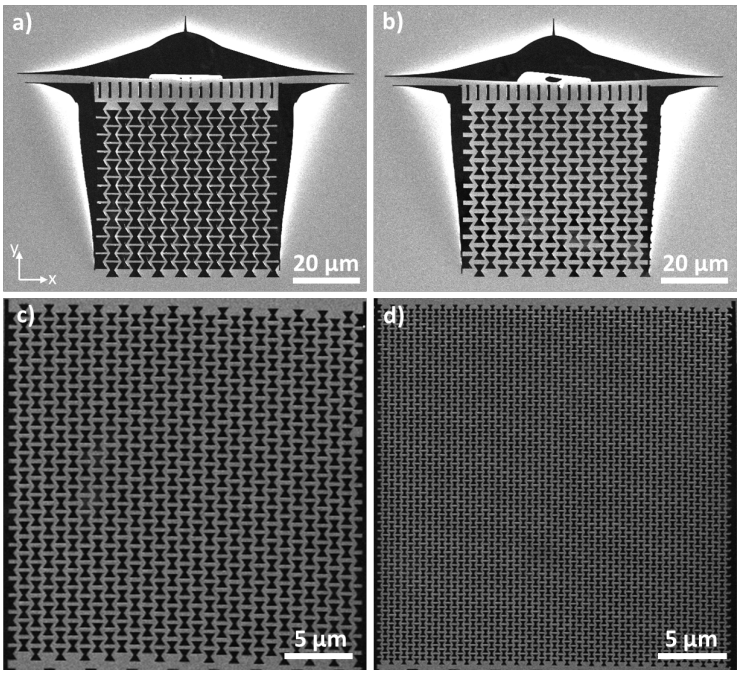

Figure 5.5: ***SEM images of auxetic metasurfaces*** *of 110 nm thickness for the infrared and optical parts of the spectrum with rectangular unit cell sizes of a) and b)* 7×5 μm^2*, c)* 1.8×1.2 μm^2*, and d)* 900×600 nm^2*.*

The optical nanoauxetics are miniaturized versions of the latter with an overall size of 20×20 μm^2 and rectangular unit cell dimensions of 1.8×1.2 μm^2 and 900×600 nm^2, see Figure 5.5 c) and d). Only two sides of the metasurface structures are supported, by the gold-coated silicon nitride membrane on one side and an elastic beam on the opposite side to allow for actuation in the y-direction as well as expansion and shrinking along the x-direction. Upon uniaxial load, the anisotropic metasurface structure will open up leading to expansion both parallel and perpendicular to the applied force.

Also, two other auxetic metasurface samples were fabricated, one being a four-point star shape design and the second one a reproduction of the optical nanoauxetics presented before, see Figure 5.6 a) and b) respectively. These samples were also fabricated from a commercially available silicon nitride membrane of 50 nm thickness. However, on this membrane a thin polycrystalline gold film was deposited using a thermal evap-

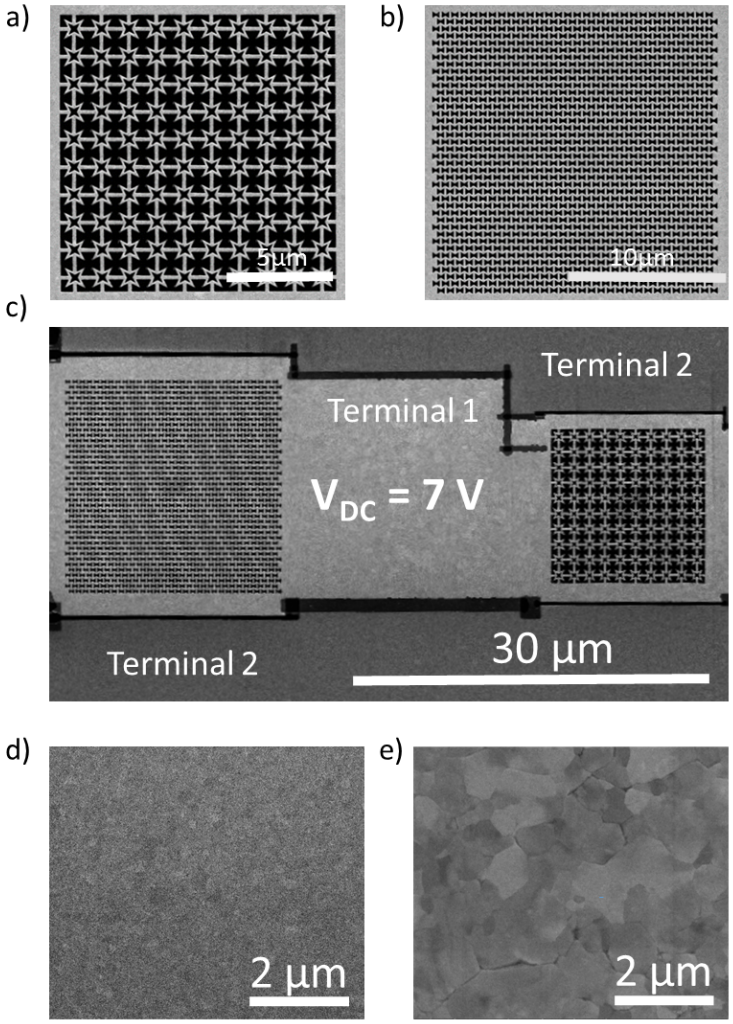

Figure 5.6: ***Auxetic metasurfaces fabricated for electro annealing*** *a) Star metasurface. b) Honeycomb metasurface. c) 7 V were applied to the structures which led to a change in the gold thin film (terminal 1: ground, terminal 2: positive potential). Gold film d) as deposited (polycrystalline) and e) after annealing where grain growth has been promoted by voltage.*

orator. In order to obtain a polycrystalline film, the gold film was deposited at 80° C, with moderate deposition rate (0.10 nm/s) and high vacuum pressure (1×10^{-6} mbar). Using focused ion beam milling, both honeycomb and star shape patterns were milled through both polycrystalline gold and silicon nitride layers, creating both the plasmonic resonators and the auxetic structure in one step. The overall size of the metasurface arrays is 20 $\times$20 μm^2. Finally, the terminals for voltage annealing (intended for voltage application) were electrically separated by removing the gold film in selected areas by focused ion beam milling, keeping the silicon nitride underneath.

In this way, voltage can be applied between 2 insulated electrical terminals. As shown in Figure 5.6, when a voltage is applied across the electrical terminals, the polycrystalline gold thin film of the fabricated auxetics is altered. Initially, as-deposited gold thin films were observed under the SEM and a polycrystalline microstructure was seen (Figure 5.6 d)). Upon application of 7 V the gold film microstructure changes by increasing its grain size as shown in Figure 5.6 e). The possible nature and implications of this increase of grain size in the plasmonic film will be discussed in the next sections.

5.4 Characterization of Auxetic Metasurfaces

In order to measure the mechanical properties of the auxetic metasurfaces, the larger and more robust arrays were actuated using a 100 nm micromanipulator tip (Figure 5.1, section 5.2). The micromanipulator was used to move the elastic beam of 100 μm length that supports one side of the structure resulting in a uniaxial force that stretches or compresses the entire metasurface, depending on the direction of micromanipulator movement. The resulting axial and transverse strains were measured by scanning electron microscope (SEM) observation of the structures in their deformed and relaxed states. Measurements of nanoscale axial and transverse deformations of the metasurface unit cells requires precise measurements of length changes. Therefore, we determined length changes by analysing SEM images recorded with and without micromanipulator actuation systematically. In order to avoid systematic errors, for a given metasurface, images of a chosen unit cell were recorded in sequence with fixed magnification and various applied forces. The axial strain corresponds to the relative length change of the rectangular unit cell along the y-direction.

As the re-entrant honeycomb rectangular unit cell has parallel gold edges that correspond to identical step-like transitions of the image intensity along y (Figure 5.7 b)), statistical errors of the gold edge separation along y were minimized by averaging the central part of the rectangular unit cell's image along x. Axial nanodisplacements due to force application can be seen clearly (Figure 5.7 b)) and the force-induced axial length change of the rectangular unit cell ΔL_y can be extracted, where 1 pixel corresponds to 8 nm. The transverse strain corresponds to the relative length change of the unit cell along the x-direction, ΔL_x, and therefore it is controlled by the force-induced

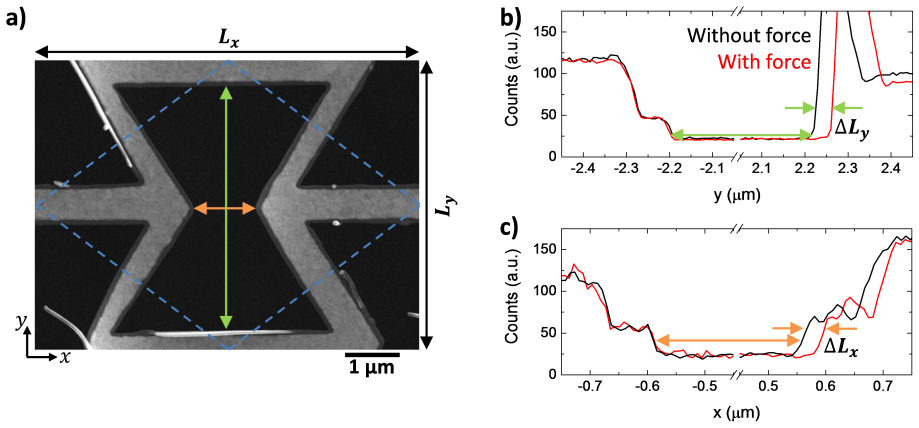

Figure 5.7: ***Strain measurements of auxetic metasurfaces.*** *The axial and transverse strains correspond to the force-induced relative size changes of the rectangular unit cell in the y and x directions, respectively. a) Characteristic dimensions of the unit cell used in the analysis of strain under external force. One rectangular unit cell is shown and the structure's alternative rhombic unit cell is indicated by dashed lines. b) and c) show an example of unit cell deformation along y and x upon application of external force along y. Counts correspond to the pixel brightness retrieved from the image analysis software, where 255 counts are white and 0 counts black. Curves were shifted on the horizontal axes in order to easily visualize the change of the dimensions in both directions.*

gap change between the re-entrant parts of the unit cell (Figure 5.7 c)). In order to minimize statistical errors, this gap change was measured for multiple characteristic distances and then averaged.

Optical characterization of all structures was performed using FTIR and optical microspectrophotometers. To study the effect of voltage-induced grain growth on the optical properties of metasurfaces, optical characterization was conducted before and after voltage application. Mechanical and electromagnetic results are shown and discussed in the next section.

5.5 Results and Discussion

In order to calculate the effective Poisson's ratio of our auxetic metasurfaces, we used the technique described before, section 5.4, Figure 5.7. Axial and transverse strains were measured and results are presented in Figure 5.8. Our measurements show that the metasurfaces expand laterally upon axial stretching and that they shrink laterally upon axial compression.

Thus, the axial - ϵ_{axial} - and transverse - ϵ_{trans} - strains were found to have the same

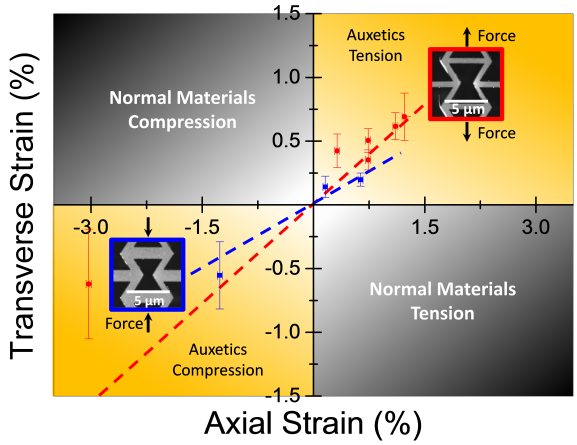

Figure 5.8: ***Auxetics vs common materials.*** *Transverse deformation of infrared auxetic metasurfaces in response to axial tension and compression measured by micromanipulation under SEM observation.*

sign in all cases, corresponding to auxetic behaviour and a negative Poisson's ratio $\nu = -\epsilon_{\text{trans}}/\epsilon_{\text{axial}}$. The deformation of the infrared auxetics with narrow (Figure 5.5 a)) and wide (Figure 5.5 b)) re-entrant honeycomb designs are best described by Poisson's ratios of $\nu_{\text{narrow}} = -0.51 \pm 0.06$ and $\nu_{\text{wide}} = -0.34 \pm 0.09$. As the Poisson's ratio of structured materials does not depend on scaling the size of their unit cell [89, 158], we argue that negative Poisson's ratios of approximately ν_{wide} shall also be expected in case of the more fragile nanoauxetics, which are simply miniaturized versions of the microscale re-entrant honeycomb design with wide beams.

Structuring of the metal-dielectric membrane controls not only its mechanical properties, but also its optical properties. Due to the micro- and nanoscale nature of our structures, they are indeed effective media (electromagnetic metamaterials) when considering infrared and optical radiation with sufficiently large wavelengths to avoid diffraction. Metasurfaces consisting of a simple rectangular lattice of unit cells diffract normally incident radiation if the wavelength is shorter than the longer of the rectangular unit cell dimensions L_x and L_y. However, the re-entrant honeycomb pattern of wallpaper symmetry group *cmm* [159] can also be described by a smaller rhombic unit cell (dashed lines in Figure 5.7a)) and therefore its diffraction threshold, $\lambda_c = L_x sin(tan^{-1} L_y/L_x)$, is given by the distance between parallel sides of the rhombic unit cell.

Therefore, and due to the presence of a plasmonic thin film, typical metasurface

electromagnetic properties arise in such auxetic materials. The optical properties of metallic micro- and nanostructures, such as the auxetic metasurfaces investigated here, are determined by the localized plasmonic response of coupled oscillations of conduction electrons and the electromagnetic near-field induced by the incident light.

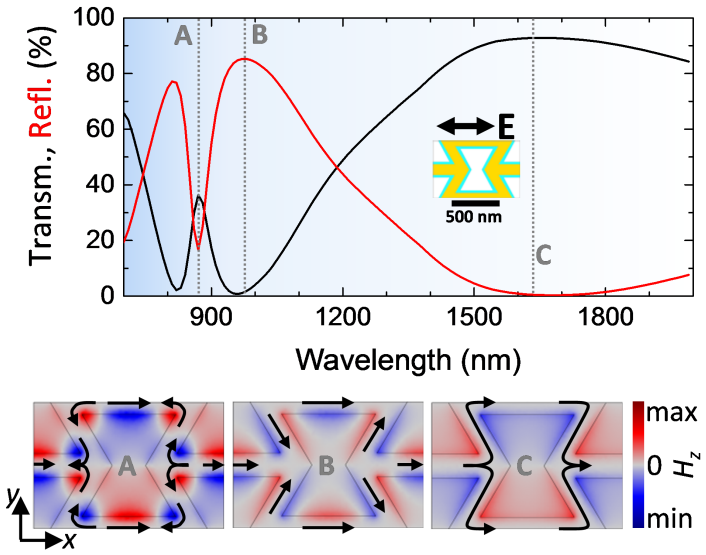

Figure 5.9: ***Plasmonic resonances of auxetic metasurfaces.*** *Simulated reflection (red) and transmission (black) spectra for the nanoauxetic metasurface with rectangular unit cell size 900 nm × 600 nm. The direction of the electric polarization E of the incident wave is indicated. Colour maps show the instantaneous magnetic field normal to the metasurface plane H_z for selected spectral features A, B and C. H_z is linked by Ampère's law to the optically induced instantaneous plasmonic currents, which have been indicated by arrows.*

This is illustrated by Figure 5.9, which shows numerical simulations of the transmission and reflection spectra for the smallest auxetic nanostructure alongside the plasmonic excitations corresponding to selected spectral features (COMSOL). The nanoauxetic exhibits a narrow absorption resonance (reflection minimum A) at about 870 nm wavelength, which corresponds to an anti-symmetric plasmonic excitation also known as "trapped" mode. These anti-symmetric plasmonic currents cannot radiate efficiently, as their radiated fields would cancel in the far-field and therefore electromagnetic energy is trapped at the auxetic metasurface, resulting in large resonant plasmonic fields and about 50% absorption. At about 970 nm wavelength, the metasurface becomes highly reflective (marked B), which is caused by a strongly scattering electric dipole mode, where the x-component of all plasmonic currents oscillates in phase. In contrast, reflectivity vanishes almost completely at around 1630 nm wavelength (marked

C), due to a non-resonant anti-symmetric excitation of the nanostructure. The same trapped mode absorption resonance (A), electric dipole reflection maximum (B) and non-resonant transmission window (C) are also seen in experimental transmission and reflection spectra of the auxetic metasurfaces, see Figure 5.10.

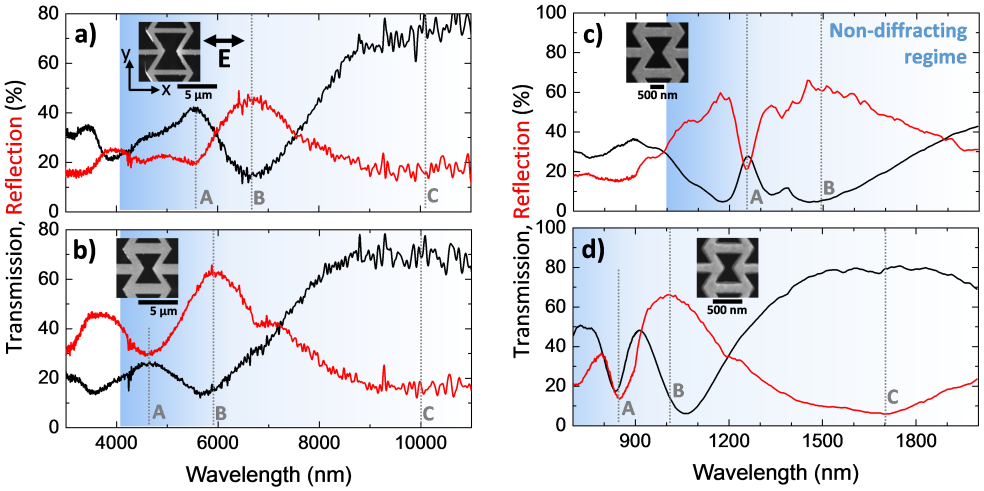

Figure 5.10: ***Optical properties of micro- and nanoauxetics.*** *Reflection (red) and transmission (black) spectra for auxetic metasurfaces based on a) the narrow line width re-entrant honeycomb pattern with a 7×5 μm^2 rectangular unit cell, and b-d) the corresponding wide line width pattern for rectangular unit cells of b) 7 × 5 μm^2, c) 1.8 × 1.2 μm^2 and d) 900 × 600 nm^2. Spectra are shown in the characteristic spectral ranges for micro- and nanostructures, the direction of the electric field polarization* ***E*** *of the incident wave is indicated and spectral features corresponding to plasmonic excitations A, B and C are marked.*

The latter were measured using FTIR (3.0 - 11.0 μm wavelength) and CRAIC (700 - 2000 nm) microspectrophotometers for the micro- and nanostructures, respectively. All auxetic metasurfaces exhibit similar plasmonic transmission and reflection resonances in the nondiffracting regime. The strength and spectral position of these resonances depends on the size and structural details of the plasmonic honeycomb structure as well as the dispersion of the permittivity of gold. A reduction of the honeycomb line width shifts the resonant response further into the infrared (Figure 5.10 a) and b)), while the spectral position of the resonances approximately scales with the overall size of the unit cell (Figure 5.10 b-d)). At this stage of research we were not able to characterize the optical properties of the auxetic metasurfaces under controlled actuation, which would require simultaneous measurements of optical properties and mechanical deformations. However, plasmonic response and thus optical properties of the metasurfaces are highly

sensitive to the geometry of the structure [71, 72, 109].

We argue that actuation of auxetic metasurfaces will lead to pronounced changes of their optical properties such as changes of strength and spectral position of plasmonic resonances. In contrast to conventional materials, where stretching or compression necessarily changes the anisotropy of the structure, auxetics provide an opportunity where the aspect ratio of the unit cell and thus its anisotropy (or isotropy) can in principle remain unchanged [99]. Recent advances in MEMS and NEMS reconfigurable metasurfaces [69, 71, 109] provide solutions for driving actuation of micro- and nanoauxetic metasurfaces electrically, enabling applications in optoelectronic devices, e.g. tuneable wave plates based on anisotropic auxetics and isotropic optomechanical light modulators and variable filters based on isotropic auxetics. Miniaturization of such structures drives up achievable modulation speeds, which are expected to reach GHz on the nanoscale [71, 72] and - in contrast to conventional reconfigurable metasurfaces - auxetic devices can also benefit from enhanced mechanical properties such as fatigue and indentation resistance [91, 160].

5.5.1 Annealing of Auxetic Metasurfaces

After focused ion beam fabrication of the structures shown by Figure 5.6, as-fabricated metasurface optical properties were measured. Later, a voltage was applied to the nanostructures under SEM observation as discussed in section 5.3. Upon application of 7 V between outer electrodes and the electrode with the samples, permanent changes in the morphology of the thin gold film are observed, as seen in Figure 5.6.

After voltage application we remeasured the optical properties for comparison with the previous result. Figure 5.11 a) and b) shows the optical properties for the star-shaped and the re-entrant honeycomb metasurfaces, respectively. The honeycomb auxetic exhibits strong and sharp resonances below 1000 nm while above this value, a broad resonance was measured. The star-shaped metasurface shows transmission and reflection spectra with a pronounced resonance at about 1500 nm while weaker resonances can be observed at shorter wavelengths. Both samples were designed with auxetic properties in mind, however, fragility of the structures did not allow reliable mechanical actuation. In Figure 5.11 a) and b), dashed lines correspond to the spectra measured after voltage application to the structures. For both polarizations of light

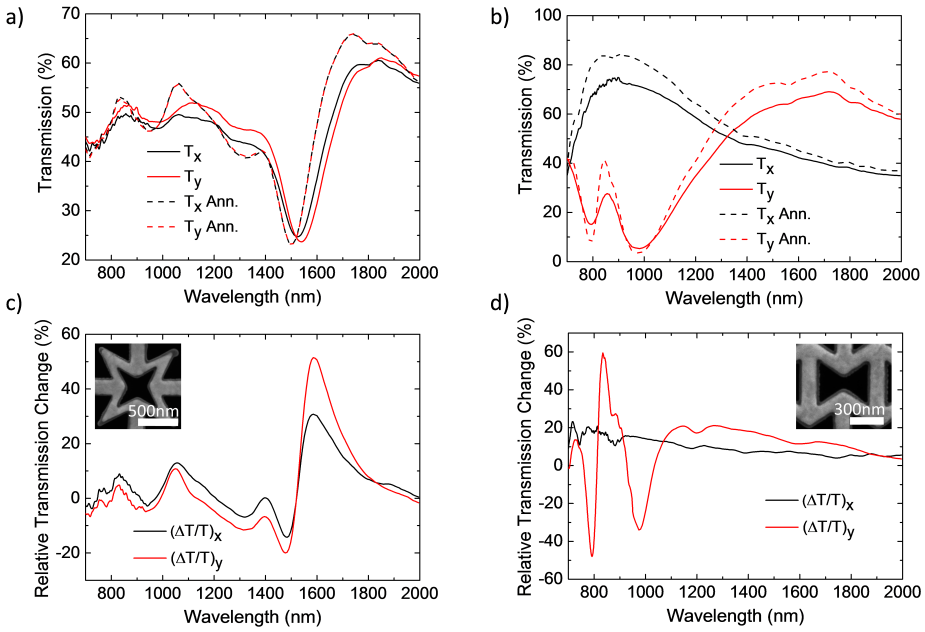

Figure 5.11: ***Transmission changes due to electro-annealing of auxetics.*** *Transmission spectra of auxetics before (solid line) and after voltage application (dashed line). a) Star-shaped design and b) re-entrant honeycomb design. Relative transmission change resulting from voltage application for both light polarizations in c) isotropic star and d) anisotropic honeycomb auxetics.*

and two different structures we observe an increase in the quality factor of the electromagnetic resonances. Figure 5.11 c) and d) shows the relative transmission change for the samples due to voltage application. Up to 60% permanent transmission changes can be achieved by applying voltages to the sample. Such voltage application promotes grain growth in a polycrystalline thin film. Such phenomena can be attributed to the grain boundary movement, causing grain coalescence due to ion diffusion within the film. Since the morphology of the film is the only noticeable difference between the samples before and after voltage application, we argue that grain growth improves the quality factor of the electromagnetic resonances by making the plasmonic structures less lossy.

Moreover, when looking at the relative transmission changes measured for both polarizations, it is interesting that the isotropic structure shows isotropic improvement of the electromagnetic resonances, while the anisotropic structure exhibits anisotropic transmission changes. Voltage application to polycrystalline films seems to be a simple and efficient way of reducing losses and improving the optical response of metasurfaces.

5.6 Summary

In summary, we demonstrate plasmonic micro- and nanoauxetic metasurfaces that exhibit both a negative Poisson's ratio and resonant optical properties controlled by the metasurface structure. Micromanipulation confirms lateral expansion upon axial stretching of the re-entrant honeycomb design and the microscale and nanoscale nanomembrane metasurfaces have pronounced transmission and reflection resonances in the infrared and optical parts of the spectrum, respectively. Moreover, these new interesting structures can enable reconfigurable nano-opto-mechanical metasurfaces which keep their isotropy/anisotropy, depending on the initial design. We argue that small displacements promoted by the external stimulus application, will change the coupling between metamolecules and consequently, optical properties [71, 72, 109]. By merging mechanical and electromagnetic metamaterials, such structures promise a broad range of unusual optomechanical properties which is yet to be explored.

Furthermore, we report the observation of an improvement of the quality factor of the optical resonances resulting from voltage application to such structures. We argue that voltage application promotes ion diffusion and causes the grain growth that was observed. Voltage-annealing induced transmission changes for both polarizations show isotropic resonance improvement due to loss reduction in isotropic structures while anisotropic transmission changes were seen for an anisotropic structure.

Chapter 6

Free-standing Plasmonic Metasurfaces

Previous chapters of this thesis focused on dynamic control of light using spatial reconfiguration of metasurface building blocks. Reconfigurable photonic metasurfaces can provide practical solutions for dynamic control of light, nevertheless, modulation frequencies can hardly reach the speed of light-matter interactions. Another way to dynamically control light has been widely explored [161–165] and it is based on the control of light-matter interaction between a standing electromagnetic wave and an ultrathin metasurface. Our ability to control light with this all-optical mechanism will ultimately allow ultrafast dynamic control over material properties with diffraction-limited resolution [1]. While in reconfigurable photonic metasurfaces light intensity is the main parameter that has been tuned, using the coherent control concept one can easily tune intensity, phase or polarization of light. In the present chapter I report on important results achieved in collaboration with other researchers and explore the concept of coherent control of metasurface functionalities. Results reported concern dynamic control of light intensity down to single photons, in images and on ultrafast timescales. In the present chapter the crucial importance of metasurface fabrication for coherent control experiments is discussed. A fabrication method is developed for ultrathin and optically symmetric (relative to the light propagation direction) nanoscale metallic metasurfaces which provide the ideal platform for coherent control of metasurface functionalities. I report how such structures enabled through collaboration with

other researchers the experimental demonstration of coherent control of light with light (i) at low intensities down to single photons, (ii) with femtosecond optical pulses and (iii) with diffraction-limited spatial resolution. In fact, I fabricated all samples used in these experiments and I report on how to obtain such metasurfaces in the following subsections. I also summarize the experimental results obtained by colleagues in order to illustrate the breakthroughs achieved, however, my contribution to these works was the sample fabrication and scientific discussions for manuscript preparation. The breakthroughs reported may lead to energy-efficient and ultrafast all-optical processing of optical data and images.

6.1 Metasurfaces for Coherent All-Optical Control of Light

The light-matter interaction of a metasurface that is thin compared to the wavelength may be controlled by placing it in the standing wave interference pattern formed by coherent counter-propagating electromagnetic waves [66]. If the structure is located at a node of electric field, it cannot interact with the field, while the electric light-matter interaction is enhanced at electric field anti-nodes. This process enables coherent all-optical control over the expression of the metasurface's effect on the wave.

In order to fully take advantage of this approach, metasurface optical properties are crucial. As mentioned in section 2.4, a metasurface is by definition an ultrathin metamaterial that can be described as a discontinuity of zero thickness in the light path. Such approach allows to describe the discontinuity and consequently the metasurface by its scattering matrix. Such a truly planar metasurface has the same optical properties (light-matter interaction) for illumination of both sides. Here, we are particularly interested in coherent control of absorption of light with light, which will be absent at a standing wave node and maximized at a standing wave anti-node. Perfect absorption at the anti-node requires a thin absorber with 50% absorption, 25% transmission and 25% reflection for a travelling wave at the experimental wavelength [66]. Such characteristics can be achieved based on a metallic free-standing nanomembrane, which will automatically have identical properties for illumination of opposite sides and can be structured to engineer metasurfaces with the required combination of optical properties. Deviations from these characteristics will reduce the achievable absorption modulation

contrast and cause uneven distribution of power between the output beams. Only with careful design and accurate nanoscale fabrication such properties can be obtained and the concept of coherent control of metasurface functionalities be fully explored.

In summary, ideal performance requires a metasurface of negligible thickness, compared to the wavelength of the electromagnetic wave, that absorbs 50% of a single beam illuminating the front or the back of the structure. Moreover, in order to explore the concept of perfect coherent absorption of light, it is desirable to attain a metasurface with optical properties that are independent of the light incidence side. Perfectly symmetric and ultrathin metasurfaces were fabricated and enabled several collaborations that lead to interesting and potentially important results in the field of active control of light with light. Results presented in the remainder of this chapter are based on samples developed by me while measurements were taken by several colleagues namely, Dr. Thomas Roger, Dr. Venkatram Nalla and Ms. Maria Papaioannou.

6.2 Fabrication and Characterization of Free-standing Metasurfaces

The development of ultrathin metasurfaces with identical optical properties for opposite directions of illumination, achieving 50% of absorption, 25% transmission and 25% reflection, at very precise wavelengths was the main challenged tackle in this work. Processes are developed in order to fabricate free-standing plasmonic metasurfaces suitable for coherent control experiments. For optimal performance of such metasurfaces, several requirements shall be met. Most importantly, high resolution nanostructures must be fabricated in plasmonic films of deeply subwavelength thickness. A minimum film thickness of about 50 nm is needed as for thicknesses below 50 nm, focused ion beam milling of high quality nanostructures is compromised by mechanical stability and thermal effects. Another important characteristic of such free-standing plasmonic metasurface relies on the possibility to engineer optical properties through structuring.

By carefully choosing adequate dimensions of asymmetric split ring groove structures, 50% absorption, 25% transmission and 25% reflection can be engineered in such metasurfaces. Finally, another crucial property of such metasurfaces, especially when placed in coherent control networks, is the symmetry of their optical properties with

respect to reversal of the incident wave direction. In coherent control experiments, balance between the two output counter-propagating beams is achieved by having equal percentages of light transmitted and reflected (25% each) regardless of the propagation direction of incident light. Engineering absorption close to 50% can provide high contrast for all-optical tuning. In order to achieve high quality metasurfaces for coherent control experiments, I fabricated free-standing metasurfaces of deeply subwavelength thickness with suitable optical properties, see Figure 6.1.

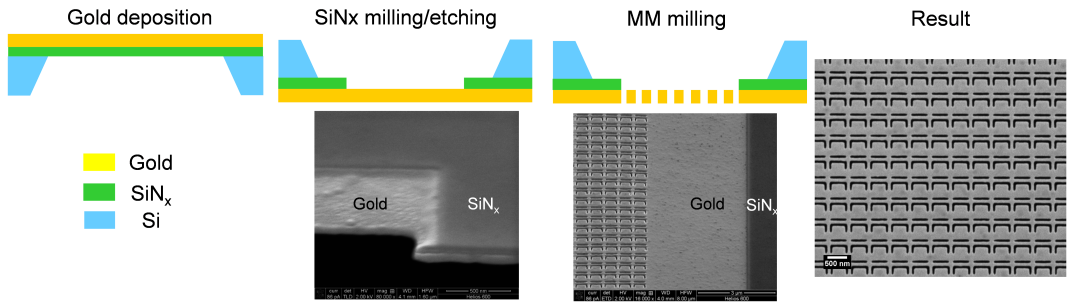

Figure 6.1: ***Fabrication steps for free-standing plasmonic membranes of deeply subwavelength thickness fabricated by focused ion beam milling.*** *A metal film is deposited on a silicon nitride nanomembrane by resistive thermal evaporation. Subsequently, either FIB milling or etching can be used to remove the silicon nitride membrane layer. A symmetric, with respect to the light propagation direction, and deeply subwavelength free-standing membrane is obtained. Finally, FIB milling for strucutring the free-standing layer into a metasurface is performed.*

Firstly, a metallic thin film is thermally evaporated on a commercially available 50 nm thick silicon nitride membrane (NORCADA, low stress $\leq$ 250 MPa) supported by a silicon frame. The thickness of the evaporated plasmonic film can vary between 40 nm and 60 nm depending on the final wavelength of operation, optical properties required and dimensions of the nanostructures. As mentioned before, films thinner than 40 nm make focused ion beam milling of small feature structures on them problematic. Thermal evaporation at low pressure (2×10^{-6}mbar) and moderate deposition rates (0.10nm/s) was performed to obtain suitable gold films.

After deposition of the plasmonic thin film, two different methods for silicon nitride removal were considered. Firstly, using focused ion beam milling, windows of 50×50 μm^2 were fabricated using different dosages, see Figures 6.1 and 6.2. The idea was to reach the plasmonic film from the silicon nitride nanomembrane side guaranteeing a free-standing plasmonic film.

Despite accurate depth control of the milling process, it is difficult to guarantee

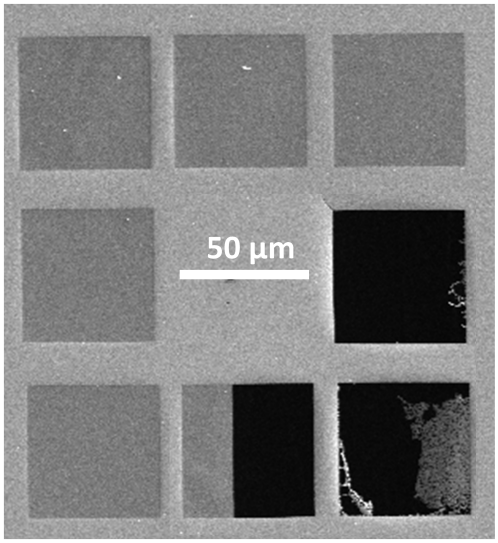

Figure 6.2: ***Free-standing gold membranes fabricated by focused ion beam milling.*** *Ion beam dosage test for free-standing gold membrane fabrication by focused ion beam milling through the silicon nitride side of a gold-on-silicon-nitride nanomembrane. Using the appropriate dosage, the silicon nitride layer can be completely removed and only a free-standing plasmonic film remains.*

complete removal of the silicon nitride layer without milling further into the metal layer. Also, this fabrication technique promotes surface asymmetry in the plasmonic film with respect to the light propagation direction due to ion implantation and different roughness on one side of the plasmonic film.

Another solution explored here in order to achieve symmetric, ultrathin metasurfaces for coherent control experiments is reactive ion etching. As discussed in section 2.5.3, this process allows careful control over the etched thickness of a specific material without affecting the other. In our case, the 50 nm SiN_x membrane can be etched away without affecting the plasmonic film quality. Reactive ion etching can provide the needed selectivity without using any liquid which could compromise the integrity of the final free-standing film due to surface tension forces and liquid solid wettablity. Using a reactive ion etching system (Plasma Lab 80 plus by Oxford Instruments) and a mix of CHF_3 (2 sccm) and Ar (10 sccm) at a process pressure of 6.67×10^{-2} mbar (50 mTorr) we perform reactive ion etching from the silicon nitride side of the gold-coated membrane exposing only the silicon wafer (membrane frame) and SiN_x (50 nm) to the etching plasma. Reactive ion etching is performed under a process power of 80 W during 10 minutes allowing complete removal of the silicon ni-

tride layer, keeping the 40 - 60 nm gold layer intact. However, it is not straight forward to obtain a 50 nm free-standing film from reactive ion etching.

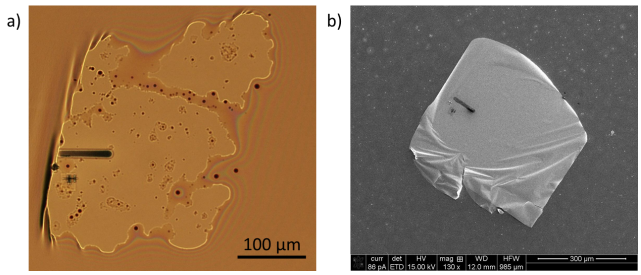

Figure 6.3: ***Failed fabrication of a free-standing gold membrane by reactive ion etching.*** *In initial reactive ion etching tests, the free-standing gold film would end up attached to the glass substrate due to chemical and physical impact on the nanomebrane. a) Optical image and b) SEM image.*

Figure 6.3 shows optical and SEM images of a failed attempt of etching the silicon nitride membrane where the ultrathin gold film ends up attached to the glass support substrate used in the process. Due to physical etching and bombardment of the sample, in addition to removing the SiN_x material, we also promote the "transfer" of the 50 nm thin gold film onto the glass surface that was used to support the sample during the etching process. Figure 6.4 shows how samples are prepared in order to completely remove the silicon nitride membrane without destroying the gold thin film. Silicon frames supporting a gold-coated silicon nitride membrane each are placed upside down on parallel placed *Kapton* tape in such a way that a gap between the gold surface and the glass slab used as a holder is present.

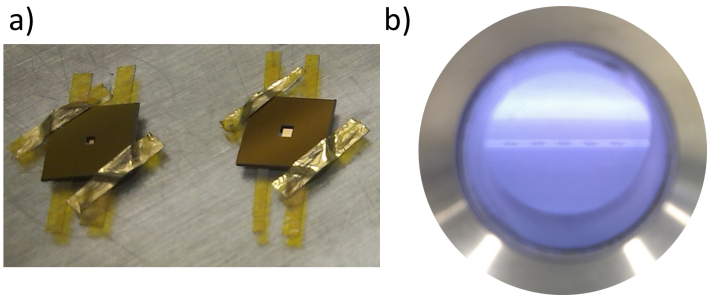

Figure 6.4: ***Sample preparation for reactive ion etching.*** *a) Two strips of* Kapton *tape are used to support each silicon frame and to keep the central membrane away from the glass. Each frame is then fixed to the glass substrate, using two additional strips of* Kapton *tape. This way damage to the gold nanomembrane can be avoided during the reactive ion etching process. b) View through the Reactive Ion Etch system's circular window showing light-purple reactive plasma and the glass substrate with previously prepared samples.*

If such sample preparation is not made, after etching, in addition to removal of the silicon nitride layer the thin gold film will be attached to the glass substrate and the gold nanomembrane will be destroyed. By having this air gap between the thin gold film and the glass holder, we prevent Van der Walls and electrostatic forces to act between the nanomembrane and the glass substrate and a flat and intact ultrathin free-standing gold membrane can be obtained. By the end of this process, a flat, smooth and free-standing 40 - 60 nm gold thin film should be obtained for further structuring of metasurfaces features.

Finally, careful structuring of a metasurface on the fabricated free-standing plasmonic layer is the last step to achieve high quality samples for coherent control experiments. Metasurface structures (such as asymmetric split ring apertures) are then fabricated in a 50 $\times$ 50 μm^2 or 100 $\times$ 100 μm^2 area, using focused ion beam (FEI Helios 600 NanoLab) milling. Depending on the experiment and the samples used, further details will be given in the experimental sections. For coherent control experiments, ideally the fabricated structures have identical optical properties for illumination of their front and back and will absorb about 50% of a single illuminating beam at the design wavelength.

In order to measure optical properties of metasurfaces fabricated on free-standing plasmonic films from both incident light directions, the holder presented in section 2.6, Figure 2.17 was used. This holder allows the optical properties to be measured easily for opposite illumination directions using a microspectrophotometer. Even simple free-

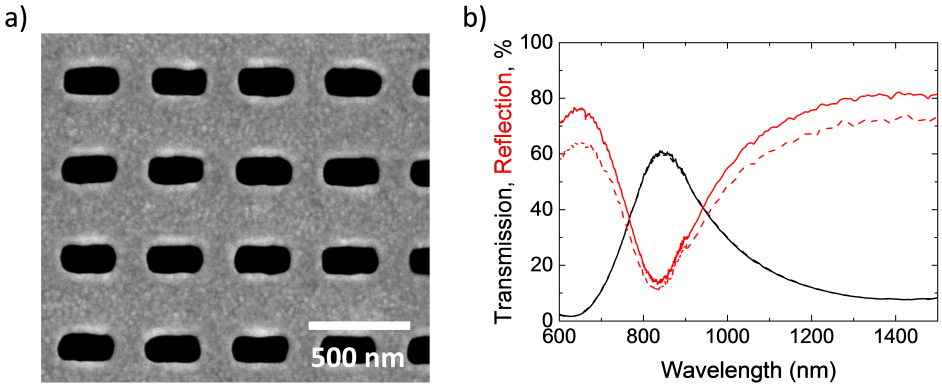

Figure 6.5: ***Optical properties of a free-standing ion beam milled metasurface.*** *Transmission and reflection properties for a metasurface consisting of dipole bar grooves fabricated on a free-standing ion beam milled plasmonic film. Solid lines show measurements for one incident direction while dashed lines show the result for the opposite one.*

standing metasurfaces fabricated by FIB milling have shown pronounced asymmetry of the metasurface reflectivity for opposite sides of illumination, see Figure 6.5. A typical realization of a metasurface (asymmetric split ring grooves) and its spectra for opposite directions of illumination measured using a microspectrophotometer is shown in Figure 6.6. This metasurface was fabricated using reactive ion etching to achieve a free-standing plasmonic thin film. Despite the complexity of the nanostructure, when compared to the simple design presented in Figure 6.5 a), symmetry with respect to the light incidence direction is greatly improved, indicating similar surface properties of both sides of the plasmonic film (roughness, chemical composition).

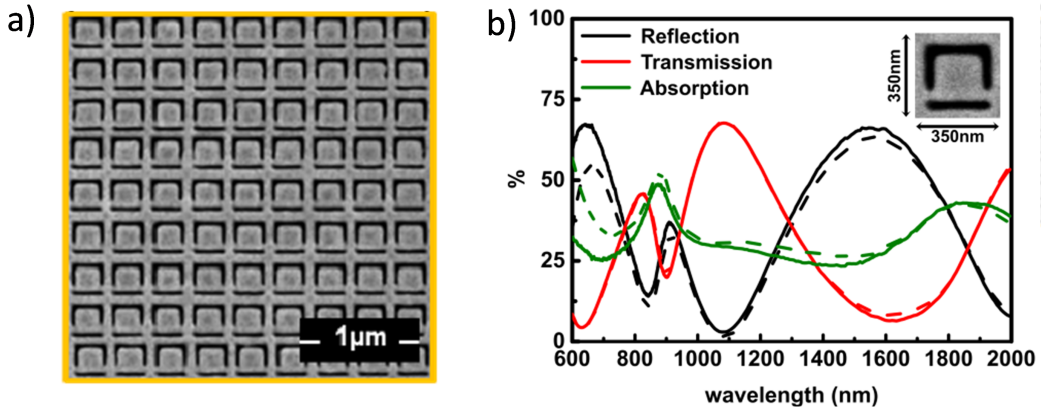

Figure 6.6: ***Typical metasurface fabricated for coherent control experiments.*** *a) Ultrathin metasurface structured by focused ion beam milling from a free-standing gold film fabricated by reactive ion etching achieving b) almost identical optical properties for light incident from opposite sides (corresponding to solid lines and dashed lines). Depending on which experiment and wavelength was targeted, dimensions of the array and unit cell were changed.*

As can be observed from the spectra, almost identical absorption, reflection and transmission are measured for different incident directions of the light beam. Moreover, the metasurface shown here successfully achieves engineered optical properties, showing 50% absorption and reflection equal to transmission (25%) at 860 nm. Therefore, reactive ion etching of the silicon nitride nanomembrane to obtain a free-standing plasmonic film yields better quality samples for coherent control experiments. Finally, after several iterations of processes optimization, free-standing plasmonic metasurfaces of deeply subwavelength thickness (typically 50 nm) were fabricated with a typical line width of 30 nm. Such metasurfaces have all characteristics required for high qual-

ity samples for coherent control of light, that is suitable optical properties (A=50%, R=T=25%) and a symmetric (with respect to the light propagation direction) optical response. By changing dimensions, periodicity and linewidth of the fabricated metasurface, a wide range of operational wavelengths can be achieved.

6.3 All-Optical Coherent Control of Light with Free-standing Metasurfaces

Coherent networks provide an ideal platform in which the recently demonstrated phenomenon of coherently controlled transparency/absorption can be exploited. As discussed in section 6.1, the interference of two counter-propagating coherent beams on a sufficiently lossy metasurface of sub-wavelength thickness can entirely eliminate Joule losses in the metallic nanostructure but can also lead to the total absorption of all incident light, depending on the waves' mutual intensity and phase and on their polarization [66]. Interferometry is used to recombine two coherent light beams on the metasurface creating a standing wave. In general, the relative phase of the two exiting beams can be controlled in order to move the standing wave relative to the metasurface. In the next sections it will be shown that coherent all-optical control of metasurface absorption is compatible with arbitrarily low intensities and femtosecond pulses of light, while being able to provide diffraction-limited spatial resolution.

6.3.1 Single Photon Coherent Perfect Absorption

My contribution to the work discussed in this section is the fabrication of the freestanding metasurface. The experiments reported here have been conducted mainly by Dr. Thomas Roger and Dr. Stefano Vezzoli.

Recent studies provided unexpected but strong evidence that the quantum properties of light are conserved when photons are converted into surface plasmon polaritons, paving the way for active and ultrafast quantum plasmonic technologies [166–172] and stimulating a broad interest for the topic. Extending the control of absorption down to very low light levels and eventually to the single photon regime is of great interest yet remains largely unexplored. Here we demonstrate the coherent absorption of single photons in a deeply sub-wavelength 50% absorber. We show that while absorption of

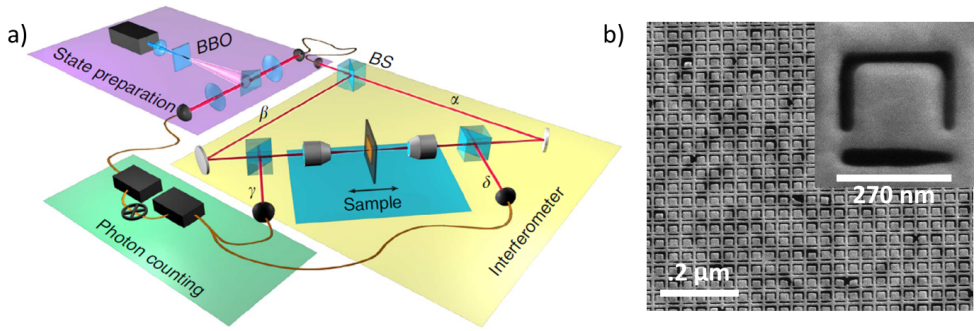

Figure 6.7: ***Single photon experiment on perfect coherent absorption.*** *a) Illumination of a type 1 beta-barium borate (BBO) crystal by a continuous wave $\lambda = 405$ nm laser producing correlated single photon pairs by spontaneous parametric down conversion. The correlated photon pairs are separated by a knife edge prism. One photon of the correlated pair is used to herald the presence of the other photon that is launched into the interferometer. The metasurface absorber b) is placed in the middle point of the interferometer and translated along the optic axis by a piezo-electrically actuated stage. The single photons are focussed onto the sample by 10x objectives. Photons are then detected in coincidence with the heralding photon at outputs δ and γ.*

photons from a travelling wave is probabilistic, standing wave absorption can be observed deterministically, with nearly unitary probability of coupling a photon into a mode of the material, e.g. a localised plasmon when this is a metasurface excited at the plasmon resonance. These results bring a better understanding of the coherent absorption process, which is of central importance for light harvesting, detection, sensing and photonic data processing applications. We demonstrate that a single photon can be coupled to a plasmon mode of a metasurface with nearly 100% probability.

In the experiment (layout shown in Figure 6.7 a)), a single photon launched into the interferometer via a lossless 50/50 beam-splitter generates a coherent superposition state at a metasurface film. By tuning properly the reflectivity and the transmissivity parameters of the scattering process at the metasurface sample, this state evolves in such a way that the probability to observe at least one photon in either of the output channels γ and δ is either 0% or 100% depending on the phase shift between beams. It was demonstrated that when the phase shift between the input beams, α and β, at the metasurface position no photons will be measured in the output channels and correspondingly the single input photon will be totally absorbed with 100% probability. An ultrathin metasurface absorber was fabricated to demonstrate the effect of deterministic single photon-to-plasmon coupling and thus perfect absorption, it exhibits close to 50% travelling wave absorption. The sample was placed at the centre point

of the interferometer. Single photon states were prepared by spontaneous parametric down conversion (SPDC) of a laser diode with emission line centred at the wavelength of 405 nm. We used a beta-barium borate (β-BBO) crystal producing non-collinear, degenerate entangled photon pairs at $\lambda = 810$ nm. The output ports γ and δ were monitored with single photon avalanche detectors gated by the heralding photon channel. The relative phase shift between the input channels was controlled by translating the metasurface film along the light propagation direction with a piezoelectric actuator.

Main results are presented in Figures 6.8 a) and b) showing the output photon count rate in channels γ and δ normalised to the input photon count rate in channels α and β (measured on the same detectors by removing the sample) as functions of the plasmonic absorber position. With a single photon entering the device at a time, we observe periodic oscillation in the output photon count rate as the phase shift between the two input channels changes. The oscillation period of 405 nm corresponds exactly to the $\lambda/2$ period. Here perfect absorption corresponds to the minima of the curve. The overall modulation (Figure 6.8 c)) was measured to be between 90% and 10%.

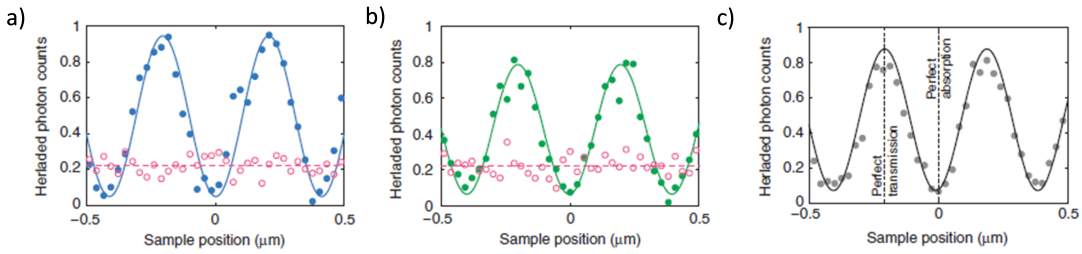

Figure 6.8: ***Single photon perfect coherent absorption.*** *a) and b) show the output photon count rates in channels γ and δ normalised to the input photon count rates in channels α and β as functions of the metasurface absorber position along the standing wave (round, full symbols). Also shown are the results of measurements when the input channel β is blocked (open circles and dashed horizontal fitting lines). c) shows the half-sum of the normalized rates in channels γ and δ. The vertical dotted lines indicate the positions of nodes and anti-nodes, corresponding to almost perfect transmission and absorption regimes, respectively.*

Finally, our setup can be converted for the study of absorption from a travelling wave by blocking the input channel β. In this case we register a position-independent level of the normalised photon count rate in the output channel γ, that indicates the probability of photon absorption (open circles in Figure 6.8 a)). Indeed, by removing the "which-path" ambiguity we are left with only the α-state: the output signal γ is simply determined by the travelling wave transmission coefficient of the metasurface.

We obtain similar results by monitoring the output port δ (open circles in Figure 6.8 b)). We note that absorption in the free-standing metasurface film has a predominantly plasmonic nature related to its nanostructure. Therefore the coherent absorption process implies a nearly 100% efficient coupling of the single photon to the plasmonic mode of the absorber. Hence, our experiment shows that although the absorption process of a single photon in a travelling wave is by its very nature probabilistic, absorption can be made completely deterministic by providing a which-path ambiguity of the standing wave.

Our findings also expose the underlying quantum mechanism of optical gating via the coherent absorption process, which has previously been reported with CW and pulsed signals at classical light levels [5, 66]. The fact that modulation of light can be demonstrated with a single photon proves that the effect of modulation here does not rely upon one photon modulating another e.g via a nonlinearity of the film. Rather, the coherent absorption gate exploits a difference in the absorption probabilities between the two configurations of the gate when the control beam is blocked or open. At higher photon fluxes (i.e. at classical light levels), this takes the form of an interference-controlled re-distribution of the energy flow between the inputs, outputs and the dissipative channel provided by the 50% absorber [173]. In contrast with a gate based on the material's nonlinearity, the coherent absorption gate operates with no harmonic distortion and works at any intensity level.

6.3.2 Ultrafast Coherent Perfect Absorption

My contribution to the work discussed in this section is the fabrication of the free-standing metasurface. The experiments reported here have been conducted by Dr. Venkatram Nalla and the theoretical model was provided by Dr. Xu Fang.

In this work the coherent absorption process was studied with ultrashort optical pulses of variable duration aiming to determine the transient dynamics of this process in a nanostructured plasmonic metasurface absorber and to probe its ultimate speed. Using pulse durations from 6 fs to 185 fs, we show that pulses as short as 11 fs can interact efficiently on the absorber. Similar to most resonant photonic devices in optical data processing networks, the operation bandwidth of coherent control of absorption is considered to be limited by the plasmon relaxation. In our work we fabricate a

device with 90 THz operational bandwidth by precisely engineering the absorption of our metasurface and consequently the plasmon relaxation rate in our structure.

A thin film of subwavelength thickness absorbing 50% of light from a travelling wave will absorb 100% of light incident on the film if placed in the anti-node of a standing wave. Far-reaching implications of the coherent control idea are in all-optical data-processing functions such as all-optical modulation, summation and inversion that can be performed in a 4-port device utilizing a thin absorber [118].

The metasurface plasmonic absorber was fabricated on a 60 nm free-standing gold film. A layer of gold was first evaporated on a 50nm SiN_x membrane that was consequently removed from the backside of the sample by reactive ion etching, as discussed in section 6.2. The grooves forming the metasurface pattern were 25nm in width. They

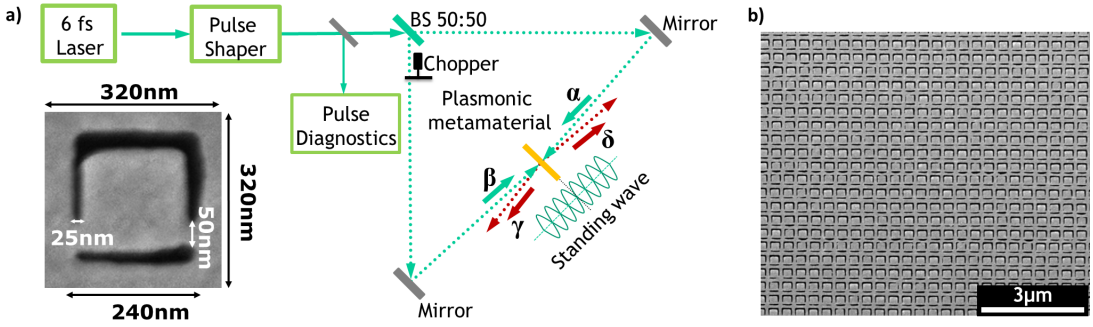

Figure 6.9: ***Probing the ultimate speed of the coherent absorption process.*** *a) A plasmonic metasurface sample is placed in the standing wave formed by counter-propagating femtosecond optical pulses α and β; b) SEM image of a fragment of the plasmonic metasurface absorber, an array of asymmetric split ring apertures in a free-standing gold film. The inset shows the asymmetric split ring unit cell dimensions (apertures are black, gold is grey).*

were cut through the film by focused ion beam milling to create a two-dimensional square array of asymmetric split-ring meta-molecules with a 320 nm× 320 nm unit cell. A schematic of the experimental setup and the metasurface are shown in Figure 6.9.

The plasmonic absorber was placed on a piezoelectric translation stage at the centre point of an interferometer constructed from a 50:50 pellicle beam splitter and broadband metal parabolic mirrors focusing light on the sample from both sides thus forming the standing wave. Broadband 6fs laser pulses were generated by a Ti: Sapphire laser and then spectrally filtered and conditioned by a pulse shaper to achieve the desired pulse duration.

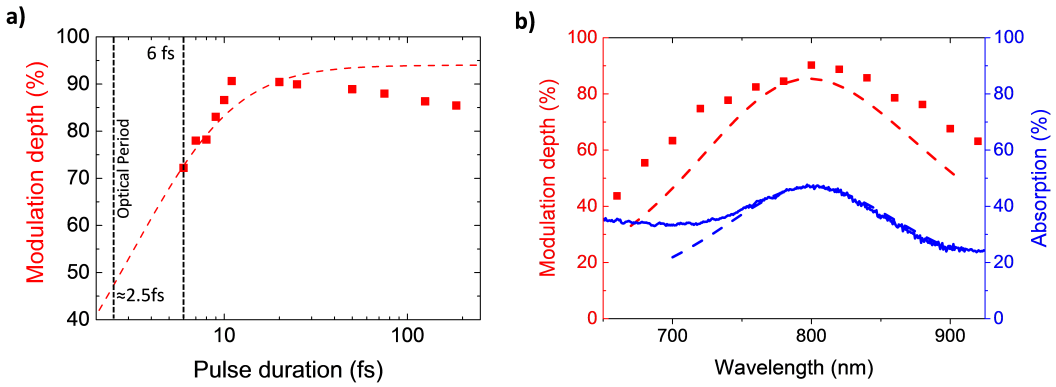

Figure 6.10: ***Coherent absorption of few femtosecond optical pulses.*** *a) Modulation depth as a function of optical pulse duration for our metasurface b) Modulation depth in a standing wave (red) and absorption in a travelling wave (blue) for our metasurface as a function of wavelength. Coloured dashed lines correspond to simulations based on the Lorentz oscillator approximation while the blue solid line and red squares correspond to experimental results.*

Here the absorber acts as a 4-port device with two input ports α and β and two output ports γ and δ, as annotated on Figure 6.9 a). In our experiment we measured the output intensities I_γ and I_δ in both output channels as functions of sample position in the interferometer. Modulation depth of the oscillation, that is the difference between maximal and minimal absorption of the total input energy, as function of the optical pulse duration ($\Delta\tau$) was measured at the centre of the pulse envelope and is shown in Figure 6.10 a). Results show that the modulation depth of the plasmonic metasurface absorber is low for short pulses and rapidly increases with pulse duration reaching a maximum at about $\Delta\tau \approx 11$ fs. Further increase of the pulse duration leads to a slow decrease of the modulation depth. We also measured the dependence of the modulation depth for the metasurface sample at different central wavelengths of the pulse spectrum λ_0 for $\Delta\tau \approx 11$ fs, see Figure 6.10 b). The maximum modulation depth was observed at $\lambda_0 = 800$ nm and coincides with the maximum of travelling wave absorption of the metasurface sample measured with a spectrometer. In the wavelength regime of interest for the ultrafast measurements, the metasurface can be approximated by a Lorentz oscillator with the resonance wavelength at 800 nm, damping constant of $\gamma = \omega_0/4$ (corresponding to a plasmon relaxation time of 11 fs), and the maximal absorption of 47%. Figure 6.10 b) shows both experimental results and theoretical results based on the Lorentz oscillator approximation. Using these three parameters, the coherent

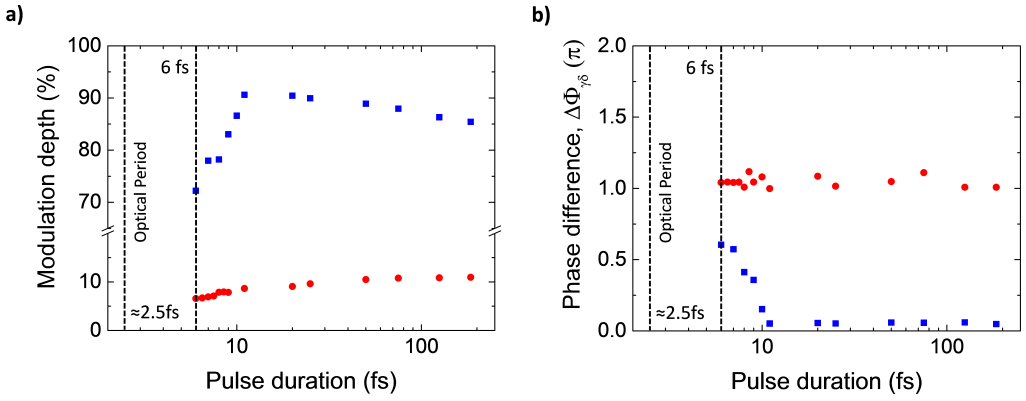

Figure 6.11: ***Ultrafast coherent absorption in metasurface and unstructured gold films.*** *a) Modulation depth and b) phase difference between output signals for the metasurface sample (blue squares) and an unstructured gold film (red circles) with same thickness. Both modulation depth and phase shift for the metasurface show dramatic changes below 11 fs while the unstructured gold film shows almost no changes with pulse duration.*

modulation depth of the metasurface is calculated without any free parameter to be adjusted, see dashed line on Figure 6.10 a). For large pulse durations, the modulation depth approaches the continuous-wave limit of 94%, twice the value of single-beam absorption. It is worth to mention that the minimal absorption is zero in the simulation, and it is a small but finite value in the experiment due to experimental imperfections. Next, we compare the modulation depth of the metasurface sample with that of an unstructured gold film of the same thickness. Figure 6.11 a) shows the pulse duration dependent modulation depth for the plasmonic metasurface and the reference result for the unstructured free standing gold film, both are 60 nm thick. The phase shift, $\Delta\phi_{\gamma\delta}$, between the recorded oscillatory dependencies in channels γ and δ is also plotted in Figure 6.11 b). In addition to the low modulation depth of the plasmonic metasurface film for short pulses and its rapid increase with pulse duration, a large phase shift, $\Delta\phi_{\gamma\delta}$, was measured for low pulse durations which rapidly falls to nearly zero when the pulse duration reaches $\Delta\tau \approx 11$ fs. In contrast, the phase shift, $\Delta\phi_{\gamma\delta}$, measured for the unstructured gold film is about π for all measured pulse durations while the modulation depth steadily increases from nearly 6.5% for short pulses to about 11% for longer pulses.

Weak coherent absorption in unstructured gold films and the large modulation depth for the metasurface sample at its plasmon resonance provide clear evidence of

the crucial role of plasmons for the coherent absorption process. Transferring of photon energy to a plasmon requires about 11 fs which can be seen as the speed limit for our metasurface. The measured 90% modulation depth for 11 fs pulses enables high contrast modulation of light with 90 THz bandwidth, the limit for our structure. In fact, we can go higher than 90 THz by carefully designing the metasurface since the limiting plasmon relaxation rate is proportional to the bandwidth of the absorption peak, based on the Lorentz oscillator model. All-optical modulation with up to 100 THz bandwidth seems to be feasible.

6.3.3 Coherent Image Processing

My contribution to the work discussed in this section is the fabrication of the free-standing metasurface. The experiments reported here have been conducted by Maria Papaioannou.

Coherent control provides a practical solution for dynamic control of the expression of metasurface properties with high spatial resolution. The implementation presented in this section realizes spatial intensity modulation by imaging stationary masks onto the metasurface while providing temporal modulation by controlling the overall phase of one illuminating beam. However, full dynamic control over amplitude and phase can be realized by controlling both illuminating beams with amplitude and phase spatial light modulators. We demonstrate all-optical wavefront control by projecting images onto opposite sides of the free-standing gold metasurface using coherent light. By modulating the relative phase of the two beams, we control the absorption of light, and hence the wavefront, with high spatial resolution. This will be illustrated by performing two-dimensional all-optical Boolean logical operations as well as image processing. The experimental setup is shown by Figure 6.12. Incident light was linearly polarized with the electric field parallel to the symmetry axis of the split ring pattern throughout all experiments. To coherently control the metasurface excitation, we split the output of a 785 nm CW laser along two paths of matched lengths, A and B, that illuminate opposite sides of the nanostructure. Intensity masks are placed in both paths and imaged onto the metasurface to control the spatial intensity distribution on the metasurface. The intensity masks that provide the spatial intensity modulation shown in Figure 6.13 were made by milling a 1.5 mm hole through an aluminium plate. The intensity masks were

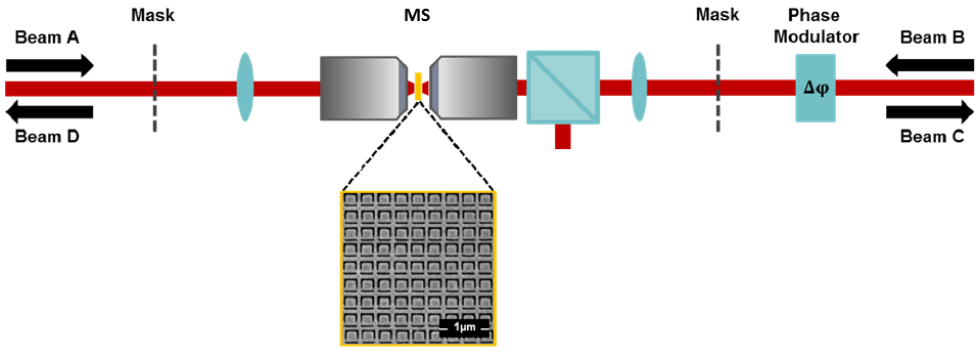

Figure 6.12: ***Two-dimensional all-optical control of light.*** *Schematic of the experimental setup where two-dimensional spatial modulation across coherent beams A and B is provided by masks and temporal modulation is provided by a phase modulator. A CCD camera monitors the system output. Also shown, a SEM image of a fragment of the metasurface (MS).*

then imaged by a lens with 400 mm focal length and a 50x objective onto either side of the metasurface with 100-fold demagnification. One side of the metasurface was imaged onto a CCD camera (Photometrics Evolve512) using a beam splitter and a 200 mm focal length lens.

In order to introduce temporal control, a liquid crystal phase modulator is used to control the relative phase of the illuminating beams, which shifts the standing wave relative to the metasurface. This way, any part of the structure can be illuminated by a single beam (A or B) or by both coherent waves, where the phase modulator allows tuning from constructive to destructive interference at the metasurface position; that is from enhanced to negligible light-matter interaction. We detect the resulting coherent effects by imaging the metasurface onto a CCD camera, detecting output beam C that is formed by transmission of beam A and reflection of beam B. We note that less-than-ideal absorption in our sample (see Figure 6.6 for optical properties) reduces the achievable level of coherent absorption and results in a difference between intensity levels in the output beams [174]. The small difference between experimental transmission and reflection levels is compensated for by adjusting the input intensities.

Figure 6.13 illustrates two-dimensional control of light with light on the free-standing gold metasurface for the simplest possible case of two partially overlapping illuminating beams, A and B (panels (a) and (b)), realized by imaging the intensity profiles imposed by two metallic masks with slightly misaligned circular holes onto opposite sides of the

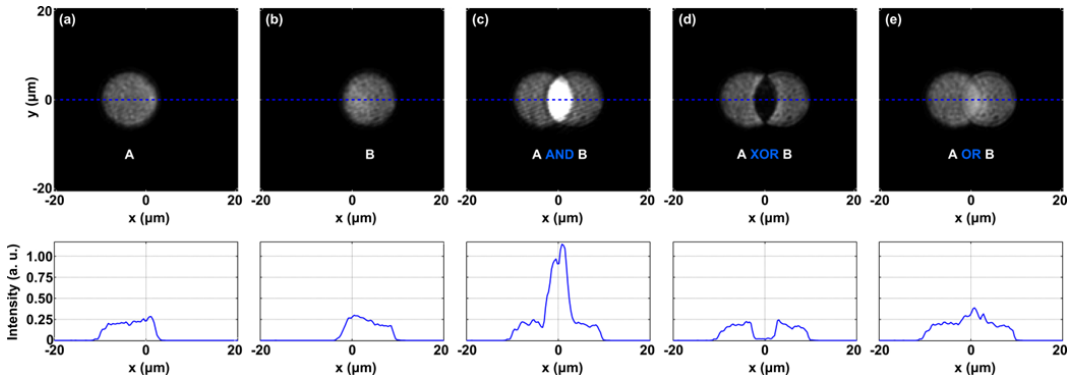

Figure 6.13: ***Coherent logical operations between images:*** *Venn diagrams a) Single beam corresponding to image A, b) single beam corresponding to image B, c) A and B, d) A XOR B and e) A OR B.*

metasurface. In areas of overlapping illuminating beams, the detected intensity depends dramatically on the relative phase difference between the incident waves. Noting that intensities of incoherent beams would simply add up, we find that illumination with a second coherent illuminating beam leads to a range of output intensities from four-fold increase to almost complete suppression. The coherently enhanced output intensity (panel (c)) corresponds to a reduced light-matter interaction and thus reduced absorption at the standing wave's electric node. On the other hand, changing the phase of one illuminating beam by π translates the standing wave, placing the metasurface at an electric anti-node, where almost complete suppression of the detected output intensity occurs as a result of enhanced light-matter interaction and therefore enhanced absorption (panel (d)). Intermediate phases lead to the full range of intermediate intensities (panel (e)).

The approach taken here exploits the interaction of coherent waves at the metasurface to enhance or completely suppress the light-matter interaction and offers control over thin film functionalities with diffraction-limited spatial resolution, ultrafast temporal resolution and high contrast at arbitrarily low intensities. All-optical logical operations (AND, XOR, OR) between two partially overlapping beams (images of an aperture) were demonstrated experimentally. This is a proof-of-principle demonstration of a new technology for two-dimensional control of light with light based on the coherent interaction of optical beams on highly absorbing plasmonic metasurfaces.

6.4 Summary

In this last experimental chapter, fabrication of ultrathin metasurfaces with identical optical properties for opposite directions of illumination enabled several experiments demonstrating active control of light. Based on precise and cutting edge fabrication of asymmetric split ring resonators on an ultrathin free-standing plasmonic membrane it was possible to use coherent control networks to demonstrate several novel concepts and principles.

It was demonstrated experimentally that the coherent absorption process in a thin absorber holds at the single quantum level and that a single photon can be deterministically coupled to a plasmonic mode of a metasurface.

Also, the ultimate speed at which coherent absorption can occur was measured to be 90 THz. This implies that future ultrafast optical signal and data processing solutions may be based on coherent optical networks.

Finally, we demonstrate simultaneous spatial and temporal control over the expression of metasurface absorption by experimentally demonstrating set theory operations between images in a coherent network.

In summary, experiments reported in this chapter have shown femtosecond-scale response times, wavelength-scale spatial resolution, large optical contrast and quantum-level energy requirements for two-dimensional control of light with light. These achievements were facilitated by the high quality of the samples fabricated. Narrow resonances at specific wavelengths, suitable absorption levels and ultrathin thickness of the metasurfaces was crucial for the success of this work.

Chapter 7

Conclusion

7.1 Summary

The goal of this work was to actively control light with metasurfaces and this has been achieved based on a range of physical concepts and fabrication techniques. As a result, this thesis provides solutions for key challenges in the field of reconfigurable photonic metasurfaces; introduces a new magneto-electro-optical effect; merges mechanical and electromagnetic metamaterials; and finally pushes nanofabrication to the limit to produce ultrathin metallic nanomembrane metasurfaces enabling coherent control of light with light. Key achievements in this work include:

- Demonstration of **new and practical** solutions for **large-range tuning** of the optical properties of reconfigurable photonic metasurfaces. Electrothermal tuning delivers optical contrast on the order of 45% and offers sub-millisecond response times. Here, application of electrical currents to the metasurface nanostructure causes resistive heating resulting in actuation due to differential thermal expansion of different materials. Magnetic tuning offers 25% optical contrast without being limited by thermal timescales (hundreds of kHz modulation). Magnetic actuation exploits the Lorentz force on current-carrying reconfigurable parts of the metasurface which is placed in an external magnetic field. Both mechanisms improve on previously reported reconfigurable metasurfaces since high contrast and high operation speeds are achieved in a practical way without cryogenic temperature requirements or vacuum chambers.

- Observation of a **new reciprocal magneto-electro-optical effect**. A large reciprocal magneto-electro-optical effect is observed in an artificial chevron nanowire structure fabricated on an elastic nanomembrane. The Lorentz force drives reversible nanowire actuation on application of a fraction of a volt when the structure is placed in a fraction-of-Tesla magnetic field. The resulting magneto-electro-optical effect does not depend on reversal of the light propagation direction and it manifests itself as transmission changes of the nanowire metamaterial that are proportional to both the external magnetic field and the external electric field (or applied voltage).

- Demonstration of the **first plasmonic micro- and nanoauxetic metasurfaces** that exhibit both a negative Poisson's ratio and resonant optical properties controlled by the metasurface structure. These materials exhibit negative Poisson's ratios between -0.3 and -0.5 under uniaxial tension or compression and pronounced transmission and reflection resonances in the infrared and optical parts of the spectrum.

- Demonstration that **electro-annealing improves the quality factor of optical resonances** in plasmonic metasurfaces.

- **Development of a fabrication technique for free-standing gold metasurfaces of tens of nm thickness**, which enabled the demonstration of coherent control of light with light with (i) single photons, (ii) 11 fs pulses of light and (iii) diffraction-limited spatial resolution.

By demonstrating both novel and practical solutions for active control of metasurfaces, these results do not only add to the rich electromagnetism of metamaterials, but also contribute to bridging the gap between scientific proof-of-principle demonstrations and industrial applications of metamaterials and metasurfaces. Potential applications range from light modulators, single photon detectors and magnetic field sensors to ultrafast all-optical data and image processing.

7.2 Outlook

The experiments reported in this thesis are mainly proof-of-principle demonstrations. Each of them could be developed further. Here, a very brief outlook is given on what is still left to do for each of the directions explored in this thesis.

Electrically and Magnetically Reconfigurable Metasurfaces

Two practical solutions for large-range tuning of reconfigurable photonic metasurfaces were demonstrated here: (i) Electrothermal tuning exploiting local resistive heating and differential thermal expansion to reconfigure the nanostructure and (ii) magnetic modulation exploiting the Lorentz force on current-carrying reconfigurable parts of the metasurface which is placed in an external magnetic field. Further optimization of actuators and optical resonators can allow practical electrothermal or magnetoelectric light modulators and switches. Randomly addressable metasurfaces that redirect, diffract, focus and modulate light on demand can be envisioned.

Magneto-electro-optical Effect in Metamaterials

Electro- and magneto-optical phenomena play key roles in photonic technology enabling light modulators, optical data storage, sensors and numerous spectroscopic techniques. Optical effects, linear and quadratic in external electric and magnetic field are widely known and comprehensively studied. However, optical phenomena that depend on the simultaneous application of external electric and magnetic fields in conventional media are barely detectable and technologically insignificant. The new large and reciprocal magneto-electro-optical effect demonstrated here bring significance to such optical phenomena. Already the effect in the chevron nanowire array can be used for magnetic field sensing applications where availability of the second control parameter (the electric field) could be exploited to engage highly sensitive zero balance phase detection techniques to realize sensitivity at nano-Tesla levels.

Auxetic Metasurfaces

Merging of mechanical and electromagnetic metamaterials provides both a negative Poisson's ratio and resonant optical properties controlled by the metasurface structure.

These new interesting structures can enable reconfigurable metasurfaces which keep their isotropy/anisotropy upon deformation. For this, practical solutions for actuation of auxetic metasurfaces with a Poisson's ratio of approximately -1 will need to be developed.

Coherent Control of Metasurfaces Functionalities

Fabrication of ultrathin free-standing metal metasurfaces with identical properties for illumination of both sides enabled coherent control of absorption of light with light with single photons, 90 THz bandwidth and diffraction-limited resolution. Taking the nanofabrication forward we can target new materials, new layered designs and inclusion of active thin films on the metasurface array. Quantum technologies, imaging and optical computing can greatly benefit from the development of this technology.

Appendix A

Fabrication Methods

This appendix provides more details than section 2.5, such as deposition parameters, fabrication conditions and etching recipes. The appendix consists of 3 parts, relating with the 3 main techniques used during this work, resistive thermal evaporation, focused ion beam milling and reactive ion etching.

A.1 Resistive Thermal Evaporation

In this work, all thin film depositions were performed using a reactive thermal evaporator system (BOC Edwards AUTO306) with tungsten boats where gold pellets are added to be evaporated. Substrates (silicon nitride membrane + silicon frame) are taped (Kapton tape) onto the substrate holder and placed inside the chamber. Rotation of the substrate holder is crucial to avoid shadow effects. All depositions use the same parameters, which yield 50 to 60 nm thick gold films with a good quality plasmonic response.

The parameters used for resistive thermal evaporation are:

- Evaporation rate - 0.10 nm/s
- Base pressure - 2-4 $\times$ 10^{-6} mbar
- Evaporation current - 2.6 A
- Substrate holder rotation - Yes
- Substrate heating - Off (except where mentioned)

- Material evaporated - Gold pellets (99.99%)

Surface and microstructure of typical gold thin films are shown in subsection 2.5.1 Figure 2.9 and Figure 2.10. The possibility to heat up the substrate holder through a radiation source was employed once. In this way we increased the crystallinity of the gold films deposited for further electro-annealing through minimization of losses in the gold film. Thermal resistive evaporation was used in all reported samples and the only difference between the gold films obtained was their final thickness, varying between 50nm and 60nm.

A.2 Focused Ion Beam Milling

Focused ion beam (FEI Helios 600 NanoLab) milling was the technique used for structuring of the metasurfaces and metamaterials reported in this thesis. In order to achieve the high precision and high resolution that is required for metamaterials operating at optical wavelengths, a long process of parameter optimization was performed. Depending on the unit cell size, substrate and thickness of the plasmonic layer, the fabrication parameters can vary substantially. The important parameters for the fabrication of each sample used in this work are listed below.

Electrically and Magnetically Reconfigurable Metasurfaces / Magneto-electro-optical effect Metamaterial:

- Magnification - x4000
- Center to center distance - 5.88nm
- Line spacing - 5.88nm
- Ion beam current - 9.9 pA
- Multipass type - 2 times reverse
- Area Dosage (Red) - 13.65 nC/cm
- Area Dosage (Yellow) - 8 nC/cm
- Area Dosage (Blue) - 3 nC/cm

- Area Dosage (Green) - 5.6 nC/cm

NPGS file used:

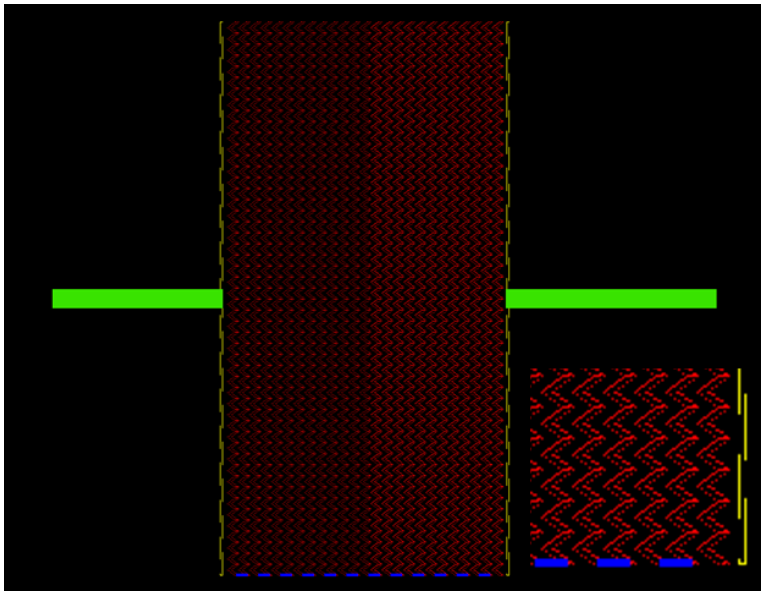

Figure A.1: ***NPGS design for the electrically and magnetically reconfigurable metasurface and the magneto-electro-optical effect metamaterial samples.*** *Designed using computer software (DesignCAD) the sample was divided in 4 layers. Red layer for the fabrication of the metasurface unit cells cutting through both silicon nitride and gold layers. Yellow layer corresponding to the left and right cuts through to release the metasurface. Blue layer in order to remove only the gold layer providing electrical isolation for every second bridge of the metasurface. Finally, the green layer in order to later insulate both sides of the metasurface, also this layer will only remove the gold layer. The inset shows a zoom up of several unit cells, chevron cut and isolating cuts. Fabrication order of layers as listed above.*

Auxetic IR Metasurfaces (Honeycomb):

- Magnification - x2000
- Center to center distance - 7.06 nm
- Line spacing - 20.2 nm
- Ion beam current - 70 pA
- Multipass type - 2 times reverse
- Area Dosage (Red) - 15.25 nC/cm
- Area Dosage (Yellow) - 14 nC/cm

- Area Dosage (Blue) - 15 nC/cm
- Area Dosage (Green) - 15.25 nC/cm

NPGS file used for the auxetic IR metasurfaces (wide beams):

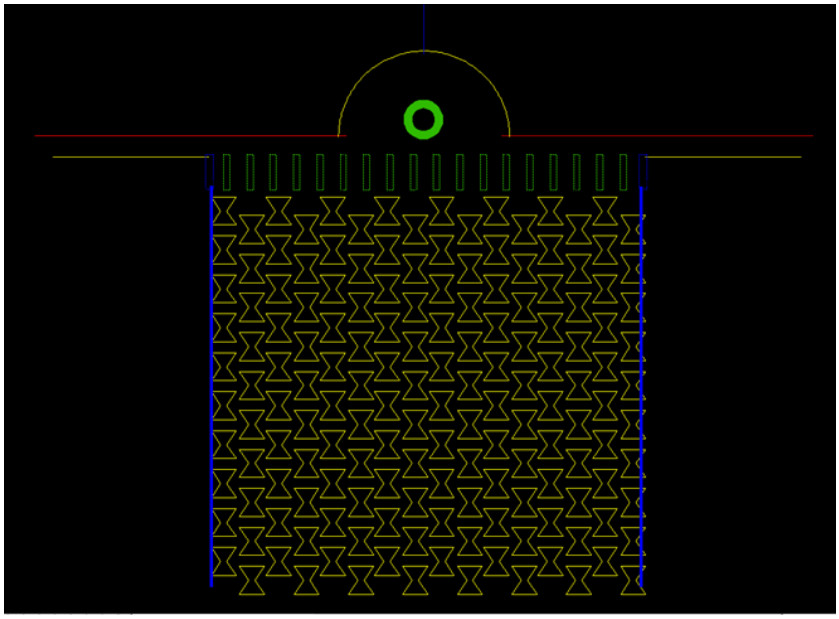

Figure A.2: ***NPGS design for the auxetic IR metasurfaces (wide beams).*** *Designed using computer software (DesignCAD) the sample was divided in 4 layers to better control patterning, however in this case, all 4 layers cut through both silicon nitride and gold layers. The hole corresponding to the green circle is used for the micromanipulator. Fabrication order of layers as listed above.*

Auxetic Optical Metasurfaces (Honeycomb):

- Magnification - x4500
- Center to center distance - 7.06 nm
- Line spacing - 20.2 nm
- Ion beam current - 9 pA
- Multipass type - 2 times reverse
- Area Dosage (Yellow) - 13.25 nC/cm
- Area Dosage (Blue) - 7.40 nC/cm

NPGS file used for the honeycomb optical auxetic metasurface:

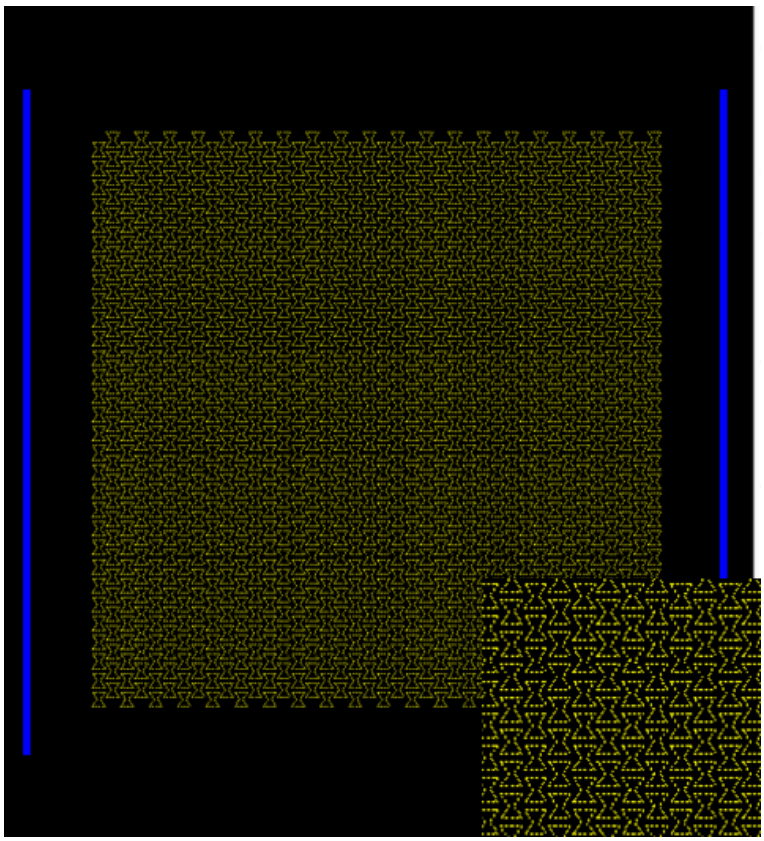

Figure A.3: ***NPGS design for the honeycomb optical metasurface sample.*** *Designed using computer software (DesignCAD) the sample was divided in 2 layers. Yellow layer cutting through both layers and providing the structured metasurface. Blue layer cutting through only gold for electrical connections realized later on. The inset shows a zoom up of several honeycomb unit cells. Fabrication order of layers as listed above.*

Auxetic Optical Metasurfaces (Star):

- Magnification - x4500
- Center to center distance - 7.06 nm
- Line spacing - 20.2 nm
- Ion beam current - 9 pA
- Multipass type - 2 times reverse
- Area Dosage (Yellow) - 11.75 nC/cm
- Area Dosage (Red) - 13.4 nC/cm

- Area Dosage (Blue) - 7.40 nC/cm

NPGS file used for the honeycomb optical auxetic metasurface:

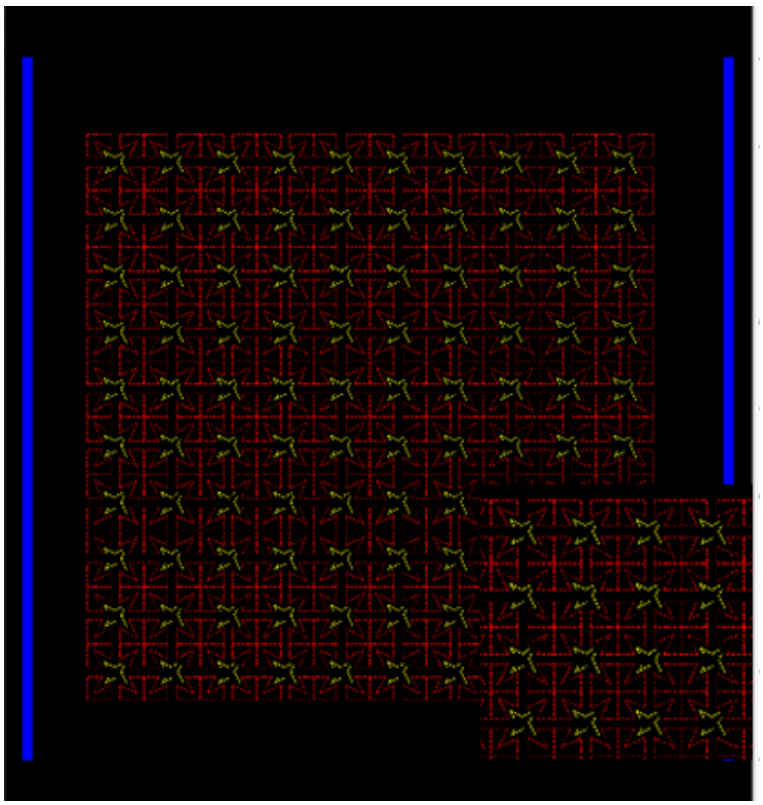

Figure A.4: ***NPGS design for the star-shaped optical metasurface sample.*** *Designed using computer software (DesignCAD) the sample was divided in 3 layers. Yellow layer cutting thought both layers and providing the central part of the star, part of the unit cell. Red layer defining the star shap of the unit cell. Blue layer cutting thought only gold for electrical connections realized later on. The inset shows a zoom up of several star-shape unit cells. Fabrication order of layers as listed above but unit cells were fabricated sequentially, meaning yellow and red layer followed by yellow and red layer.*

Coherent Control Metasurfaces:

- Magnification - x1500 (100μm $\times$ 100μm arrays), x3000 (50μm $\times$ 50μm arrays)
- Center to center distance - 3.14 nm, 4.71 nm
- Line spacing - 20.40 nm, 24.32 nm
- Ion beam current - 1.5 pA, 1.3 pA
- Multipass type - OFF
- Line Dosage (Yellow)- 8.75 nC/cm, 8 nC/cm

In this case, due to use of the smallest possible ion beam current a platinum cross is deposited on the surface to facilitate the focusing and stigma control of the ion beam. Also, due to characteristics of the designed CAD file, a line dosage is chosen instead of an area dosage.

NPGS file used for a typical coherent control metasurface:

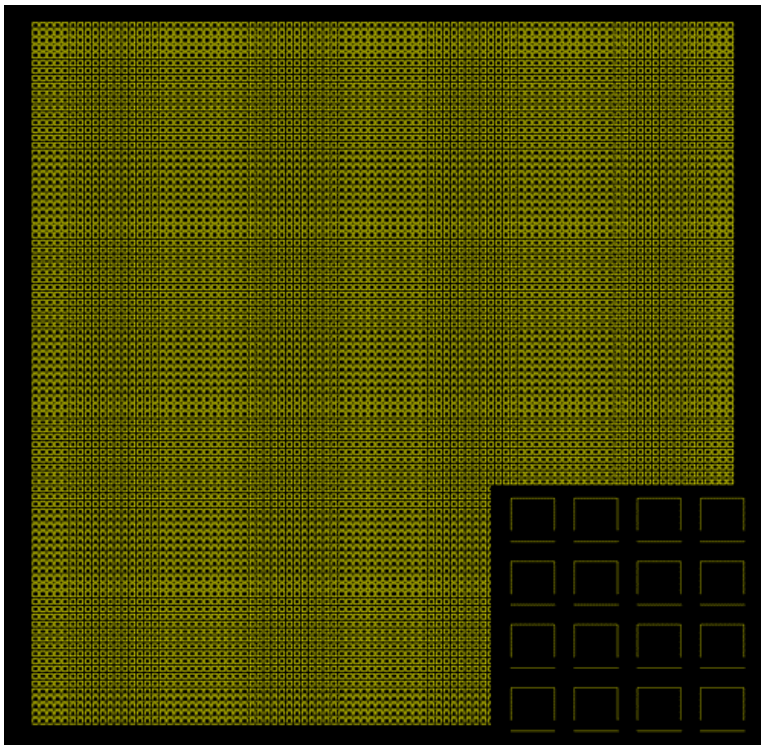

Figure A.5: ***NPGS design for coherent control metasurfaces.*** *Designed using computer software (DesignCAD) the sample has only 1 layer, which consists of two lines that make up the unit cell of the metasurface. The inset shows a zoom up of several unit cells, C-shape is fabricated followed by the horizontal bottom bar.*

A.3 Reactive Ion Etching

Reactive ion etching (Plasma Lab 80 Plus, Oxford Instruments) was only used for the last Chapter of this thesis, however, it was one of the crucial tools that allow the fabrication of high quality metasurfaces of deeply sub-wavelength thickness with symmetric optical properties for illumination of both sides. Preparation of samples for the etching process is given in the main text and detailed with pictures. Here, the parameters used for the etching process are listed.

Reactive Ion Etching of 50 nm of silicon nitride membrane with 50/60 nm of evap-

orated gold:

- Time -10 minutes
- RF power - 80 W
- Chamber pressure - 50 mT
- Base pressure - 7.5×10^{-6} mbar
- Gas flux (CHF_3) - 2 sccm
- Gas flux (Ar) - 10 sccm
- Process temperature - 20°C

Appendix B

Publications

B.1 Journal Publications

- J. Valente, J. Y. Ou, E. Plum, J. Youngs, N. I. Zheludev - "Reconfiguring Photonic Metamaterials with Currents and Magnetic Fields", Appl. Phys. Lett. 106, 111905 (2015)
- J. Valente, J. Y. Ou, E. Plum, J. Youngs, N. I. Zheludev - "A Magneto-electro-optical effect in plasmonic nanowire material", Nat. Commun. 6, 7021 (2015)
- T. Roger, S. Vezzoli, E. Bolduc, J. Valente,J. J. F. Heitz, J. Jeffers, J. Leach, C. Couteau, C. Soci, N. I. Zheludev, D. Faccio - "Coherent Perfect Absorption in the Single Photon Regime", Nat. Commun. 6, 7031 (2015)
- M. Papaioannou, E. Plum, J. Valente, E. T. F. Rogers, N. I. Zheludev - "Two-dimensional control of light with light on metasurfaces", Light Sci. Appl. 5, e16070 (2016)
- J. Valente, E. Plum, J. Youngs, N. I. Zheludev - "Nano and Micro-Auxetic Plasmonic Materials", Adv. Mater., doi:10.1002/adma.201600088 (2016)

B.1.1 Submitted

- C. Altuzarra, S. Vezzoli, J. Valente, W. Gao, C. Soci, D. Faccio, C. Couteau, N. I. Zheludev - "Nonlocal Control of Dissipation with Entangled Photons", Science Advances. *under review*

B.2 Conference Main Contributions

- (oral) “Auxetic nanomechanical metamaterials” - J. Valente, E. Plum, and N. I. Zheludev - Materials Research Society MRS 2015 Fall Meeting and Exhibit, Boston, MA, USA, 29 Nov - 4 Dec 2015
- (3MT) “Active control of light with metasurfaces” - J. Valente, E. Plum, M. Papaioannou, P. Cencillo-Abad, V. Nalla, C. Altuzarra, S. Vezzoli, I. J. Youngs, and N. I. Zheludev - Defence & Security Doctoral Symposium, Cranfield, UK, 22 - 26 Nov 2015
- (artwork) “Metamaterial x Metamaterial = MM2” - J. Valente, E. Plum, I. J. Youngs and N. I. Zheludev - Defence & Security Doctoral Symposium, Cranfield, UK, 22 - 26 Nov 2015
- (keynote) “ Metamaterials: a playground for light” - J. Valente, and N. I. Zheludev - STEM TEAtime - Workshop on Light, Southampton, UK, 19 Mar 2015
- (oral) “Metamaterial NEMS: giant optical nonlinearity and magnetoelectric effect” - J. Valente, J. Y. Ou, E. Plum, K. F. MacDonald, and N. I. Zheludev - OMN2014 - International Conference on Optical MEMS and Nanophotonics, Glasgow, Scotland, 17 - 21 Aug 2014
- (oral) “Lorentz force metamaterial with giant optical magnetoelectric response” - J. Valente, J. Y. Ou, E. Plum, I. Youngs, and N. I. Zheludev - CLEO:2014, San Jose, CA, USA, 8 - 13 Jun 2014
- (oral) “Reconfigurable photonics metamaterials: nanoscale forces and giant magnetoelectric effect” - J. Valente, E. Plum, J. Y. Ou, and N. I. Zheludev - DSTL Novel Electronic Materials PhD Theme Event, London, 17 Dec 2013
- (poster) “ Reconfigurable photonics metamaterial: observation of a giant magnetoelectric effect” - J. Valente, E. Plum, J. Y. Ou, and N. I. Zheludev - DSTL Novel Electronic Materials PhD Theme Event, London, 17 Dec 2013
- (oral) “Reconfigurable metamaterials controlled by Lorentz, Ampere and Coulomb forces: towards GHz bandwidth” - J. Valente, E. Plum, J. Y. Ou, and N. I. Zheludev - CLEO/Europe - IQEC 2013, Munich, Germany, 12 - 16 May 2013

- (invited) “Nanomechanical control of metamaterial optical properties” - E. Plum, J. Y. Ou, J. Valente, J. Zhang and N. I. Zheludev IPS Meeting 2013, Singapore, 4 - 6 Mar 2013

- (poster) “Reconfiguring photonic metamaterials with electrical currents” - J. Valente, E. Plum, N. I. Zheludev - National PhD Scheme Conference 2013, Oxford, UK, 27 Feb 2013

- (invited) “Reconfiguring photonic metamaterials with electromagnetic forces” - E. Plum, J. Y. Ou, J. Valente, J. Zhang, and N. I. Zheludev - Nanometa 2013, Seefeld, Austria, 3 - 6 Jan 2013

- (poster) “Tunable plasmonic luminescence in reconfigurable metamaterials” - G. Adamo, W. T. Chen, E. Plum, J. K. So, J. Valente, D. P. Tsai, and N. Zheludev - Nanometa 2013, Seefeld, Austria, 3 - 6 Jan 2013

B.2.1 Other Conference Contributions

- (oral)“Shape memory plasmonic metamaterial” - M. Tsuruta, J. Valente, B. Gholipour, K. F. MacDonald, E. Plum, and N. I. Zheludev Metamaterials 2016, Crete, Greece, 17 - 22 Sep 2016

- (oral)“Metasystems for all-optical recognition and processing of images and data” - M. Papaioannou, E. Plum, E. T. F. Rogers, J. Valente, and N. I. Zheludev Metamaterials 2016, Crete, Greece, 17 - 22 Sep 2016

- (oral) “Shape memory photonic metamaterial” - M. Tsuruta, J. Valente, B. Gholipour, K. F. MacDonald, E. Plum, and N. I. Zheludev, CLEO:2016, San Jose, CA, USA, 5-10 Jun 2016

- (poster) “All-optical image recognition and processing with plasmonic metasurfaces” - M. Papaioannou, E. Plum, E. T. F. Rogers, J. Valente, B. Gholipour, and N. I. Zheludev, CLEO:2016, San Jose, CA, USA, 5-10 Jun 2016

- (poster) “*Remote control* of coherent light absorption with entangled photons” - C. M. Altuzarra, S. Vezzoli, J. Valente. C. Soci, D. Faccio, C. Couteau, and N. I. Zheludev CLEO 2016, San Jose, CA, USA, 5 - 10 June 2016

- (poster) “Shape memory metamaterial” - M. Tsuruta, J. Valente, B. Gholipour, K. F. MacDonald, E. Plum, and N. I. Zheludev, New horizons in nanophotonics, Chicheley, UK, 23-24 May 2016

- (poster) “All-optical image recognition and processing with plasmonic metasurfaces” - M. Papaioannou, E. Plum, E. T. F. Rogers, J. Valente, Nikolay I. Zheludev, New horizons in nanophotonics, Chicheley, UK, 23-24 May 2016

- (invited) “Reconfigurable nanomembrane metadevices” - E. Plum, J. Valente, J. Y. Ou, P. Cencillo-Abad, A. Karvounis, K. F. MacDonald, and N. I. Zheludev, 9th International Conference on Nanophotonics (ICNP 2016), Taipei, Taiwan, 21 - 25 Mar 2016

- (poster) “Quantum coherent absorpion of plasmons with entangled photons” - C. Altuzarra, S. Vezzoli, J. Valente, C. Soci, D. Faccio, C. Couteau and N. I. Zheludev, Nanophotonics in Asia, Osaka, Japan, 10 - 11 Dec 2015

- (oral) “Coherent polarization spectroscopy of metamaterials” - K. Hiramatsu, E. Plum, J. Valente, K. F. MacDonald, and N. I. Zheludev - Metamaterials 2015, Oxford, UK, 7 - 12 Sep 2015

- (oral) “Coherent image processing with plasmonic metasurfaces” - M. Papaioannou, E. Plum, J. Valente, E. T. F. Rogers, and N. I. Zheludev - Metamaterials 2015, Oxford, UK, 7 - 12 Sep 2015

- (oral) “100 THz Broadband and single photon optical switching with a plasmonic metamaterial” - V. Nalla, S. Vezzoli, C. M. X. Altuzarra, E. Bolduc, J. Valente, J. J. F. Heitz, J. Jeffers, J. Leach, T. Roger, C. Couteau, S. Handong, C. Soci, D. Faccio, and N. I. Zheludev - Metamaterials 2015, Oxford, UK, 7 - 12 Sep 2015

- (oral) “Random access photonic metamaterials” - P. Cencillo-Abad, J. Y. Ou, J. Valente, E. Plum, and N. I. Zheludev - Metamaterials 2015, Oxford, UK, 7 - 12 Sep 2015

- (invited) “Nanostructured photonic metamaterials reconfigurable with light, nanomechanical and electromagnetic forces” - J. Y. Ou, J. Valente, A. Karvounis, W. Wu,

E. Plum, K. F. MacDonald, and N. I. Zheludev - SPIE Optics & Photonics 2015, San Diego, California, USA, 9 - 13 Aug 2015

- (oral) "100 THz broadband optical switching with plasmonic metamaterial" - V. Nalla, S. Vezzoli, J. Valente, C. Soci, H. Sun, and N. I. Zheludev - ICMAT2015, Singapore, 28 Jun - 3 Jul 2015

- (poster) " Coherent perfect absorption of a single photon in a metamaterial" - S. Vezzoli, C. Altuzarra, T. Roger, J. Valente, E. Bolduc, J. Heitz, J. Leach, J. Jeffers, C. Soci, C. Couteau, N. I. Zheludev, and D. Faccio - ICMAT2015, Singapore, 28 Jun - 3 Jul 2015

- (oral) "Dynamic mode multiplexing with plasmonic metasurfaces" - M. Papaioannou, E. Plum, J. Valente, E. T. F. Rogers, and N. I. Zheludev - CLEO/Europe-EQEC 2015, Munich, Germany 21 - 25 Jun 2015

- (oral) "Reconfigurable gradient metasurfaces with random access" - P. Cencillo-Abad, J.-Y. Ou, J. Valente, E. Plum, and N. I. Zheludev - CLEO/Europe-EQEC 2015, Munich, Germany 21 - 25 Jun 2015

- (oral) "Coherent spectroscopy of optical activity" - K. Hiramatsu, E. Plum, J. Valente, K. F. MacDonald, and N. I. Zheludev - CLEO/Europe-EQEC 2015, Munich, Germany 21 - 25 Jun 2015

- (oral) "100 THz optical switching with plasmonic metamaterial" - V. Nalla, S. Vezzoli, J. Valente, S. Handong, and N. I. Zheludev - CLEO/Europe-EQEC 2015, Munich, Germany 21 - 25 Jun 2015

- (oral) "100 THz bandwidth plasmonic metamaterial switch" - V. Nalla, J. Valente, S. Vezzoli , C. Soci, H. Sun, and N. I. Zheludev - IPS Meeting, Singapore, 4 - 6 Mar 2015

- (poster) "Metamaterial coherent plasmonic absorption with a single photon" - C. Altuzarra, S. Vezzoli, T. Roger, E. Bolduc, J. Valente, J. Heitz, J. Jeffers, J. Leach, C. Couteau, C. Soci, N. I. Zheludev, and D. Faccio - IPS Meeting, Singapore, 4 - 6 Mar 2015

- (oral) “Metamaterial coherent plasmonic absorption with a single photon” - C. Altuzarra, S. Vezzoli, T. Roger, E. Bolduc, J. Valente, J. Heitz, J. Jeffers, J. Leach, C. Couteau, C. Soci, N. I. Zheludev, D. Faccio, and T. Roger - Nanometa 2015, Seefeld, Austria, 5 - 8 Jan 2015

- (poster) “ Randomly addressable reconfigurable photonic metamaterials” - P. Cencillo-Abad, J. Y. Ou, J. Valente, E. Plum, N. I. Zheludev - Nanometa 2015, Seefeld, Austria, 5 - 8 Jan 2015

- (poster) “100 THz bandwidth all-optical switching using coherent absorption in plasmonic metamaterials” - V. Nalla, J. Valente, H. Sun, N. I. Zheludev - Nanometa 2015, Seefeld, Austria, 5 - 8 Jan 2015

- (invited) “ Giant nonlinearities in plasmonic and dielectric reconfigurable metamaterials” - N. I. Zheludev, K. F. MacDonald, E. Plum, J.-Y. Ou, J. Valente, A. Karvounis, W. Wu - 2014 MRS Fall Meeting, Boston, MA, USA, 30 Nov - 5 Dec 2014

- (invited) “ Giant optical nonlinearity and magnetoelectric effect in reconfigurable plasmonic metamaterials” - E. Plum, J. Valente, J. Y. Ou, K. F. MacDonald, and N. I. Zheludev - Metamaterials’2014, Copenhagen, Denmark, 25 - 30 Aug 2014

- (invited) “ Nanomechanical metamaterial light modulators” - E. Plum, J. Y. Ou, J. Valente, P. Cencillo-Abad, and N. I. Zheludev - META’14, Singapore, 20 - 23 May 2014

- (keynote) “ Driving reconfigurable photonic metamaterials with light and electrical signals: exploiting forces and fields at the nanoscale ” - N. I. Zheludev, E. Plum, K. F. MacDonald, J. Y. Ou, J. Zhang, J. Valente, W. M. Zhu, and A. Q. Liu - Metamaterials’ 2013, Bordeaux, France, 16 - 19 Sep 2013

- (invited) “ Reconfigurable photonic metamaterials driven by Coulomb, Lorentz and optical forces” - E. Plum, J. Y. Ou, J. Valente, and N. I. Zheludev - International Conference on Nanomaterials 2013 (ICN 2013), London, Ontario, Canada, 12 - 16 Aug 2013

- (invited) “Reconfiguring photonic metamaterials” - E. Plum, J. Y. Ou, J. Valente, J. Zhang, and N. I. Zheludev - Sino-UK Workshop on Nanophotonics and Metamaterials, Beijing, China, 7 - 8 Dec 2012

B.2.2 Outreach and Workshops

- (Workshop) “Workshop Education, Training and Skills: Connecting students and employers the case of electronics.” - European Comission *Eureka*, Brussels, 13 Oct 2015
- (Science Festival) “ Cheltenham Science Festival” - EPSRC event, Cheltenham, UK, 7 - 9 Jun 2013
- (Outreach) “The Big Bang Science Fair” - London, UK, 14 - 17 Mar 2013
- (Summer School) “International School of Quantum Electronics - 52nd Course:Advances on Nanophotonics IV” - Ettore Majorana Foundation and Centre for Scientific Culture, Erice, Sicily, 17 - 29 Jul 2012
- (Workshop) “Metamaterials Industry Open Day” - Southampton, UK, 13 Sept 2012

References

[1] N. I. Zheludev and Y. S. Kivshar. "From metamaterials to metadevices". *Nature Materials*, 11(11), 2012.

[2] D. R. Smith, W. J. Padilla, D. C. Vier, S. C. Nemat-Nasser, and S. Schultz. "Composite Medium with Simultaneously Negative Permeability and Permittivity". *Physical Review Letters*, 84(18), 2000.

[3] R. A. Shelby, D. R. Smith, and S. Schultz. "Experimental verification of a negative index of refraction". *Science (New York, N.Y.)*, 292(5514), 2001.

[4] N. Kida, Y. Kaneko, J. P. He, M. Matsubara, H. Sato, T. Arima, H. Akoh, and Y. Tokura. "Enhanced optical magnetoelectric effect in a patterned polar ferrimagnet". *Physical Review Letters*, 96(16), 2006.

[5] X. Fang, M. L. Tseng, J. Y. Ou, K. F. Macdonald, D. P. Tsai, and Ni. I. Zheludev. "Ultrafast all-optical switching via coherent modulation of metamaterial absorption". *Applied Physics Letters*, 104(14):141102, 2014.

[6] V. A. Fedotov, P. L. Mladyonov, S. L. Prosvirnin, A. V. Rogacheva, Y. Chen, and N. I. Zheludev. "Asymmetric propagation of electromagnetic waves through a planar chiral structure". *Physical Review Letters*, 97(16), 2006.

[7] V. V. Khardikov, E. O. Iarko, and S. L. Prosvirnin. "Trapping of light by metal arrays". *Journal of Optics*, 12(4), 2010.

[8] A.S. Schwanecke, V.A. Fedotov, V.V. Khardikov, S.L. Prosvirnin, Y. Chen, and N.I. Zheludev. "Optical magnetic mirrors". *Journal of Optics A: Pure and Applied Optics*, 9(1), 2007.

[9] U. Leonhardt. "Optical Conformal Mapping". *Science (New York, N.Y.)*, 312(5781), 2006.

[10] J. C. Bose. "On the selective conductivity exhibited by some polarising substances". *Royal Proceedings Society*, 60(1), 1896.

[11] J.C. Bose. "On the Rotation of Plane of Polarisation of Electric Waves by a Twisted Structure". *Proceedings of the Royal Society of London (1854-1905)*, 63(1), 1898.

[12] R. H. Ott, R. G. Kouyoumijian, and L. Peters Jr. "Scattering by a two-dimensional periodic array of narrow plates". *Radio Science*, 2, 1967.

[13] C.C. Chen. "Scattering by a two-dimensional periodic array of conducting plates". *IEEE Transactions on Antennas and Propagation*, 18(5), 1970.

[14] A. B. Munk. "Reflection Properties o f Periodic Surfaces o f Loaded Dipoles". *IEEE Transactions on Antennas and Propagation*, 19(5), 1971.

[15] J. Hunag, T. K. Wu, and S. W. Lee. "Tri-band frequency selective surface with circular ring elements". *IEEE Transactions on Antennas and Propagation*, 42(2), 1994.

[16] R. Ulrich. "Far-infrared properties of metallic mesh and its complementary structure". *Infrared Physics*, 7, 1967.

[17] V. P. Tomaselli, D. C. Edewaard, P. Gillan, and K. D. Möller. "Far-infrared bandpass filters from cross-shaped grids.". *Applied optics*, 20(8), 1981.

[18] J. A. Bossard, D. H. Werner, T. S. Mayer, J. A. Smith, Y. U. Tang, R. P. Drupp, and L. Li. "The design and fabrication of planar multiband metallodielectric frequency selective surfaces for infrared applications". *IEEE Transactions on Antennas and Propagation*, 54(4), 2006.

[19] C. Wenshan and V. Shalaev. *Optical Metamaterials: Fundamentals and Aplications*, volume 330. Springer, 2010.

[20] N. Yu, P. Genevet, M.A Kats, F. Aieta, J.P. Tetienne, F. Capasso, and Z. Gaburro. "Light Propagation with Phase Discontinuities: Generalized Laws of Reflection and Refraction". *Science (New York, N.Y.)*, 334(10), 2011.

[21] Constantine Balanis. *Advanced Engineering Electromagnetics*. John Wiley and Sons, Arizona, 1989.

[22] J. D. Jackson. *Classical Electrodynamics*, volume 67. John Wiley and Sons, Inc., 1999.

[23] J. Petschulat, C. Menzel, A. Chipouline, C. Rockstuhl, A. Tünnermann, F. Lederer, and T. Pertsch. "Multipole approach to metamaterials". *Physical Review A*, 78(4):1–9, 2008.

[24] David J. Cho, Feng Wang, Xiang Zhang, and Y. Ron Shen. "Contribution of the electric quadrupole resonance in optical metamaterials". *Physical Review B - Condensed Matter and Materials Physics*, 78(12):1–4, 2008.

[25] Na Liu and Harald Giessen. "Coupling effects in optical metamaterials". *Angewandte Chemie - International Edition*, 49(51):9838–9852, 2010.

[26] I.V. Shadrivov, A. B. Kozyrev, D.W. Van Der Weide, and Y.S. Kivshar. "Tunable transmission and harmonic generation in nonlinear metamaterials". *Applied Physics Letters*, 93(16), 2008.

[27] I.V. Shadrivov, P.V. Kapitanova, S. I. Maslovski, and Y.S. Kivshar. "Metamaterials controlled with light". *Physical Review Letters*, 109(8), 2012.

[28] V. Savinov, a. Tsiatmas, a. R. Buckingham, V. a. Fedotov, P. a. J. de Groot, and N. I. Zheludev. "Flux Exclusion Superconducting Quantum Metamaterial: Towards Quantum-level Switching". *Scientific Reports*, 2:2–6, 2012.

[29] A. E. Nikolaenko, F. De Angelis, S. A. Boden, N. Papasimakis, P. Ashburn, E. Di Fabrizio, and N. I. Zheludev. "Carbon nanotubes in a photonic metamaterial". *Physical Review Letters*, 104(15), 2010.

[30] Z. L. Sámson, K. F. MacDonald, F. De Angelis, B. Gholipour, K. Knight, C. C. Huang, E. Di Fabrizio, D. W. Hewak, and N. I. Zheludev. "Metamaterial electro-optic switch of nanoscale thickness". *Applied Physics Letters*, 96(14), 2010.

[31] M. Ricci, N. Orloff, and S. M. Anlage. "Superconducting metamaterials". *Applied Physics Letters*, 87(3), 2005.

[32] V. Savinov, V. A. Fedotov, S. M. Anlage, P. A. J. De Groot, and N. I. Zheludev. "Modulating Sub-THz radiation with current in superconducting metamaterial". *Physical Review Letters*, 109(24), 2012.

[33] K. M. Dani, Z. Ku, P.C. Upadhya, R. P. Prasankumar, S. R. J. Brueck, and A. J. Taylor. "Subpicosecond optical switching with a negative index metamaterial". *Nano Letters*, 9(10), 2009.

[34] G. A. Wurtz, R. Pollard, W. Hendren, G. P. Wiederrecht, D. J. Gosztola, V. A. Podolskiy, and A.V. Zayats. "Designed ultrafast optical nonlinearity in a plasmonic nanorod metamaterial enhanced by nonlocality.". *Nature nanotechnology*, 6(2), 2011.

[35] M. Ren, B. Jia, J.Y. Ou, E. Plum, J. Zhang, K.F. MacDonald, A. E. Nikolaenko, J. Xu, M. Gu, and N.I. Zheludev. "Nanostructured plasmonic medium for terahertz bandwidth all-optical switching". *Advanced Materials*, 23(46), 2011.

[36] T. Driscoll, H.T. Kim, B.G. Chae, B.J. Kim, Y.W. Lee, N. Jokerst, S. Palit, D. R. Smith, M. Di Ventra, and D. N. Basov. "Memory metamaterials.". *Science (New York, N.Y.)*, 325(5947), 2009.

[37] M. J. Dicken, K. Aydin, I. M. Pryce, L. A. Sweatlock, E. M. Boyd, S. Walavalkar, J. Ma, and H. A. Atwater. "Frequency tunable near-infrared metamaterials based on VO2 phase transition.". *Optics express*, 17(20), 2009.

[38] I. C. Khoo, D. H. Werner, X. Liang, and A. Diaz. "Nanosphere dispersed liquid crystals for tunable negative zero positive index of refraction in the optical and terahertz regimes". *Optics Letters*, 31(17), 2006.

[39] Q. Zhao, L. Kang, B. Du, B. Li, J. Zhou, H. Tang, X. Liang, and B. Zhang. "Electrically tunable negative permeability metamaterials based on nematic liquid crystals". *Applied Physics Letters*, 90(1), 2007.

[40] D.H. Werner, D.H. Kwon, I.C. Khoo, A. V. Kildishev, and V. M. Shalaev. "Liquid crystal clad near-infrared metamaterials with tunable negative-zero-positive refractive indices.". *Optics express*, 15(6), 2007.

[41] A. Minovich, J. Farnell, D. N. Neshev, I. McKerracher, F. Karouta, J. Tian, D.A. Powell, I.V. Shadrivov, H. Hoe Tan, C. Jagadish, and Y.S. Kivshar. "Liquid crystal based nonlinear fishnet metamaterials". *Applied Physics Letters*, 100(12), 2012.

[42] O. Buchnev, J. Y. Ou, M. Kaczmarek, N. I. Zheludev, and V .A. Fedotov. "Electro-optical control in a plasmonic metamaterial hybridised with a liquid-crystal cell.". *Optics express*, 21(2), 2013.

[43] H. Tao, A. C. Strikwerda, K. Fan, W. J. Padilla, X. Zhang, and R. D. Averitt. "Reconfigurable terahertz metamaterials". *Physical Review Letters*, 103(14), 2009.

[44] Y.H. Fu, A.Q. Liu, W.M. Zhu, X. M. Zhang, D. P. Tsai, J.B. Zhang, T. Mei, Ji.F. Tao, H.C. Guo, X.H. Zhang, J. H. Teng, N.I. Zheludev, G. Q. Lo, and D.L. Kwong. "A micromachined reconfigurable metamaterial via reconfiguration of asymmetric split-ring resonators". *Advanced Functional Materials*, 21(18), 2011.

[45] B. Ozbey and O. Aktas. "Continuously tunable terahertz metamaterial employing magnetically actuated cantilevers.". *Optics express*, 19(7), 2011.

[46] W. M. Zhu, A. Q. Liu, T. Bourouina, D. P. Tsai, J. H. Teng, X. H. Zhang, G. Q. Lo, D. L. Kwong, and N. I. Zheludev. "Microelectromechanical Maltese-cross metamaterial with tunable terahertz anisotropy.". *Nature communications*, 3(12), 2012.

[47] I. M. Pryce, K. Aydin, Y.A. Kelaita, R. M. Briggs, and H. A. Atwater. "Highly strained compliant optical metamaterials with large frequency tunability". *Nano Letters*, 10(10), 2010.

[48] F. Huang and J.J. Baumberg. "Actively tuned plasmons on elastomerically driven Au nanoparticle dimers". *Nano Letters*, 10(5), 2010.

[49] S. Aksu, M. Huang, A. Artar, A. A. Yanik, S. Selvarasah, M.R. Dokmeci, and H. Altug. "Flexible plasmonics on unconventional and nonplanar substrates". *Advanced Materials*, 23(38), 2011.

[50] J. Zhong, Y. Huang, G. Wen, H. Sun, and W. Zhu. "The design and applications of tunable metamaterials". *Procedia Engineering*, 29, 2012.

[51] A. Q. Liu, W. M. Zhu, D. P. Tsai, and N. I. Zheludev. "Micromachined tunable metamaterials: a review". *Journal of Optics*, 14(11), 2012.

[52] V. A. Fedotov, P. L. Mladyonov, S. L. Prosvirnin, and N. I. Zheludev. "Planar electromagnetic metamaterial with a fish scale structure". *Physical Review E - Statistical, Nonlinear, and Soft Matter Physics*, 72(5), 2005.

[53] X.G. Peralta, E. I. Smirnova, A.K. Azad, H.T. Chen, A. J. Taylor, I. Brener, and J.F. O'Hara. "Metamaterials for THz polarimetric devices.". *Optics express*, 17(2), 2009.

[54] E. Plum, V. A. Fedotov, and N. I. Zheludev. "Optical activity in extrinsically chiral metamaterial". *Applied Physics Letters*, 93(19), 2008.

[55] E. Plum, X. X. Liu, V. A. Fedotov, Y. Chen, D. P. Tsai, and N. I. Zheludev. "Metamaterials: Optical activity without chirality". *Physical Review Letters*, 102(11), 2009.

[56] A. Papakostas, A. Potts, D. M. Bagnall, S. L. Prosvirnin, H. J. Coles, and N. I. Zheludev. "Optical Manifestations of Planar Chirality". *Physical Review Letters*, 90(10), 2003.

[57] X. Ni, N. K. Emani, A. V. Kildishev, A. Boltasseva, and V. M. Shalaev. "Broadband Light Bending with Plasmonic Nanoantennas". *Science (New York, N.Y.)*, 335(6067), 2012.

[58] S. Sun, K.Y. Yang, C.M. Wang, T.K. Juan, W.T. Chen, C. Y. Liao, Q. He, S. Xiao, W.T. Kung, G. Guo, L. Zhou, and D.P. Tsai. "High-Efficiency Broad-

band Anomalous Reflection by Gradient Meta- Surfaces". *Nano letters*, 12(11), 2012.

[59] B. Walther, C. Helgert, C. Rockstuhl, F. Setzpfandt, F. Eilenberger, E. Kley, F. Lederer, A. Tünnermann, and T. Pertsch. "Spatial and Spectral Light Shaping with Metamaterials". *Advanced Materials*, 24(47), 2012.

[60] T. Roy, A. E. Nikolaenko, and E. T. F. Rogers. "A meta-diffraction-grating for visible light". *Journal of Optics*, 15(8), 2013.

[61] X. Ni, S. Ishii, A. V. Kildishev, and V.M. Shalaev. "Ultra-thin, planar, Babinet-inverted plasmonic metalenses". *Light: Science & Applications*, 2(4), 2013.

[62] D. Lin, P. Fan, E. Hasman, and M. L. Brongersma. "Dielectric gradient metasurface optical elements". *Science*, 345(6194), 2014.

[63] W.T. Chen, K. Yang, C. Wang, Y. Huang, G. Sun, C. Y. Liao, W. Hsu, H.T. Lin, S. Sun, L. Zhou, A.Q. Liu, and D.P. Tsai. "High-Efficiency Broadband Meta-Hologram with Polarization- Controlled Dual Images". *Nano Letters*, 14(12), 2014.

[64] D. Veksler, E. Maguid, N. Shitrit, D. Ozeri, V. Kleiner, and E. Hasman. "Multiple Wavefront Shaping by Metasurface Based on Mixed Random Antenna Groups". *ACS Photonics*, 2(5), 2015.

[65] N. Yu and F. Capasso. "Flat optics with designer metasurfaces.". *Nature Materials*, 13(2), 2014.

[66] J. Zhang, K. F. MacDonald, and N. I. Zheludev. "Controlling light-with-light without nonlinearity". *Light: Science & Applications*, 1(e18), 2012.

[67] M. Lapine, I. V. Shadrivov, D.A. Powell, and Y.S. Kivshar. "Magnetoelastic metamaterials". *Nature Materials*, 11(1), 2012.

[68] D. Chicherin. "MEMS-Based High Impedance Surfaces for Milimeter and Submilimeter Wave applications". *Microwave Optical Technology Letters*, 48(12), 2006.

[69] W.M. Zhu, A.Q. Liu, X.M. Zhang, D.P. Tsai, T. Bourouina, J.H. Teng, X.H. Zhang, H.C. Guo, H. Tanoto, T. Mei, G. Q. Lo, and D.L. Kwong. "Switchable magnetic metamaterials using micromachining processes". *Advanced Materials*, 23(15), 2011.

[70] J. Y. Ou, E. Plum, L. Jiang, and N. I. Zheludev. "Reconfigurable photonic metamaterials". *Nano Letters*, 11(5), 2011.

[71] J.Y. Ou, E. Plum, J. Zhang, and N.I. Zheludev. "An electromechanically reconfigurable plasmonic metamaterial operating in the near-infrared.". *Nature nanotechnology*, 8(4), 2013.

[72] J.Y. Ou, E. Plum, J. Zhang, and N. I. Zheludev. "Giant Nonlinearity of an Optically Reconfigurable Plasmonic Metamaterial". *Advanced Materials*, 28(4), 2015.

[73] Nikolay I. Zheludev and Eric Plum. "Reconfigurable nanomechanical photonic metamaterials". *Nature Nanotechnology*, 11(1):16–22, 2016.

[74] J. Russell and R. Cohn. *Pockels Effect*. Book on Demand, 2012.

[75] Jenkins and White. *Fundamentals of Optics*. Mc Graw-Hill Book Company, 1957.

[76] S. Visnovsky. "Magneto-optical Effects in Crystals at normal incidence". *Czech Journal of Physics B*, 37, 1987.

[77] A. Cotton and H. Mouton. "Nouvelle propiete optique (birefringence magnetique) de certains liquides organitques non colloidaux". *C. R. Acad. Sci.*, 145, 1907.

[78] W. Voigt. *Magneto-Und Elektrooptik*. Druck Und Verlag Von B. G. Teubner, 1908.

[79] I.S. Zheludev and O. G. Vlokh. "Electro- and magnetogyration". *Proc. Indian Acad.Sci.*, 92(10), 1983.

[80] O.G. Vlokh and R.O. Vlokh. "The Electrogyration Effect". *Opt. Photon. News*, 20, 2009.

[81] V. A. Markelov. "Experimental Observation of a New Nonreciprocal Magneto-optical Effect". *JETP Lett.*, 25(9), 1977.

[82] E.B. Graham and R.E. Raab. "A molecular theory of linear birefringence induced by crossed electric and magnetic fields". *Molecular Physics.*, 52, 1984.

[83] J. H. Jung, M. Matsubara, T. Arima, J. P. He, Y. Kaneko, and Y. Tokura. "Optical magnetoelectric effect in the polar GaFeO3 ferrimagnet". *Physical Review Letters*, 93(3), 2004.

[84] M. Saito, K. Taniguchi, and T. Arima. "Gigantic Optical Magnetoelectric Effect in CuB 2 O 4". *Journal of the Physical Society of Japan*, 77(1), 2008.

[85] R. Lakes. "Foam Structures with a Negative Poisson's Ratio.". *Science (New York, N.Y.)*, 235(4792), 1987.

[86] K.E. Evans. "Auxetic polymers: a new range of materials". *Endeavour*, 15(4), 1991.

[87] I. G. Masters and K. E. Evans. "Models for the elastic deformation of honeycombs". *Composite Structures*, 35(4), 1996.

[88] G. N. Greaves, a. L. Greer, R. S. Lakes, and T. Rouxel. "Poisson's ratio and modern materials". *Nature Materials*, 10(12), 2011.

[89] Y. Liu and H. Hu. "A review on auxetic structures and polymeric materials". *Sci. Res. Essays*, 5(10), 2010.

[90] M. Carrara, M. R. Cacan, J. Toussaint, M. J. Leamy, M. Ruzzene, and A. Erturk. "Metamaterial-inspired structures and concepts for elastoacoustic wave energy harvesting". *Smart Materials and Structures*, 22(6), 2013.

[91] A. Alderson and K. L. Alderson. "Auxetic materials". *Proceedings of the Institution of Mechanical Engineers, Part G: Journal of Aerospace Engineering*, 221(4), 2007.

[92] https://en.wikipedia.org/wiki/Poisson%27s_ratio.

[93] https://en.wikipedia.org/wiki/Deformation_(mechanics).

[94] J. C. Álvarez Elipe and A. Díaz Lantada. "Comparative study of auxetic geometries by means of computer-aided design and engineering". *Smart Materials and Structures*, 21(10), 2012.

[95] F. Scarpa, P. Panayiotou, and G. Tomlinson. "Numerical and experimental uniaxial loading on in-plane auxetic honeycombs". *The Journal of Strain Analysis for Engineering Design*, 35(5), 2000.

[96] U.D. Larsen, O. Sigmund, and S. Bouwstra. "Design and Fabrication of Compliant Mecromechanisms and Structures with Negative Poisson's Ratio". *, Proceedings of the Ninth Annual International Workshop on Micro Electro Mechanical Systems, IEEE*, 6(2), 1996.

[97] B Xu, F. Arias, S. Brittain, X. Zhao, B. Grzybowski, S. Torquato, and G.M. Whitesides. "Making negative Poisson's ratio microstructures by soft lithography". *Advanced Materials*, 11(14), 1999.

[98] S. Pagliara, K. Franze, C.R. McClain, G.W. Wylde, C. L. Fisher, R.J. M. Franklin, A. J. Kabla, U. F. Keyser, and K. J. Chalut. "Auxetic nuclei in embryonic stem cells exiting pluripotency.". *Nature Materials*, 13(6), 2014.

[99] R.F. Almgren. "An isotropic three-dimensional structure with Poisson's ratio=-1". *Journal of Elasticity*, 15, 1985.

[100] F.C. Smith, F. Scarpa, and B. Chambers. "The electromagnetic properties of re-entrant dielectric honeycombs". *IEEE Microwave and Guided Wave Letters*, 10(11), 2000.

[101] D. Shin, Y. Urzhumov, D. Lim, K. Kim, and D.R. Smith. "A versatile smart transformation optics device with auxetic elasto-electromagnetic metamaterials.". *Scientific reports*, 4, 2014.

[102] F.C. Smith. "Effective permittivity of dielectric honeycombs". *IEE Proc. Microw. Antennas Propag.*, 146(1), 1999.

[103] F. Scarpa, F. C. Smith, B. Chambers, and G. Burriesci. "Mechanical and electromagnetic behaviour of auxetic honeycomb structures". *Aeronautical Journal*, 107(1069), 2003.

[104] C. Lira, F. Scarpa, M. Olszewska, and M. Celuch. "The SILICOMB cellular structure: Mechanical and dielectric properties". *Physica Status Solidi (B) Basic Research*, 246(9), 2009.

[105] P. Kopyt, R. Damian, M. Celuch, and R. Ciobanu. "Dielectric properties of chiral honeycombs - Modelling and experiment". *Composites Science and Technology*, 70(7), 2010.

[106] R. Ciobanu, R. Damian, and I. Casian-Botez. "Electromagnetic characterization of chiral auxetic metamaterials for EMC applications". *Computer Standards and Interfaces*, 32(3), 2010.

[107] D. Shin, Y. Urzhumov, Y. Jung, G. Kang, S. Baek, M. Choi, H. Park, K. Kim, and D. R Smith. "Broadband electromagnetic cloaking with smart metamaterials.". *Nature communications*, 3, 2012.

[108] E. F. Kuester and C. L. Holloway. "Comparison of Approximations for Effective Parameters of Artificial Dielectrics". *IEEE Transactions on Microwave Theory and Techniques*, 38(11), 1990.

[109] J. Valente, J.Y. Ou, E. Plum, I. J. Youngs, and N. I. Zheludev. "Reconfiguring photonic metamaterials with currents and magnetic fields". *Applied Physics Letters*, 106(11), 2015.

[110] J. N. Grima, R. Caruana-Gauci, M. R. Dudek, K.W. Wojciechowski, and R. Gatt. "Smart metamaterials with tunable auxetic and other properties". *Smart Materials and Structures*, 22(8), 2013.

[111] T. Roger, S. Vezzoli, E. Bolduc, J. Valente, J.J. F. Heitz, J. Jeffers, C. Soci, J. Leach, C. Couteau, N.I. Zheludev, and D. Faccio. "Coherent perfect absorption in deeply subwavelength films in the single-photon regime". *Nature Communications*, 6:7031(5), 2015.

[112] S. A. Mousavi, E. Plum, J. Shi, and N. I. Zheludev. "Coherent control of birefringence and optical activity". *Applied Physics Letters*, 105(1), 2014.

[113] U. Efron. *Spatial light modulator technology: materials, devices, and applications*. CRC Press, 1994.

[114] Grigory Lazarev, Andreas Hermerschmidt, Sven Krüger, and Stefan Osten. "LCOS spatial light modulators: Trends and Applications". *Optical Imaging and Metrology: Advanced Technologies*, pages 1–29, 2012.

[115] Hyeonseung Yu, Jongchan Park, KyeoReh Lee, Jonghee Yoon, KyungDuk Kim, Shinwha Lee, and YongKeun Park. "Recent advances in wavefront shaping techniques for biomedical applications". *Current Applied Physics*, 15(5):632–641, 2015.

[116] P. Gunter. "Coherent Light Amplification and Optical Phase Conjugation with Photorefractive Materials". *Phys. Rep.*, 93(4):199, 1982.

[117] X. Xu, H. Liu, and Lihong V. W. "Time-reversed ultrasonically encoded optical focusing into scattering media". *Nat Photon*, 5(3), 2011.

[118] Xu Fang, Kevin F MacDonald, and Nikolay I Zheludev. "Controlling light with light using coherent metadevices: all-optical transistor, summator and invertor". *Light: Science & Applications*, 4(February):e292, 2015.

[119] Al. Boltasseva and V.M. Shalaev. "Fabrication of optical negative-index metamaterials: Recent advances and outlook". *Metamaterials*, 2(1), 2008.

[120] C. M. Soukoulis and M. Wegener. "Past achievements and future challenges in the development of three-dimensional photonic metamaterials". *Nature Photonics*, 5(9), 2011.

[121] https://en.wikipedia.org/wiki/Skin_effect.

[122] H. Van Wolferen and L.Abelmann. *Lithography: Principles, processes and materials.* Nova Science Publishers Inc., 2011.

[123] N. Dutta, I.O. Mirza, S. Shi, and D.W. Prather. "Fabrication of Large Area Fishnet Optical Metamaterial Structures Operational at Near-IR Wavelengths". *Materials*, 3(12), 2010.

[124] N. I. Zheludev, E. Plum, and V. A. Fedotov. "Metamaterial polarization spectral filter: Isolated transmission line at any prescribed wavelength". *Applied Physics Letters*, 99(17), 2011.

[125] I. Bergmair, B. Dastmalchi, M. Bergmair, A. Saeed, W. Hilber, G Hesser, C. Helgert, E. Pshenay-Severin, T. Pertsch, E. B. Kley, U. Hübner, N. H. Shen, R. Penciu, M. Kafesaki, C. M. Soukoulis, K. Hingerl, M. Muehlberger, and R. Schoeftner. "Single and multilayer metamaterials fabricated by nanoimprint lithography.". *Nanotechnology*, 22, 2011.

[126] J. Orloff. *Handbook of charged particle optics*. CRC Press, 2008.

[127] C. A. Volkert and A. M. Minor. "Focused Ion Beam Microscopy and Micromachining". *MRS Bulletin*, 32(05), 2007.

[128] S. Reyntjens and R. Puers. "A review of focused ion beam applications in microsystem technology". *Journal of Micromechanics and Microengineering*, 11(4), 2001.

[129] T. E. Everhart and R. F M Thornley. "Wide-band detector for micro-microampere low-energy electron currents". *Advances in Imaging and Electron Physics*, 133, 1960.

[130] C. N. Burrous, A. J. Lieber, and V. T. Zaviantseff. "Detection Efficiency of a Continuous Channel Electron Multiplier for Positive Ions". *Review of Scientific Instruments*, 38(10), 1967.

[131] P. Sigmund. "Theory of Sputtering - Sputtering Yield of Amorphous and Polycrystalline Targets". *Physical Review*, 184(2), 1969.

[132] P. Sigmund. "A mechanism of surface micro-roughening by ion bombardment". *Journal of Materials Science*, 8(11), 1973.

[133] M. Rosler and W. Brauer. "Theory of Electron Emission from Solids by Proton and Electron Bombardment". *Physica Status Solidi B*, 148(1), 1988.

[134] D. Hasselkamp. *Kinetic electron emission from solid surfaces under ion bombardment*, volume 123 of *Springer Tracts in Modern Physics*. Springer Berlin Heidelberg, 1992.

[135] A. Yasaka. *Feasibility Study of Spatial-Phase-Locked Focused-Ion-Beam Lithography*. Massachusetts Institute of Technology, 1995.

[136] V. A. Fedotov, M. Rose, S. L. Prosvirnin, N. Papasimakis, and N. I. Zheludev. "Sharp trapped-mode resonances in planar metamaterials with a broken structural symmetry". *Physical Review Letters*, 99(14):14740 (4), 2007.

[137] http://www.azom.com/properties.aspx?ArticleID=53.

[138] http://www.azom.com/article.aspx?ArticleID=5147.

[139] https://en.wikipedia.org/wiki/Euler-Bernoulli_beam_theory.

[140] https://en.wikipedia.org/wiki/Second_moment_of_area.

[141] https://en.wikipedia.org/wiki/Young%27s_modulus.

[142] https://en.wikipedia.org/wiki/Joule_heating.

[143] https://en.wikipedia.org/wiki/Heat_flux.

[144] http://en.wikipedia.org/wiki/Gold.

[145] https://en.wikipedia.org/wiki/Thermal_expansion.

[146] http://global.kyocera.com/prdct/fc/list/tokusei/bouchou/index.html.

[147] http://www.engineeringtoolbox.com/linear-expansion-coefficients-d_95.html.

[148] S. Prasanna and S.M. Spearing. "Materials Selection and Design of Microelectrothermal Bimaterial Actuators". *Journal of Microelectromechanical Systems*, 16(2), 2007.

[149] https://en.wikipedia.org/wiki/Lorentz_force.

[150] G. Chen and P. Hui. "Thermal conductivities of evaporated gold films on silicon and glass". *Applied Physics Letters*, 74(20), 1999.

[151] D. R. Queen and F. Hellman. "Thin film nanocalorimeter for heat capacity measurements of 30 nm films". *Review of Scientific Instruments*, 80(6), 2009.

[152] D. K. Wickenden, J. L. Champion, R. Osiander, R. B. Givens, J. L. Lamb, J. A. Miragliotta, D. A. Oursler, and T. J. Kistenmacher. "Micromachined polysilicon resonating xylophone bar magnetometer". *Acta Astronautica*, 52, 2003.

[153] F. Keplinger, S. Kvasnica, A. Jachimowicz, F. Kohl, J. Steurer, and H. Hauser. "Lorentz force based magnetic field sensor with optical readout". *Sensors and Actuators, A: Physical*, 110, 2004.

[154] J. Zhang, K. F MacDonald, and N. I Zheludev. "Nonlinear dielectric optomechanical metamaterials". *Light: Science & Applications*, 2(8), 2013.

[155] K. Seshan. *Handbook of thin-film deposition processes and techniques.* Noyes Publications; William Andrew Publishing, Santa Clara, California, second edition, 2002.

[156] K.M. McPeak, S.V. Jayanti, S. J. P. Kress, S. Meyer, S. Iotti, A. Rossinelli, and D. J. Norris. "Plasmonic Films Can Easily Be Better: Rules and Recipes". *ACS Photonics*, 2(3), 2015.

[157] http://www.nanotechnik.com/mm3a-em.html.

[158] Joseph N Grima, Pierre-sandre Farrugia, Ruben Gatt, and Daphne Attard. "On the auxetic properties of rotating rhombi and parallelograms". *Physica Status Solidi B*, 529(3):521–529, 2008.

[159] Doris Schattschneider. *The Plane Symmetry Groups : Their Recognition and Notation*, volume 85. American Mathematical Monthly, 1978.

[160] Y. Prawoto. "Seeing auxetic materials from the mechanics point of view: A structural review on the negative Poisson's ratio". *Computational Materials Science*, 58, 2012.

[161] M.I. Stockman, S.V. Faleev, and D.J. Bergman. "Coherent control of femtosecond energy localization in nanosystems.". *Physical review letters*, 88(6), 2002.

[162] B. Gjonaj, J. Aulbach, P.M. Johnson, A.P. Mosk, L. Kuipers, and A. Lagendijk. "Active spatial control of plasmonic fields". *Nature Photonics*, 5(6), 2011.

[163] W. Wan, Y. Chong, L. Ge, H. Noh, A. D. Stone, and H. Cao. "Time-reversed lasing and interferometric control of absorption.". *Science (New York, N.Y.)*, 331(6019), 2011.

[164] Z. Li, S. Zhang, N. J. Halas, P. Nordlander, and H. Xu. "Coherent modulation of propagating plasmons in silver-nanowire-based structures". *Small*, 7(5), 2011.

[165] J. W. Yoon, G. M. Koh, S. H. Song, and R. Magnusson. "Measurement and modeling of a complete optical absorption and scattering by coherent surface plasmon-polariton excitation using a silver thin-film grating". *Physical Review Letters*, 109(25), 2012.

[166] E. Altewischer. "Plasmon-assisted transmission of entangled photons". *Nature*, 418(July), 2002.

[167] D. E. Chang, A. S. Sørensen, P. R. Hemmer, and M. D. Lukin. "Quantum optics with surface plasmons". *Physical Review Letters*, 97(5), 2006.

[168] D. E. Chang, A. S. Sørensen, E. A. Demler, and M.D. Lukin. "A single-photon transistor using nanoscale surface plasmons". *Nature Physics*, 3(11), 2007.

[169] A. V. Akimov, A. Mukherjee, C. L. Yu, D. E. Chang, A. S. Zibrov, P. R. Hemmer, H. Park, and M.D. Lukin. "Generation of single optical plasmons in metallic nanowires coupled to quantum dots.". *Nature*, 450(7168), 2007.

[170] R.W. Heeres, L.P. Kouwenhoven, and V. Zwiller. "Quantum interference in plasmonic circuits.". *Nature nanotechnology*, 8(10), 2013.

[171] M. S. Tame, K.R. McEnery, S. K. Ozdemir, J. Lee, S. A. Maier, and M. S. Kim. "Quantum plasmonics". *Nat Phys*, 9(6), 2013.

[172] J. S. Fakonas, H. Lee, Y.A. Kelaita, and H. A. Atwater. "Two-plasmon quantum interference". *Nature Photonics*, 8(4), 2014.

[173] T.J. Davis, D.E. Gómez, and F. Eftekhari. "All-optical modulation and switching by a metamaterial of plasmonic circuits.". *Optics letters*, 39(16), 2014.

[174] S. A. Mousavi, E. Plum, J. Shi, and N. I. Zheludev. "Coherent control of optical polarization effects in metamaterials". *Scientific Reports*, 5:8977, 2015.